University of
Stavanger

Faculty of Science and Technology

MASTER'S THESIS

Study program/ Specialization: Marine and Offshore Technology	Spring semester, 2019 Open / ~~Restricted access~~
Writer: Julie-Ann Knight	Julie-Ann Knight (Writer's signature)

Faculty supervisor:

Dr. Charlotte Obhrai

Thesis title:

The Influence of an Unstable Turbulent Wind Spectrum on the Loads and Motions on a Floating Offshore Wind Turbine

Credits (ECTS): 30

Key words: Wind Energy Atmospheric Stability Højstrup 1981 Unstable Spectra Model Floating Offshore Wind Turbines OC3-Hywind, OC4-DeepCwind Wind Coherence	Pages: 93 + enclosure/Appendix: 18 Stavanger, 14th June 2019

Abstract

Floating offshore wind turbines are exposed to harsh environmental conditions throughout their lifetime and typically experience unstable atmospheric conditions. Including the effect of atmospheric stability should improve the accuracy of fatigue load calculations, and subsequently, the design of the wind turbine. The objective of this study is to investigate the influence of different unstable turbulent wind fields on the loads and motions on a floating offshore wind turbine (FOWT), with emphasis on Højstrup's 1981 Unstable Spectra Model. The turbulent wind fields were generated using the spectral representation approach by Shinozuka and Deodatis [1992], and then used within SIMA to simulate the fatigue and motions on a FOWT. The resulting fatigue loads and platform motions were analyzed under varying stability and varying coherence for both the OC3-Hywind spar-buoy FOWT and the OC4-DeepCwind semisubmersible FOWT. The most significant difference between the simulated wind fields was found for the tower top torsion fatigue load, where very unstable conditions were 47% larger than neutral conditions for the OC3-Hywind FOWT and 30.4% larger for the OC4-DeepCwind FOWT. Since very unstable conditions corresponded to the highest turbulence intensities and largest turbulent fluctuations, they consequently resulted in larger fatigue loads for the tower top torsion. Other modes, such as the blade root flap-wise and tower base fore-aft bending moments, were relatively unaffected.

Unlike the notable differences seen when simulating unstable conditions, the sensitivity study for variations in lateral and vertical coherence showed less variability and little consequence on a majority of the platform modes. However, a variation in vertical coherence resulted in fatigue loads for the blade root-flap wise moment that were 16.25% (OC3) and 38.8% (OC4) larger under a more coherent wind field, while a variation in lateral coherence gave fatigue loads for tower top torsion that were 13.4% (OC3) and 20.7% (OC4) larger under a less coherent wind field. Overall, one can conclude that the additional low frequency turbulent behavior, associated with unstable conditions, increased the turbulent fluctuations and therefore, was of more importance than changes in wind coherence for this study.

In addition to assessing the influence of stability and coherence on a FOWT, the results were compared to the findings of Putri [2016]. The goal of the comparison was to see if more realistic turbulence intensities, and hence damage equivalent loads, could be simulated under unstable atmospheric conditions using Højstrup's 1981 Unstable Spectra Model. In contrast to the Højstrup model, the fitted Mann model, used within that study, does not account for buoyancy generated turbulence. This difference could explain why Putri [2016] found higher turbulence values and therefore, larger fatigue loads under neutral atmospheric stability conditions. Nonetheless, further analysis should be conducted to improve the Højstrup model in order to better depict unstable conditions in an offshore environment.

Acknowledgements

I would like to express my sincere gratitude to my supervisor, Dr. Charlotte Obhrai, for the continuous support, feedback, and invaluable guidance throughout the course of this thesis. The numerous meetings and her passion for this topic kept me motivated for the entirety of the semester. I am extremely grateful to have been given the opportunity to work on this master thesis topic and to explore the benefits and challenges of offshore wind energy.

I am also very thankful for my co-supervisors, Dr. Etienne Cheynet and Rieska Putri, who provided me with key insights and expertise. I truly appreciate them spending time to collaborate with me, their incredible patience, and their abundant knowledge that was needed in order to carry out this study.

Finally, I would like to extend my greatest appreciation for my family, who have always encouraged and supported me in achieving my goals. My experience in Norway would not have been possible without their love, guidance, and endless faith.

Stavanger, 14th June 2019

Julie-Ann Knight

Table of Contents

List of Figures

List of Tables

Nomenclature

Latin Symbols

A : rotor swept area

b : Wöhler exponent

c_2^w: second decay coefficient

c_p : specific heat of the air at constant pressure

C : constant used for fatigue damage $C = N\sigma^b$

C_p : power coefficient

C_y^i, C_z^i : decay coefficient in the y and z direction, respectively & $i = \{u, v, w\}$

Co : real part of the cross spectrum of coherence

d_y, d_z : horizontal and vertical separation distance, respectively

D : total fatigue damage

f : non-dimensionalized frequency $f = \frac{nz}{u}$

f_i : non-dimensionalized frequency, related to inversion height $f_i = \frac{nz_i}{u}$

g : gravity acceleration constant

I_u, I_v, I_w : Turbulence Intensity (longitudinal, lateral, and vertical, respectively)

k : constant of proportionality

K_h : turbulent exchange coefficient for heat

K_m : turbulent exchange coefficient for momentum

L : Monin-Obuhkov length

L_m : length scale for the eddy size of the peak of the turbulence spectrum

n : frequency [Hz]

n_i : respective load cycles/number of load range occurrences

N_{eq} : equivalent number of load cycles

N_i : total number of cycles until failure

q : heat flux

Q : imaginary part of the cross spectrum of coherence

R_b : bulk Richardson number

R_i : gradient Richardson number

R_f : flux Richardson number

S_i : turbulent velocity spectrum, $i = \{u, v, w\}$ & u = along wind, v = cross wind, and w = vertical wind

T_o : mean temperature of the surface layer

$\bar{u}$: mean wind speed [m/s]

u', v', w' : velocity fluctuation in the along wind, cross wind and vertical wind, respectively

u_* : surface scaling velocity/friction velocity $u_{*0}(1-\frac{z}{z_i})$ [m/s]

U : wind speed

z : height above ground

z_i : height of lowest inversion/boundary layer depth

z_0 : surface roughness

Greek Symbols

α_c : Charnock's parameter

$\alpha\varepsilon^{2/3}$: measure of energy dissipation rate

γ : wind coherence

Γ : degree of anisotropy

$\bar{\theta}$: mean potential temperature

κ : von Kármán constant

ν_* : characteristic velocity scale $(=\sqrt{\tau/\rho}\,)$

ρ : density of air

σ : standard deviation

σ_i : real load ranges

σ_{eq} : alternating equivalent stress/damage equivalent load

τ : turbulent friction stress

ϕ_ε : dimensionless dissipation rate

ψ_m : stability-dependent function

Abbreviations

a.m.s.l: Above Mean Sea Level

AFCRL: Air Force Cambridge Research Laboratories

DEL: Damage Equivalent Load

FINO: Forschungsplattformen in Nord-und Ostsee

FOWT: Floating Offshore Wind Turbine

GWEC: Global Wind Energy Council

HAWC2: Horizontal Axis Wind turbine simulation Code 2nd generation

HAWT: Horizontal Axis Wind Turbine

IEA: International Energy Agency

IEC: International Electrotechnical Commission

JONSWAP: Joint North Sea Wave Project

LIDAR: Light Detection and Ranging

MABL: Marine Atmospheric Boundary Layer

MW: MegaWatt

NREL: National Renewable Energy Laboratory

OC3: Offshore Code Comparison Collaboration

OC4: Offshore Code Comparison Collaboration Continuation

RAO: Response Amplitude Operator

RIFLEX: Riser System Analysis Program

SIMA: Simulation Workbench for Marine Architecture

SIMO: Simulation of Marine Operations

SWL: Still Water Level

TI: Turbulence Intensity

TLP: Tension Leg Platform

VAWT: Vertical Axis Wind Turbine

1. Introduction

1.1 Background/Motivation

With the growing interest and need for renewable energy throughout the world, the study and research of wind fields has become an important aspect in the design and operation of offshore wind turbines. There are a number of reasons to bring the benefits of wind turbines offshore, including reduced friction/lower surface roughness, which allows for higher average wind speeds, homogeneous conditions, so, theoretically, reduced turbulence, and more space to employ different projects. However, there are also numerous difficulties, such as structural loads, placement in a corrosive environment, environmental limitations, limited access and higher costs for maintenance, and high costs for cables and grid connections, depending on the distance from shore, and foundations, depending on the water depth [Obhrai, 2018]. Keeping these issues in mind, it is beneficial to look at wind turbulence, the profile of the wind, the direction of the wind, etc., all of which can significantly contribute to the motions of a floating offshore wind turbine (FOWT) and subsequently, the lifetime integrity of the structure.

In order to assist in developing better designs and maintenance strategies, it is important to investigate the effect atmospheric stability and turbulent wind modelling has on both the power production of wind turbines and the fatigue loads. These concepts have been researched by a variety of project teams including Sathe et al. [2013] who suggested that the fatigue loads on the tower and rotor were influenced by atmospheric stability conditions. In another study by Kretshmer et al. [2018], atmospheric stability and its relationship to the fatigue loads on an offshore wind turbine were investigated using collected measurements from the German research wind plant, alpha ventus. The study specifically looked at the impact of atmospheric stability on the blade root bending and the tower base moments, which were found to be the highest under unstable conditions in wind speeds between cut-in speed and approximately 14 m/s. Similar to what was discovered in the research of Sathe et al. [2013], Kretshmer et al. [2018] noticed that fatigue loads on the tower base were primarily influenced by atmospheric turbulence, unlike the fatigue loads on the blade root bending, which were influenced by a combination of wind shear for stable wind conditions and turbulence for neutral and unstable wind conditions. For their analysis, the fatigue loads were determined using the concept of damage equivalent load (DEL), as was done in this study.

The research of wind fields and turbulence models has been continuing to grow and is important when considering wind turbine design and maintenance. With all this in mind, the current study focuses on how turbulent wind fields and generated wind coherence influence the motions and loads on a FOWT, with special attention paid to Højstrup's 1981 Unstable Spectra Model.

In the research of turbulent wind spectra thus far, descriptions of wind fields in varying atmospheric stability have been centrally focused around neutral wind conditions. For example, a variety of studies rely on the recommendations of the IEC standards, which details two turbulence models: the IEC Kaimal Spectra & Exponential Coherence Model and the Mann Spectral Tensor Model [IEC, 2005], neither of which consider the effect of atmospheric stability. The IEC Kaimal model was not designed to take into account atmospheric stability, and the Mann model was originally developed for neutral atmospheric stability, although this model can be fitted to wind measurements to include the influence of different atmospheric conditions [Sathe et al., 2013]. Using the models from the IEC standards would typically give a conservative estimation of loads [Sathe et al., 2013]. With that being said, the IEC spectral models were defined as a way to assist in the design phase of the wind turbine. Considering that design wind speeds are typically very large, which corresponds to neutral conditions [Cheynet et al., 2018], the inclusion of non-neutral conditions in the IEC standards was not a priority.

Since many research studies are based on the IEC recommendations, it seems appropriate to conduct a study involving a spectral model that considers unstable atmospheric conditions, since these conditions are most prevalent offshore [Sathe et al, 2013]. To the author's knowledge, the Højstrup 1981 Unstable Spectra Model has not been used to investigate the fatigue loads and motions of a FOWT. By emphasizing unstable conditions, the Højstrup model takes into account the low frequency behavior of the velocity spectra, which is of particular interest to floating offshore structures, such as wind turbines.

In wind engineering, it is also important to define an appropriate coherence model. The Davenport Coherence Model, which is commonly used in creating wind fields, uses a simplified expression for the co-coherence of longitudinal turbulence components related to the separation between points. According to the model, as the separation approaches zero, the coherence approaches 1. However, two points located in space are never completely coherent, which shows a limitation of the Davenport model. The scope of this thesis involves combining the Højstrup spectra model with not only the Davenport Coherence Model, but also an improved coherence model, which takes into account atmospheric stability. The goal of incorporating a different coherence model is to improve upon the findings of past research and observe the influence of changing the coherence [Cheynet, 2018].

1.2 Objectives

The primary goals of this master's thesis are as follows:

- Generate turbulent wind fields based on Højstrup's 1981 Unstable Spectra Model
- Investigate how synthetic/generated wind fields from different turbulent wind spectra effect the fatigue and motions of a spar-buoy type and semi-submersible type floating offshore wind turbine
- Compare the findings to previous studies to determine if more realistic turbulence intensities, and consequently, more realistic damage equivalent loads can be simulated under unstable atmospheric conditions
- Conduct a sensitivity study on the effect of vertical and lateral coherence on the loads and motions of a floating offshore wind turbine
- Compare the eigen/natural frequencies of a particular floating offshore wind turbine with the response frequencies

1.3 Thesis Methodology & Organization

To achieve the goals of this thesis, it was first necessary to carry out a literature review and become familiar with Højstrup's 1981 Unstable Spectra Model. After acquiring a good background and understanding of the model parameters, simulations were set up in MATLAB to generate a turbulent wind input that could represent unstable atmospheric conditions and then run for each desired scenario. The turbulent wind input was then used to simulate the fatigue and motions of a FOWT using the Simulation Workbench for Marine Application (SIMA), developed by SINTEF Ocean, and specifically the coupled SIMO-RIFLEX program within SIMA. These results were then processed and analyzed to determine the damage equivalent loads and resultant platform motions.

The organization of this thesis is as follows:

Chapter 1: Introduction – gives an overview of the background information, objectives, limitations of previous studies, and the organization of this thesis report.

Chapter 2: Theory – details the relevant theories of offshore wind power, atmospheric stability, wind speed profile, turbulence and turbulent wind models, and wind coherence.

Chapter 3: Methodology – contains pertinent information on the specifications of the OC3-Hywind spar-buoy and OC4-DeepCwind semisubmersible floating offshore wind turbines, how the wind fields were modelled, how the simulations were performed and set-up, and details about the software needed to complete the objectives of this thesis.

Chapter 4: Results & Discussion – presents the simulation results as damage equivalent loads and platform motion responses of the specified FOWTs using the Højstrup 1981 Unstable Spectra Model under varying stability and varying coherence, and an analysis of the results.

Chapter 5: Conclusion – delivers a summary of the significant results and overall conclusions that can be made from the analysis of this study, along with recommendations for future work.

2. Theory

2.1 Offshore Wind Power

In recent years, offshore wind energy has taken on a more significant role in the global energy sector. According to the Global Wind Energy Council's (GWEC) Global Energy Report 2017, there are 18,814 MW of offshore wind installed across the globe, with a record breaking 4,334 MW of new offshore wind power installed in 2017 [GWEC, 2018]. *Figure 2.1* shows the distribution of the global offshore wind capacity in the various markets, cumulatively and in 2017 alone. A majority of this offshore wind is related to fixed foundations, but the report goes on to predict that floating offshore wind will become cost-competitive by the end of the 2020s, and gain momentum in the 2030s.

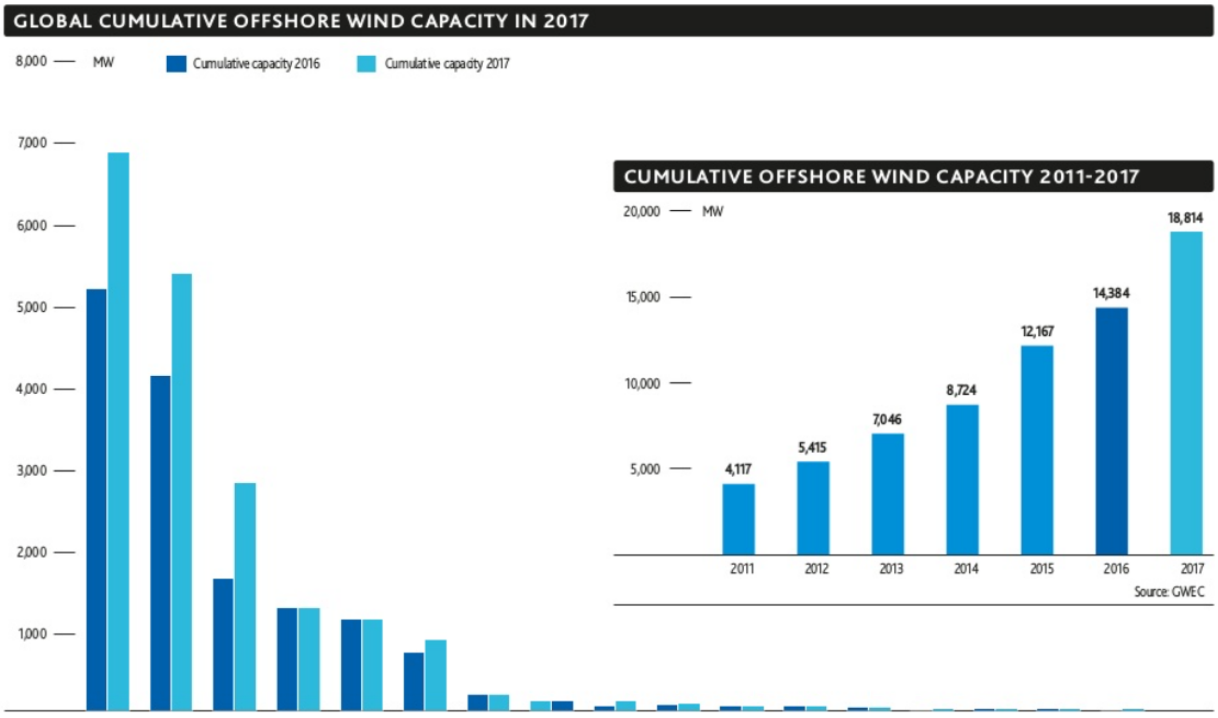

	UK	Germany	PR China	Denmark	Netherlands	Belgium	Sweden	Vietnam	Finland	Japan	South Korea	United States	Ireland	Taiwan	Spain	Norway	France	Total
Total 2016	5,156	4,108	1,627	1,271	1,118	712	202	99	32	60	35	30	25	0	5	2	0	14,483
New 2017	1,680	1,247	1,164	0	0	165	0	0	60	5	3	0	0	8	0	0	2	4,334
Total 2017	6,836	5,355	2,788	1,271	1,118	877	202	99	92	65	38	30	25	8	5	2	2	18,814

Source: GWEC

Figure 2.1: Offshore Wind Capacity according to the Global Wind Energy Council's (GWEC) Global Energy Report 2017

In order to become more competitive with other energy sources, wind turbines are getting larger, since the larger the wind turbine, the more power it can harness. The maximum power available in the wind is given by the following equation [Manwell, et al., 2010]:

$$P = \frac{1}{2}\rho A U^3 \tag{2.1}$$

where ρ is the density in air, A is the rotor swept area, and U is the wind speed. The maximum power that can be extracted from the wind is thus:

$$P = \frac{1}{2}\rho A U^3 * C_p \tag{2.2}$$

where C_p is the power coefficient. The power coefficient represents the ratio of the power output from the wind to the power available in the wind, and is bounded by a theoretical limit of power that can be extracted by a wind turbine. The value for this theoretical limit, known as the Betz limit, is 16/27, approximately 0.59, and was derived by Albert Betz in 1919 [Betz, 1926]. Here, it is important to distinguish the difference between the total power available when the wind blows, the amount of usable power considering the Betz limit, and the total amount of power output from the turbine considering the efficiency of the turbine. The efficiency of the turbine is related to the wind resource at the particular site, which includes factors such as wind shear, wind turbulence, and yaw misalignment [Micallef and Sant, 2016].

Three factors that significantly influence the power extraction of wind turbines include wind speed, cross-sectional rotor swept area, and the conversion efficiency of the rotor, transmission system, and generator. Although these factors have the potential to help generate a higher power output from the wind turbine, increases in wind speed and rotor swept area would also cause an increase in the loads acting on the wind turbine [Gitano-Briggs, 2012].

2.2 Atmospheric Stability

When considering the wind resource at a particular site, it is also beneficial to look at atmospheric stability, which is related to the temperature of the air. Atmospheric stability ranges from stable, neutral, and unstable conditions based on the "tendency for air particles to move vertically" relative to the temperature of their surroundings [*Atmospheric Stability*, accessed 2019]. In stable conditions, the air particles are cooler than the surrounding air, causing them to sink or remain where they are. This stratification leads to less mixing and a higher velocity gradient/more velocity shear, although friction velocity is often lower for stable conditions and typically leads to a low atmospheric boundary layer height. With that being said, in stable conditions, the turbulence is typically referred to as "mechanically generated" or "shear produced" turbulence. In unstable conditions, the air particles are warmer than the surrounding air, which causes them to rise. Hence, this is called "buoyancy generated" turbulence. In an unstable atmosphere, there is more vertical mixing and a lower velocity gradient/less velocity shear. Due to the enhanced vertical mixing, one would expect larger turbulent fluctuations and higher fatigue loads under unstable conditions, which are typically more dominant at offshore sites [Sathe et al., 2013]. However, stability conditions are largely dependent on the site location [Jonkman and Veers, 2019]. Overall, the thermal effects of atmospheric stability reduce turbulence in stable conditions, increase turbulence in unstable conditions, and have a negligible effect on turbulence in neutral conditions.

Atmospheric stability can also be characterized based on the Monin-Obukhov length (L), which is the length scale of energy-containing eddies [Chougule, 2017]. It can also be defined as the level in which buoyancy production starts to exceed shear production of turbulent kinetic energy [McNaughton, 2004]. The Monin-Obukhov length was mathematically derived by [Monin and Obukhov, 1954] as follows:

$$L = -\frac{v_*^3}{\kappa \frac{g}{T_o} \frac{q}{c_p \rho}} \tag{2.3}$$

where v_*^3 is the characteristic velocity scale = $\sqrt{\tau/\rho}$ (τ: turbulent friction stress and ρ: density of air), κ is von Karman constant $\approx$ 0.4 [Högström, 1988], g/T_o is a dimensional constant (g: gravity acceleration constant and T_o: mean temperature of the surface layer), and $q/c_p\rho$ is temperature flux (q: is heat flux and c_p: specific heat of the air at constant pressure). The heat flux helps determine the sign of L; for instance, with stable atmospheric conditions, the heat flux is directed downward ($q < 0$), which makes L positive. Whereas, with unstable atmospheric conditions, heat flux is directed upward ($q > 0$), making L negative. Theoretically, these two conditions meet at neutral atmospheric conditions, when $q = 0$ [Monin and Obukhov, 1994]. It is important to recognize that *Equation 2.3* relies on a few assumptions, including that the turbulent fluxes can be modelled by bulk quantities.

The Monin-Obukhov length is an important part of classifying thermal stratification in the surface layer, and is typically associated with the height above ground (z). The ratio between the height above ground and the Monin-Obuhkov length is recognized as an important stability parameter which reflects the impact of varying height and stability conditions [Kaimal and Finnigan, 1994]. This ratio also expresses the relationship between the mechanical/shear turbulent production and the buoyant turbulent production, and will be referred to as the dimensionless Obukhov stability parameter. Since *Equation 2.3* involves some assumptions, it is better to solve for the Monin-Obukhov length using the dimensionless stability parameter as given in [Kaimal and Finnigan, 1994]:

$$\frac{z}{L} = -\frac{(g/\bar{\theta})(\overline{w'\theta'})_o}{u_*^3/kz}$$

(2.4)

where $(g/\bar{\theta})$ is referred to as the buoyancy parameter, with $\bar{\theta}$ equal to the mean potential temperature, $(\overline{w'\theta'})_o$ is the temperature flux at the surface, u_* is friction velocity, and k is the constant of proportionality. The negative sign is included so that z/L has a negative value for unstable conditions and a positive value for stable conditions.

Atmospheric stability can also be estimated using the bulk Richardson number, as given in *Equation 2.5* [Kaimal and Finnegan, 1994]:

$$R_b = \frac{(g/\bar{\theta})(\bar{\theta}_z - \bar{\theta}_o)/2}{(\bar{u}_z/z)^2}$$

(2.5)

where $\bar{\theta}_z$ and $\bar{\theta}_o$ are the mean potential temperatures at height z and at the surface, respectively, and $\bar{u}_z$ is the mean wind speed at height z. The bulk Richardson number varies relative to the dimensionless Obukhov stability parameter, meaning that for unstable conditions, $R_b < 0$, bulk Richardson number is used as [DNV-RP-C205, 2010]:

$$\frac{z}{L} = 10R_b$$

(2.6)

For stable conditions, $0 \le R_b \le 0.2$, the bulk Richardson number is used as [DNV-RP-C205, 2010]:

$$\frac{z}{L} = \frac{10R_b}{1 - 4.5R_b}$$

(2.7)

There are two other forms of the Richardson number that can be useful indicators of stability: the gradient Richardson number and the flux Richardson number [Kaimal and Finnegan, 1994]. The gradient Richardson number was the most widely used way of defining stability in earlier research of the atmosphere and highlights the “relative importance of buoyancy and shear in producing turbulence” [Kaimal and Finnegan, 1994]. Similarly, the flux Richardson number defines the ratio of the production rate of buoyant turbulence to the production rate of shear turbulence, although it is rarely used in practice. The gradient Richardson number (R_i) and the flux Richardson number (R_f) can be found using *Equation 2.8* and *2.9*, respectively.

$$R_i = \frac{(g/\bar{\theta})(\partial\bar{\theta}/\partial z)}{(\partial\bar{u}/\partial z)^2}$$

(2.8)

$$R_f = \frac{(g/\bar{\theta})(\overline{w'\theta'})}{\overline{u'w'}(\partial\bar{u}/\partial z)} \cong \frac{K_h}{K_m} R_i \tag{2.9}$$

where $\partial\bar{\theta}/\partial z$ is the gradient of the mean potential temperature, $\partial\bar{u}/\partial z$ is the gradient of the mean wind speed, $\overline{u'w'}$ is the mean product of velocity fluctuations, and K_h and K_m are turbulence exchange coefficients for heat and momentum, respectively.

Throughout this thesis, atmospheric stability will be classified using Monin-Obukhov length based on the atmospheric stability classes as suggested by Gryning et al. [2007]. These classes are presented in *Table 2.1*.

Table 2.1 Atmospheric Stability Classes

Atmospheric Stability Class	Monin-Obukhov Length (m)
Very Unstable	$-100 \leq L \leq -50$
Unstable	$-200 \leq L \leq -100$
Near unstable	$-500 \leq L \leq -200$
Neutral	$\lvert L \rvert \geq 500$
Near stable	$200 \leq L \leq 500$
Stable	$50 \leq L \leq 200$
Very Stable	$10 \leq L \leq 50$

2.3 Wind Speed Profile

Referring back to the wind power equation, it can be seen that wind speed is very influential in increasing the power output of a wind turbine, since power is proportional to the cube of the wind speed. It is also important to note that since conditions offshore vary from those onshore, it is of particular interest to accurately depict the wind speed profile in the marine atmospheric boundary layer (MABL). The MABL refers to the part of the atmosphere that is in direct contact with the ocean, and is therefore, directly influenced by exchanges of momentum, energy, and mass between the ocean and the atmosphere [Kaimal and Finnegan, 1994].

The Earth consists of four major layers: the troposphere, stratosphere, mesosphere, and thermosphere. The troposphere is the layer closest to the Earth's surface, and since it accounts for most of the atmosphere, it is especially important when considering wind speeds within the first few hundred meters of the surface. The troposphere consists of the free atmosphere and the boundary layer; the boundary layer can be further broken up into the surface layer and the Ekman/transition layer. The surface layer (~50-100 m) is described by approximately constant shearing stress vertically, which means that the wind profile is influenced by surface friction and vertical temperature gradients [Kaimal and Finnegan, 1994]. Just above the surface layer, the atmosphere is characterized by variable shearing stress, so the wind profile in that region is influenced by the earth's rotation in addition to surface friction and vertical temperature gradients. *Figure 2.2* [shodor.org, accessed 2019] shows a simplified depiction of the troposphere just above the Earth's surface.

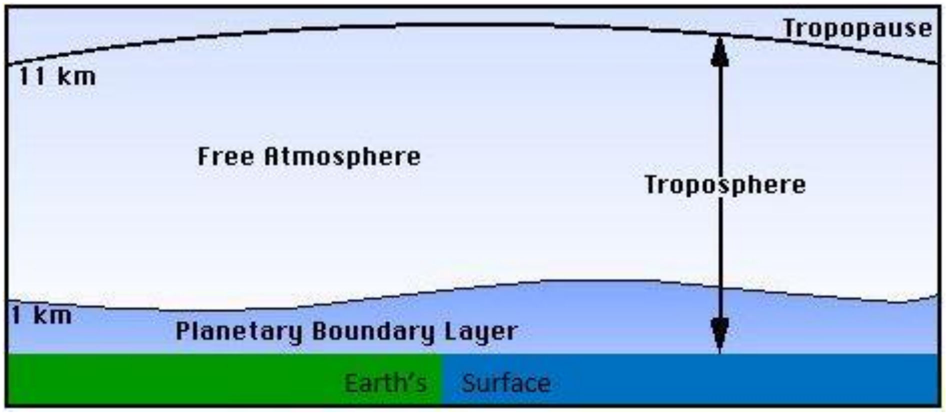

Figure 2.2: Depiction of Planetary Boundary Layer and Free Atmosphere

The behavior of the wind speed profile in the atmospheric surface layer, defined as the lowest 10% of the planetary boundary layer, has been predicted using Monin-Obukhov similarity theory (MOST) [Monin and Obukhov, 1954] and surface-layer scaling. However, deviations from MOST have been noted for atmospheric conditions offshore at altitudes as low as 29 m above mean sea level (a.m.s.l) [Peña et al., 2008], which makes the design of the wind turbine difficult since offshore wind turbines typically extend beyond this altitude. Unfortunately, it is challenging to collect wind speed measurements over the sea, and it is particularly hard to fully capture undisturbed marine conditions. Thankfully, new technologies have been implemented to collect measurements in the MABL, including light detection and ranging (LiDAR) to create vertical profiles of the atmosphere [Peña et al., 2008]. In addition, sonic anemometer data was collected over two years at the German research platform FINO1, located in the North Sea. In a study by Cheynet et al. [2018], this data was analyzed to determine the limits of current spectral models and to analyze turbulence characteristics within the boundary layer. The data collected at the FINO1 platform revealed that very unstable conditions were typically associated with low wind speeds; whereas, neutral conditions were often associated with high wind speeds [Cheynet et al., 2018].

Logarithmic Wind Speed Profile

The logarithmic wind speed profile is considered for this thesis and is given in the Recommended Practice for neutral conditions as seen in *Equation 2.10* [DNV-RP-C205, 2010]:

$$U(z) = \frac{u_*}{\kappa} \ln(z/z_o) \tag{2.10}$$

where u_* is friction velocity = $\sqrt{(\overline{uw} + \overline{vw})}$, κ is von Karman constant = 0.4, z is the measurement height considered, and z_o is surface roughness length. Offshore, surface roughness is variable and depends on the sea state. Using assumptions of steady winds and a wind and wave field in equilibrium, sea surface roughness length has been defined using a simple relationship suggested by Charnock [1955] and is given in *Equation 2.11*:

$$z_0 = \alpha_c \frac{{u_*}^2}{g} \tag{2.11}$$

where α_c is Charnock's parameter and g is the gravity acceleration constant. Typical values for Charnock's parameter fall within the range of 1.1 x 10^{-2} and 1.8 x 10^{-2} [Kraus and Businger, 1994], and vary based on wave age, wave height, water depth, fetch, and potentially, wind speed [Cheynet et al., 2017].

The logarithmic wind speed profile can also be calculated using a reference wind speed at a particular height, thus rearranging *Equation 2.10* as:

$$U(z) = U_{ref} \frac{\ln(z/z_o)}{\ln(z_{ref}/z_o)} \tag{2.12}$$

where z_{ref} is a reference height and U_{ref} is the mean wind velocity at z_{ref}. *Equation 2.10* and *2.12* can also be adjusted for unstable atmospheric conditions by using a stability correction function [DNV-RP-C205, 2010], giving a non-neutral wind profile in the surface layer [Sathe et al., 2013]:

$$U(z) = U_{ref} \frac{\ln(z/z_o) - \psi_m(z/L)}{\ln(z_{ref}/z_o) - \psi_m(z_{ref}/L)} \tag{2.13}$$

$$\psi_m(z/L) = 2\ln[1+x] + \ln[1+x^2] - 2\tan^{-1}(x)$$

$$x = \left(1 - 19.3(z/L)\right)^{\frac{1}{4}}$$

where ψ_m is the stability function (shown specifically for unstable conditions) and L is the Monin-Obukhov length. This stability function has been studied extensively using field measurements, most commonly using data from the 1968 Kansas experiment [Haugen et al., 1971]. According to Peña et al. [2008], when using MOST to correct the marine wind speed profile for non-neutral conditions, the resulting simplified expressions compare well with wind speed measurements up to 161 m a.m.s.l.

2.4 Turbulence & Turbulent spectra models

Wind turbulence, which is the fluctuating component of incoming wind, is considered a major cause of fatigue damage on wind turbines and is caused by the dissipation of the wind's kinetic energy into thermal energy through the development and breakdown of eddies [Kaimal and Finnegan, 1994]. These "energy-containing" eddies develop due to instabilities in the wind flow and hold a majority of the kinetic energy [Kaimal and Finnigan, 1994]. Wind turbulence is typically characterized using turbulence intensity (TI), which measures the fluctuation of wind speed about its mean value. Therefore, a larger value for TI would coincide with a larger fluctuation about the mean wind speed. Turbulent wind acts not only in the along wind direction (longitudinal), but also the cross wind (lateral) and vertical wind (vertical) directions. Typically, the along wind component is most influential on the loads on a structure, but it is important to consider all three components in order to fully capture the dynamic response of the wind turbine [Eliassen and Obhrai, 2016]. TI is defined as the ratio between the standard deviation and the mean of the wind velocity, at a particular height (z):

$$I_u(z) = \frac{\sigma_u(z)}{\bar{u}(z)} \tag{2.14}$$

$$I_v(z) = \frac{\sigma_v(z)}{\bar{u}(z)} \tag{2.15}$$

$$I_w(z) = \frac{\sigma_w(z)}{\bar{u}(z)} \tag{2.16}$$

where I_u, I_v, and I_w are turbulence intensity in the longitudinal, lateral, and vertical directions, respectively, σ is the standard deviation of wind speed, and $\bar{u}$ is the mean wind speed.

Typically, wind spectra are derived based on a combination of the "blunt model" and the "pointed model". The "blunt model" is suggested for perturbed terrain, while the "pointed model" is most commonly used for flat, smooth, and uniform terrains [Tieleman, 1995]. These models are expressed in *Equations 2.17* and *2.18* respectively.

$$\frac{nS(n)}{u_*^2} = \frac{Af}{(1+Bf)^{5/3}} \tag{2.17}$$

$$\frac{nS(n)}{u_*^2} = \frac{Af}{1+Bf^{5/3}} \tag{2.18}$$

As mentioned previously, the two most commonly used turbulence models that are detailed in the IEC standards to simulate wind fields and velocity spectra are: the IEC Kaimal Spectra & Exponential Coherence Model and the Mann Spectral Tensor Model. However, since these two models were originally developed for neutral conditions, this thesis will focus on the Højstrup 1981 Unstable Spectra Model and use the original Kaimal Spectra model as a comparison for neutral conditions.

Kaimal Spectra Model

Kaimal's spectral model for the horizontal spectra involves three parts: a low-frequency range which relates to the boundary layer height, a high frequency range relating to distance above ground, and an intermediate range, which was defined based on linear interpolation between the low and high frequency parts. Kaimal et al. [1972] concluded that each spectrum and co-spectrum could be simplified into single universal curves within the inertial subrange. Using this approach, their research then involved monitoring the behavior of the spectra with variations in z/L. According to [Kaimal et al., 1972], the Kaimal Spectra Model properly describes the energy content of turbulent wind in the surface layer, within the range of 0.01 Hz and 4 Hz, for neutral stability conditions.

The most commonly used equations for the Kaimal spectra in engineering applications are based on the neutral Kansas measurements and are adjusted to account for the 4/3 ratio that is expected in the inertial subrange [Kaimal and Finnigan, 1994]. These equations are as follows [Kaimal, 1972]:

$$\frac{nS_u}{u_*^2} = \frac{105f}{(1+33f)^{5/3}} \tag{2.19}$$

$$\frac{nS_v}{u_*^2} = \frac{17f}{(1+9.5f)^{5/3}} \tag{2.20}$$

$$\frac{nS_w}{u_*^2} = \frac{2f}{1+5.3f^{5/3}} \tag{2.21}$$

where n is frequency in Hertz, S_u, S_v, S_w are the velocity spectra in the along wind, cross wind, and vertical wind respectively, u_* is friction velocity, and $f = nz/\bar{u}$, a nondimensional reduced frequency. As will be seen in the next section, the Højstrup 1981 Unstable Spectra Model is an extension of the Kaimal Spectra Model.

Højstrup 1981 Unstable Spectra Model

The goal of Højstrup's 1981 Unstable Spectra Model was to develop a simple model that could resemble velocity spectra in unstable conditions downwind of a change in surface roughness and heat flux [Højstrup, 1981]. Since atmospheric turbulence consists of both a buoyancy-generated component and a mechanically generated component, Højstrup found it important to create a full-scale velocity spectrum that involves both aspects and can be modeled as the sum of two semi-empirical spectra. This can be seen in *Equation 2.22* [Højstrup, 1981]:

$$S(n) = S_L(n) + S_m(n) \tag{2.22}$$

with $S_L(n)$ corresponding to the low frequency part of the spectra and $S_m(n)$ corresponding to the Kaimal Spectra Model. The backbone of the model involves a strong emphasis on incorporating both a buoyancy-produced part (low frequencies) and a shear-produced part (high frequencies), thus creating the following equations [Højstrup, 1981]:

$$\frac{nS_u}{u_*^2} = \frac{0.5f_i}{1+2.2f_i^{5/3}}\left(\frac{z_i}{-L}\right)^{2/3} + \frac{105f}{(1+33f)^{5/3}} \tag{2.23}$$

$$\frac{nS_v}{u_*^2} = \frac{0.32f_i}{1+1.1f_i^{5/3}}\left(\frac{z_i}{-L}\right)^{2/3} + \frac{17f}{(1+9.5f)^{5/3}} \tag{2.24}$$

$$\frac{nS_w}{u_*^2} = \frac{32f}{(1+17f)^{5/3}}\left(\frac{z}{-L}\right)^{2/3} + \frac{2f}{1+5.3f^{5/3}} \tag{2.25}$$

For neutral conditions, when $L = \infty$, *Equations 2.23*, *2.24*, and *2.25* reduce to the Kaimal spectrum. By comparing these equations with Equations *2.17* and *2.18*, it can be seen that the Højstrup model follows the conditions of the pointed and the blunt model by using a combination of both. The key variables of the model are the three scaling lengths: height (z), inversion height (z_i), and Monin-Obuhkov length (L). Another important aspect is the reduced frequency parameters, f and f_i, which are nondimensionalized and provide knowledge of the spectra's variation with stability [Olesen, 1984]. These parameters are defined in *Equations 2.26* and *2.27* [Højstrup, 1981]:

$$f = \frac{nz}{\bar{u}} \tag{2.26}$$

$$f_i = \frac{nz_i}{\bar{u}} \tag{2.27}$$

where n is frequency in Hertz and $\bar{u}$ is the mean wind speed. In order to normalize all spectra, Højstrup used the frequency and friction velocity, u_*. Friction velocity can be substituted as a local value or defined through the use of *Equation 2.28* [Højstrup, 1982], with u_{*0} equal to the initial friction velocity.

$$u_* \approx u_{*0}(1 - \left(\frac{z}{z_i}\right)) \tag{2.28}$$

The formulas for the horizontal spectra can be seen as the summation of two parts, with a slight variation in the shape of the spectrum between the u-component and the v-component. These discrepancies were based on data from the Kansas and Minnesota experiments, which led to the chosen shape parameters [Højstrup, 1982]. According to these parameters, the Højstrup model defines a v-spectrum which is above the u-spectrum for low frequencies. Within the Højstrup model, the comparison of v- to u- spectra at high frequencies approaches 4/3, which coincides with the idea of isotropy (same physical property in all directions), and describes Kolmogorov's hypothesis of local isotropy in the inertial subrange [Kolmogorov, 1941]. However, this ratio may not necessarily be observed for stable atmospheric conditions.

The constants used in *Equations 2.23* and *2.24* were also chosen in order to be consistent with the defined expression for the dimensionless dissipation rate for turbulent kinetic energy: $\phi_\varepsilon = kz\varepsilon/u_*^3$ [Højstrup, 1981]. For the Kaimal part of the spectrum, $S_m(n)$, this dissipation rate is equal to one. However, for the low frequency part of the spectrum, where buoyancy production plays a role, the dissipation rate becomes $\phi_\varepsilon^{2/3} = 1 + 0.75\left(\frac{z}{L}\right)^{2/3}$. This shifts the spectra slightly towards higher frequencies with a peak frequency (non-dimensional) of 0.8 instead of 0.65 for the u-spectra and a peak frequency of 1.2 instead of 0.65 for the v-spectra.

The w-spectrum is modelled similarly to the horizontal spectra, but scales with the height above ground rather than the inversion height within the low frequency range [Højstrup, 1981]. This is due to the limiting factor of a solid surface, which affects the vertical velocity fluctuations without a reliance on stability and inversion height.

Højstrup also considered the influence of small-scale eddies originating within the surface layer, as well as large-scale eddies from above the surface layer, scaling based on parameters associated with the origin of the eddies [Olesen et al., 1984]. These considerations enabled the Højstrup model to further define the spectral shape of the horizontal spectra, as well as the vertical spectra. By including the effect of different eddy sizes, it would make sense for the unstable horizontal spectra to have two peaks, since it involves a superposition of two components with different scaling parameters. However, the spectra can be simplified within a frequency range corresponding to turbulent motion, thus creating a smooth curve with one peak. The effect of different eddy sizes can be seen in *Figure 2.3*, showing an example of the two components of the v-spectrum plotted as a function of reduced frequency. The two peaks are seen most prominently in the v-spectrum at distances close to the ground where the shear-produced part and the buoyancy-produced part are further apart [Højstrup, 1981].

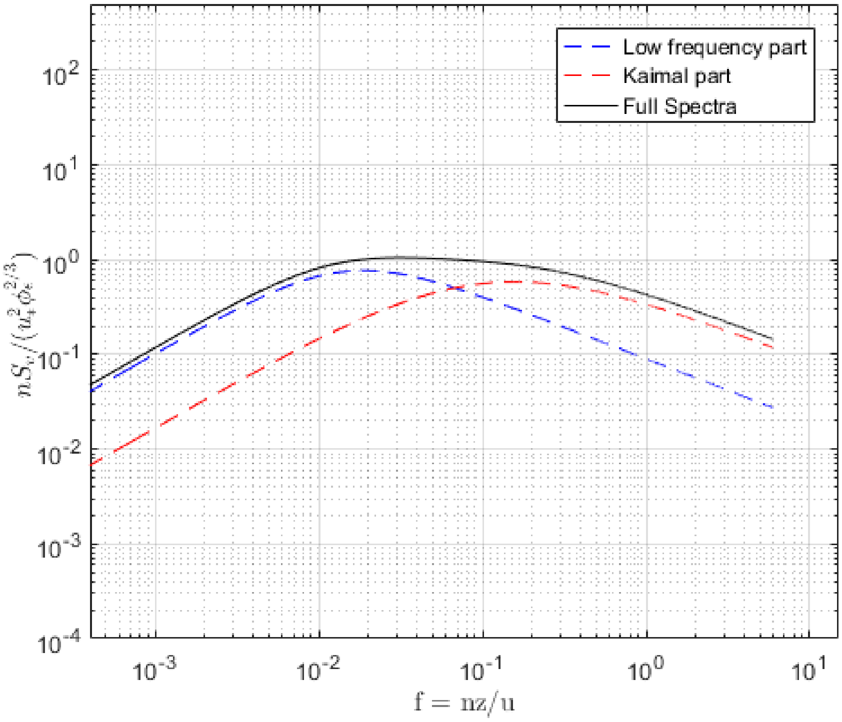

Figure 2.3: Højstrup model for the v-spectrum

2.5 Coherence & Coherence models

Wind coherence is the normalized cross-spectrum of the fluctuations in velocity, and expresses how eddies of different sizes are correlated in two or more different points in space [Panofsky, 1974]. Wind coherence has been included in research studies relating to wind turbulence since the 1960s [Cheynet et al., 2018, Panofsky and Singer, 1965, Davenport, 1961, Panofsky et al., 1958]. Many projects were concerned with the correlation between wind speed and temperature fluctuations [Panofsky and Singer, 1965], or the decay parameters associated with co-coherence. The normalized co-spectrum of the velocity fluctuation is known as co-coherence, and is the real part of the coherence function. Throughout the rest of this paper, co-coherence will be referred to as coherence, unless otherwise specified.

There are two recognized definitions of coherence: a square root definition and a squared definition. This thesis will consider the square root coherence definition as given in Højstrup [1999]:

$$\gamma(n) = \sqrt{\frac{Co^2(n)+Q^2(n)}{S_1(n)\, S_2(n)}} \tag{2.29}$$

where n is the frequency in Hz, Co is the co-spectrum density/real part of the cross-spectrum, Q is the quadrature spectrum density/imaginary part of the cross-spectrum, and $S_1(f)$ & $S_2(f)$ are the spectral densities of the velocity components. A coherence equal to one can be interpreted as all frequencies, within the range specified by n, are perfectly correlated given a separation distance, and a coherence near or equal to zero means all frequencies are poorly correlated for a given separation distance [Ropelewski et al., 1973].

Davenport Exponential Coherence Model

A suitable model for vertical coherence, when the separation between points are small in comparison to the length scale of turbulence, is the Davenport Exponential Coherence Model, displayed in *Equation 2.30* [Davenport, 1961]:

$$\gamma_i(d_z, n) \approx \exp\left(\frac{-\mathrm{C}_{\mathrm{z}}^{\mathrm{i}}\, n\, d_z}{\bar{u}}\right) \tag{2.30}$$

where $i = \{u, v, w\}$, d_z is the vertical separation distance between points, n refers to the frequency in Hz, $\bar{u}$ is the horizontal mean velocity, and C_z^i is a decay coefficient in the z-direction. The Davenport Coherence Function proposes a simple approximation, which suggests that coherence depends only on the ratio of the vertical separation distance to the horizontal wave length of the correlated eddies, in the direction of the mean wind [Panofsky and Singer, 1965]. In his studies, Davenport [1961] considered strong wind conditions, meaning near-neutral stability, and concluded that the coherence between wind speed fluctuations was a universal function of the nondimensional frequency f:

$$\Delta f = \frac{n\, d_z}{\bar{u}} \tag{2.31}$$

To account for the influence that both horizontal and vertical separations have on the coherence, *Equation 2.30* was adjusted by Pielke and Panofsky [1970] to include horizontal separations [Ropelewski, 1972]:

$$\gamma_i(d_y, d_z, n) \approx \exp(-\sqrt{\left(C_y^i\, d_y\right)^2 + \left(C_z^i\, d_z\right)^2} * \frac{n}{\bar{u}}) \tag{2.32}$$

where d_y is the horizontal separation distance between points and C_y^i is a decay coefficient in the y-direction.

Modified Coherence Model

Although the Davenport Coherence Model is commonly used in wind engineering, there are concerns regarding the characterization of the wind coherence using only one decay coefficient [Cheynet, 2018], as well as a lack of emphasis on the relationship of coherence to atmospheric stability. The decay coefficients seen in *Equation 2.32* have been evaluated as a large range of values within different research studies since coherence is influenced by numerous parameters, such as spatial separation, measurement height, mean wind speed, wind shear, atmospheric stability, turbulence intensity, etc. [Panofsky and Singer, 1965, Davenport, 1961, Panofsky et al., 1958]. In terms of including the influence of atmospheric stability, the research of Soucy et al. [1982] concluded that the decay coefficient increases with increasing stability, z/L, for z/L < 0.5. This is in line with the research of Pielke and Panofsky [1970] and Panofsky and Singer [1965], both of which confirmed the findings of Davenport [1961], but went further to suggest that the coefficients are related to atmospheric stability conditions. To investigate the factors affecting the decay parameter, Ropelewski et al. [1973] analyzed measurements collected at four meteorological sites and data collected in a wind-tunnel experiment. Results showed that the decay parameters were functions of stability and the angle between the mean wind and the anemometer line.

Based on these findings, it seems beneficial to address a modified coherence function to better depict wind coherence. Cheynet et al. [2018] derived a coherence function using decay coefficients with a dependency on spatial separation and atmospheric stability. This coherence function is first displayed in *Equation 2.33* as a two-parameter set-up (a dimensionless decay coefficient in the z-direction and an additional coefficient with the dimensions of the inverse of a time scale) to describe the coherence of the vertical velocity component. To also account for the coherence of the horizontal velocity component, *Equation 2.33* was adjusted to include a dimensionless decay coefficient in the y-direction, as seen in *Equation 2.34*.

$$\gamma_i(d_z, n) \approx \exp\left[-\sqrt{\left(\frac{c_z^i\, n\, d_z}{\bar{u}}\right)^2 + \left(\frac{d_z}{l_2}\right)^2}\right] \tag{2.33}$$

$$\gamma_i(d_y, d_z, n) \approx \exp\left[-\sqrt{\left(\frac{c_y^i\, n\, d_y}{\bar{u}}\right)^2 + \left(\frac{c_z^i\, n\, d_z}{\bar{u}}\right)^2 + \left(\frac{d_z}{l_2}\right)^2}\right] \tag{2.34}$$

where $l_2 = \bar{u}/c_2^w$ and c_2^w [1/time] corresponds to a second decay coefficient, which is only applied in the vertical wind direction. Setting this second decay coefficient to zero would reduce the equation to the Davenport Coherence Model. Unfortunately, the dimensionless decay coefficients in the y-direction have yet to be defined for atmospheric stability. However, the dimensionless decay coefficients in the z-direction, as well as the additional decay coefficient, are defined in [Cheynet et al., 2018] to account for stability conditions (-2 < z/L < -0.2) and were derived from FINO1 data:

$$c_z^u = 11 + 1.8\exp(4.5\frac{z}{L}) \tag{2.35}$$

$$c_z^v = 7.1 + 3.4\exp(6.8\frac{z}{L}) \tag{2.36}$$

$$c_z^w = 3.5 + 0.7\exp(2.5\frac{z}{L}) \tag{2.37}$$

$$c_2^w = 0.05 + 0.13\exp(5\frac{z}{L}) \tag{2.38}$$

3. Methodology

The simulations for this thesis were based on the spar-buoy type FOWT, a ballast stabilized concept, from Phase IV of the IEA Annex XXIII Offshore Code Comparison Collaboration (OC3) project [Jonkman, 2010]. This phase uses the offshore 5 MW standard wind turbine of the National Renewable Energy Laboratory (NREL) in conjunction with the spar-buoy concept that was used within the “Hywind” project developed by Equinor. The NREL 5 MW offshore wind turbine has three blades, a hub height of 90 m above still water level (SWL), and a rotor diameter of 126 m, including hub diameter. The cut-in, rated, and cut-out wind speeds are given as 3, 11.4, and 25 m/s, respectively. This study will use rated wind speed for the analysis, as well as 8 m/s for a below rated scenario and 15 m/s for above rated. The OC3 project kept the same aerodynamic and structural characteristics of the 5 MW NREL wind turbine, but altered the support and control system. *Table 3.1* gives a summary of some of the specifications for the NREL 5 MW offshore wind turbine [Jonkman, 2010].

Table 3.1: Specifications for NREL 5 MW Offshore Wind Turbine

Parameter	NREL 5 MW Wind Turbine
Power Production Rating	5 MW
Number of Blades	3
Rotor Orientation	Upwind
Rotor Diameter	126 m
Hub Height	90 m
Cut in, Rated, Cut out Wind Speed	3 m/s, 11.4 m/s, 15 m/s
Cut in, Rated Rotor Speed	6.9 rpm, 12.1 rpm

The draft of the OC3-Hywind floating platform is 120 m, placed in a water depth of 320 m, and anchored using three catenary mooring lines, each positioned 120˚ from one another. The tower structure is connected to the platform 10 m above SWL. The OC3-Hywind system has been used for developing aero-hydro-servo-elastic models and is further described in a report by J. Jonkman [2010]. *Figure 3.1* displays an illustration of the OC3-Hywind spar-buoy FOWT [Jonkman, 2010].

Figure 3.1: Illustration of the 5 MW NREL wind turbine on the OC3-Hywind spar-buoy FOWT

In addition to the OC3-Hywind spar-buoy, the semi-submersible design from Phase II of the Offshore Code Comparison Collaboration Continuation (OC4) project [Robertson, et al., 2014], an extension of the OC3 project, was used as a way to investigate the influence of atmospheric stability on different FOWT foundation types. The semi-submersible design used in the project was originally developed for DeepCwind, a U.S. based project involved in validating FOWT modeling tools. In the OC4 Phase II, the NREL offshore 5 MW baseline wind turbine was used, just as in the OC3 Phase IV, which means the number of blades, rotor diameter, hub height, rotor speed, and cut-in, rated, and cut-out wind speeds remain the same. Similar to the OC3-Hywind spar-buoy, the semi-submersible foundation is positioned using 3 mooring lines, with 120˚ between adjacent lines, and is connected to the tower structure 10 m above SWL. The draft of the floating platform for the semi-submersible design is 20 m and is placed in a water depth of 200 m. The platform consists of a main column, which is situated in the middle of the platform and is attached to the tower structure. The platform also includes three offset columns, each connected to the main column using pontoons and cross members. This arrangement can be seen in the illustration in *Figure 3.2*. Additional information can be found in [Robertson, et al., 2014].

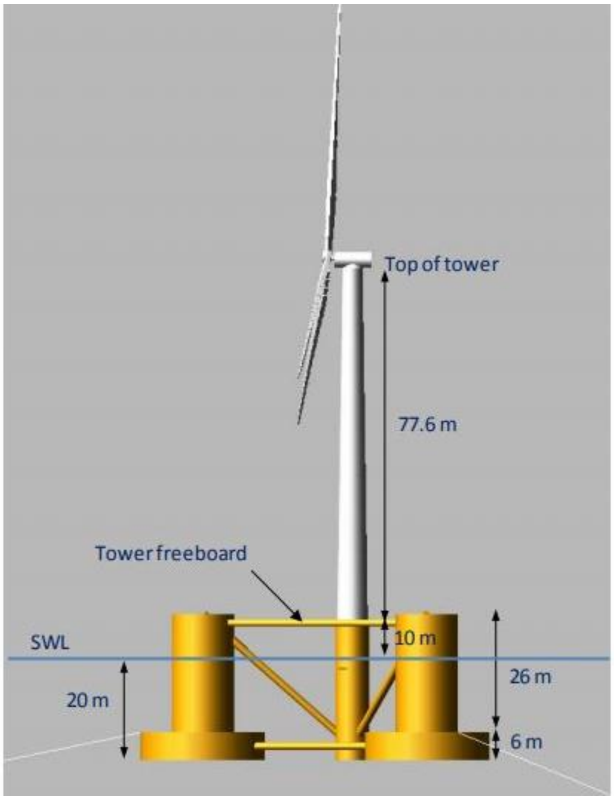

Figure 3.2: Illustration of the DeepCwind semi-submersible design used in the OC4 project

Currently, the semi-submersible design concept is being used within Principle Power's WindFloat foundation design for FOWTs, which was successfully used in the deployment of a full-scale 2 MW prototype off the coast of Portugal [www.principlepowerinc.com, accessed 2019]. Principle Power's design is slightly different than the OC4-DeepCwind design, in that the turbine tower of WindFloat is positioned on one of the offset columns rather than the one directly in the middle of the platform. The future WindFloat designs will build upon the success of the prototype, with potential specifications including: a power rating of approximately 5-10 MW, rotor diameter between ~120-190 m, turbine hub height of ~80-110 m, operational water depth greater than 40 m, hull draft less than 20 m, and 3-4 conventional mooring line components. The semi-submersible design is a hybrid of the buoyancy stabilized, ballast stabilized, and mooring stabilized concepts, whereas the spar-type is classified as ballast stabilized [Bui, 2018]. A summary of some of the properties of the OC3-Hywind spar-buoy and OC4-DeepCwind semisubmersible foundations is displayed in *Table 3.2*.

Table 3.2: Properties of the two floating platforms

Parameter	Spar	Semisubmersible
Water depth (m)	320	200
Draft (m)	120	20
Elevation of Main Column above SWL (m)	10	10
Number of Mooring Lines	3	3
Angle between Adjacent Lines	120˚	120˚
Platform Roll Inertia about CM (kg*m^2)	4.229E9	6.827E9
Platform Pitch Inertia about CM (kg*m^2)	4.229E9	6.827E9
Platform Yaw Inertia about CM (kg*m^2)	1.642E8	1.266E10

Theoretically, the response of a FOWT is largely influenced by the natural frequencies of the system. The natural/eigen frequencies of the first 10 modes of the OC3-Hywind FOWT [Jonkman et al., 2010] and the OC4-DeepCwind FOWT [Robertson et al., 2014] are displayed in *Table 3.3.*

Table 3.3: Eigen frequencies for the first 10 modes of the OC3-Hywind & OC4-DeepCwind FOWTs

Mode	Platform Motion	Spar	Semisubmersible
1	Surge	0.008 Hz	0.01 Hz
2	Sway	0.008 Hz	0.01 Hz
3	Heave	0.032 Hz	0.058 Hz
4	Roll	0.034 Hz	0.04 Hz
5	Pitch	0.034 Hz	0.04 Hz
6	Yaw	0.11 Hz	0.012 Hz
7	1st Tower fore-aft	0.43 Hz	0.43 Hz
8	1st Tower side-side	0.44 Hz	0.43 Hz
9	Drivetrain torsion	0.63 Hz	0.63 Hz
10	Blade flap-wise	0.64 Hz	0.64 Hz

The primary tools used for analyzing the Højstrup 1981 Unstable Spectra Model were MATLAB and Simulation Workbench for Marine Application (SIMA), and specifically the coupled SIMO-RIFLEX program within SIMA. Using the simulation results, the fatigue loads for each FOWT were analyzed using the concept of damage equivalent load (DEL). In addition to assessing the effect that the Højstrup spectra has on the loads and motions on a FOWT, the scope of this thesis also involves comparing the motions and fatigue damages to the Kaimal Spectra Model, the Højstrup 1981 Unstable Spectra Model with varying coherence, along with the results of other research projects, including the study by Putri [2016] and the research of Bachynski and Eliassen [2019]. The results of Putri [2016] were found using HAWC2 aero-hydro-servo-elastic code, so a slightly different model was used, whereas Bachynski and Eliassen [2019] obtained results also using SIMA. Both studies focus on the turbulent wind models recommended in the IEC standards, although Putri [2016] also included an analysis of the fitted Mann model, which was adjusted using fitted parameters from Sathe et al. [2013] to resemble stable, neutral, and unstable atmospheric conditions.

3.1 Wind Simulation Model

In order to analyze the velocity spectra of the Højstrup model, a MATLAB script was used to determine the spectra for the u, v, and w components based on *Equations 2.23*, *2.24*, and *2.25*. The spectral representation approach was then used to simulate turbulent wind fields using the method from Shinozuka and Deodatis [1991]. A function called WindSimFast [Cheynet, 2018], available on MathWorks File Exchange, was utilized within this approach based on the input variables: frequency, the specified Y-Z grid, the Højstrup spectra, and the decay coefficients. To allow for the simulations to closely resemble the stochastic nature of wind and waves and to minimize uncertainty, six random seeds were defined within the script to generate the velocity histories. This means that each scenario, based on stability conditions, coherence, wind speed, etc., was run six times in MATLAB. Each seed could then be analyzed separately for the fatigue damages and motion responses.

3.1.1 Frequency & Y-Z Grid

The sampling frequency for the simulations were based on the number of time steps, N = 2^M, divided by the duration of the time series. In this case, M was set to 15, and the time duration was one hour (3600 seconds), giving a sampling frequency of approximately 9.1 s. One hour was chosen to reduce the uncertainties in the wind turbulence and to include the low frequency behavior of the turbulent wind, since low frequencies tend to be important for the motion response of a FOWT. However, simulations were run for no more than an hour since a duration longer than this may stray from the idea of a stationary wind field [Cheynet et al., 2018]. The sampling frequency was then used to determine the range of frequencies for the simulation, which was limited by the Nyquist frequency to avoid aliasing.

In order to make a valid comparison with the results from the study by Putri [2016], a Y by Z grid over the specified time duration was defined to match the one from the study. Thus, a 32768 x 32 x 32 (t x Y x Z) grid was generated with a t range from 0 to 32,768 s (N = 2^M), a Y range from -77.5 to 77.5 m, and a Z range from 12.5 to 167.5 m. After running the simulation, each grid point corresponded to a spatial location within the generated wind field and a local wind speed for the along wind, cross wind, and vertical wind direction. This grid created a 3D turbulence box which encompassed the rotor swept area of the wind turbine. A simplified sketch of the dimensions of the 3D turbulence box is displayed in *Figure 3.3* (original image of the wind turbine was taken from www.pinterest.com).

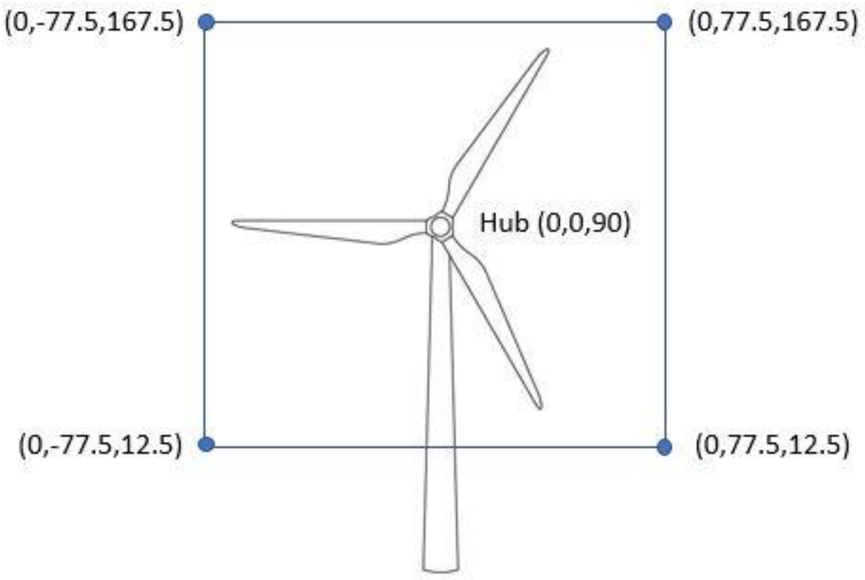

Figure 3.3: Basic dimensions of 3D turbulence box (t, Y, Z)

3.1.2 Højstrup Spectra Model Parameters

1968 Kansas & 1973 Minnesota Experiments

Højstrup's 1981 Unstable Spectra Model was developed using the published measurements from the experiments in both Kansas, USA (1968) and Minnesota, USA (1973) [Højstrup, 1981]. The 1968 Air Force Cambridge Research Laboratories (AFCRL) experiment in Kansas [Haugen et al., 1971] was conducted with the aim of gathering data on wind and temperature fluctuations across a flat, uniform plain [Kaimal et al, 1972]. The results provided a clear representation of the turbulence structure within the surface layer, but highlighted the need for additional data collection. The AFCRL experiment in Minnesota, conducted 5 years after the Kansas experiment, also used conditions of a flat and uniform site, this time located in northwestern Minnesota, in order to further the research of the Kansas experiment.

The techniques used for data collection in Kansas involved three-axis sonic anemometers, hot-wire anemometers, and fine platinum wire thermometers positioned at three locations along a 32 m tower.

Standard cup anemometers were set up at eight levels along the tower to measure mean wind speed and temperature gradients, and approximately 50-80 m from one side of the tower, two CSIRO drag plates were situated to measure surface stress and friction velocity. Analog signals from the instruments were collected 20 times a second, although measurement collection was halted after 5 minutes. This arrangement shows a limitation of the Kansas data, since the 5-minute cut-off may have created the effect of a high pass filter. For data analysis, fifteen 1-hour runs were selected, corresponding to 10 unstable conditions and 5 stable conditions. Further details of the 1968 Kansas experiment can be found in [Haugen et al., 1971]. By the time of the 1973 AFCRL Minnesota experiment, scientists at the Meteorological Research Unit (MRU) developed an idea to attach turbulence probes to the tethering cable of large, captive balloons. After establishing the compatibility of this technique with that of tower-based measurements, it was given the go ahead to apply it in conjunction with the techniques used in Kansas. In Minnesota, the turbulence probes on both the tower and the balloon cable were sampled 10 times a second, and wind and temperature data sampled every second, although data collection only took place during a northerly wind and when the sky was clear. More information about the Minnesota experiment can be found in [Kaimal et al., 1976].

From the efforts in Kansas and Minnesota, data was obtained regarding the structure of turbulence in the atmospheric boundary layer, based on measurements such as wind speed, potential temperature, boundary layer height, etc. [Kaimal et al., 1976]. Boundary layer height, or the height of lowest inversion (zi), was found to be another important parameter for determining the velocity spectra. With that being said, the Kansas experiment assumed a constant inversion height of 1000 m for all runs, while the Minnesota experiment measured the inversion height through the use of five probes attached at 5 locations along a tethering cable of a 1300 m^3 kite balloon. The value for the inversion height was determined from the measurements of wind and temperature fields, and was taken as the location where the distribution of wind speed and potential temperature were no longer near-constant and exhibited a sharp increase.

Input Parameters

According to data collected in the 1968 Kansas experiment, the most unstable conditions corresponded to a value of -0.5 for the dimensionless Obukhov stability parameter (z/L) [Højstrup, 1982]. However, the most unstable conditions in the study by Cheynet et al. [2018] were within the range of -2 and -1. With a hub height of about 90 m (standard value for the NREL 5 MW wind turbine), an Obukhov stability parameter of -0.5 gives a value for the Monin-Obukhov length (L) of -180 m. In order to also capture more unstable conditions, a value for the Obukhov stability parameter of -1 was used for this study along with -0.5. This correlates to a value for L of -90 m. Referring back to atmospheric stability classes in *Table 2.1*, these two values for the Monin-Obukhov length fall under the categories "very unstable" for L = -90 m and "unstable" for L = -180 m, and will be referred to as such for the analysis of this thesis.

Friction velocity was calculated using *Equation 2.28*, and the initial friction velocity was set equal to 0.4 m/s. Since the neutral atmospheric boundary layer height is between 500 and 1000 m in the MABL, and increases in convective conditions, an inversion height of 1000 m was chosen and utilized for this study. To calculate the mean wind speed along the height of the wind turbine, the corrected logarithmic wind speed profile for unstable conditions was selected. In this case, the reference height was set equal to the hub height of 90 m and surface roughness was set to 0.00014 m, based on measurements from Sathe et al. [2013]. The mean wind speed at hub height, U_{ref}, was substituted based on the appropriate wind speed associated with below, above, and rated wind speed. *Figure 3.4* displays an example of the logarithmic wind profile, corrected for very unstable conditions (L = -90 m), used for a rated wind speed scenario.

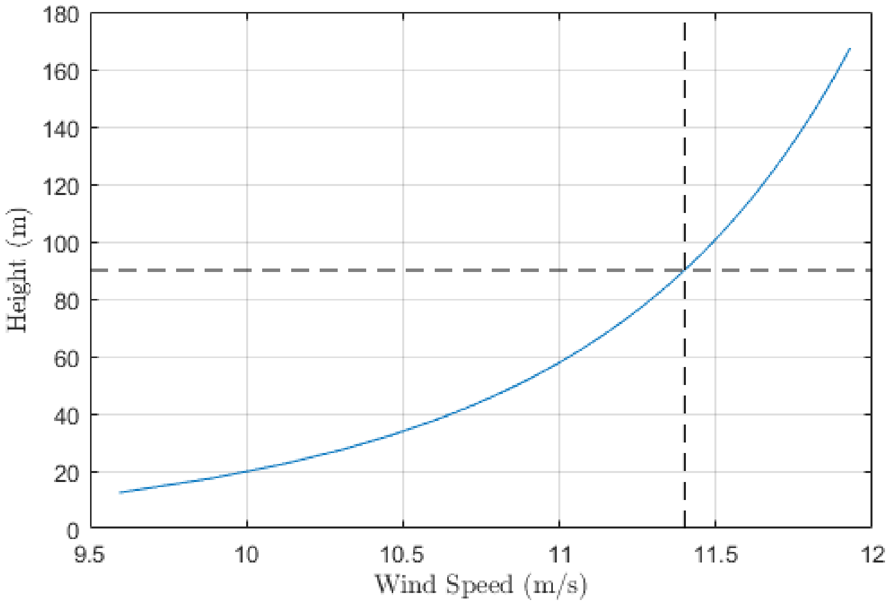

Figure 3.4: Corrected Logarithmic Wind Profile for unstable conditions using rated wind Speed (11.4 m/s) at the 90 m hub height

3.1.3 Decay Coefficients

Another important concept needed to generate an appropriate wind field is the coherence model and specifically, the decay coefficients. When applying the Davenport Coherence Function, the decay coefficients used were similar to those found in the study by Solari and Piccardo [2001]. In their study, the decay coefficients derived from measurements were averaged for each combination of {x, y, z} and {u, v, w} and are the same coefficients listed in the N400 handbook, which are specifically defined for bridge engineering. For this thesis, these decay coefficients were adjusted slightly for determining the coherence and can be seen in *Table 3.4*.

Table 3.4: Decay Coefficients for Davenport Coherence

Coefficient	c_y^u	c_y^v	c_y^w	c_z^u	c_z^v	c_z^w
Value	7	7	6.5	10	10	3

When using the Modified Coherence Function, the vertical decay coefficients (z-direction) were determined using *Equations 2.35 – 2.38*, displayed earlier in **Section 2.5**. In order to visualize how this new coherence function would alter the results of the simulations, two cases were carried out. The first case (Case 1) involved fixing the horizontal decay coefficients (y-direction), while varying the vertical decay coefficients (z-direction). This was accomplished by using the two chosen Monin-Obukhov lengths (L = -90 m and L = -180 m), which altered the vertical decay coefficients due to their reliance on stability conditions. In this scenario, the horizontal decay coefficients were chosen as 11 for the along wind and cross wind, and 5.5 for the vertical wind (equal to half the along wind and cross wind coefficient).

For the second case (Case 2), the vertical decay coefficients remained the same and the horizontal decay coefficients were varied. Here, the horizontal decay coefficients defined in Case 1 were again used, but were also changed to 9 for the along wind and cross wind, and 4.5 for the vertical wind. The values for Case 1 and Case 2 are summarized in *Table 3.5* and *3.6*, respectively. As *Table 3.5* shows, the vertical decay coefficients increase with increasing stability conditions (z/L), which was also suggested by Soucy et al. [1982]. Recall that a Monin-Obukhov length of L = -90 m corresponds to z/L = -1, and L = -180 m corresponds to z/L = -0.5.

Table 3.5: Decay Coefficients for Modified Coherence Case 1

Coefficient	c_y^u	c_y^v	c_y^w	c_z^u	c_z^v	c_z^w	c_2^w
Case 1a (L = -90m)	11	11	5.5	**11.02**	**7.10**	**3.56**	**0.051**
Case 1b (L = -180m)	11	11	5.5	**11.19**	**7.21**	**3.70**	**0.061**

Table 3.6: Decay Coefficients for Modified Coherence Case 2

Coefficient	c_y^u	c_y^v	c_y^w	c_z^u	c_z^v	c_z^w	c_2^w
Case 2a (L = -90m)	**11**	**11**	**5.5**	11.02	7.10	3.56	0.051
Case 2b (L = -90m)	**9**	**9**	**4.5**	11.02	7.10	3.56	0.051

3.1.4 Kaimal Spectra Model Parameters

The Kaimal Spectra Model was set up in a similar way as the Højstrup model, with all associated parameters for the simulation remaining the same. However, since the Kaimal spectra model is associated with neutral atmospheric conditions, $L = \infty$, the logarithmic wind speed profile without the stability correction was applied. Additionally, only the Davenport Exponential Coherence Model was used with the Kaimal model.

3.1.5 Target Spectra for the Højstrup Model & the Kaimal Model

Before running simulations, the Højstrup and the Kaimal model were analyzed to obtain a proper understanding of the simulated spectra. *Figure 3.5* displays the normalized target spectra for the Højstrup 1981 Unstable Spectra Model with very unstable (L = -90 m) and unstable (L = -180 m) atmospheric stability conditions, as well as the Kaimal spectra model, resembling neutral conditions, at the lowest part of the rotor (30 m).

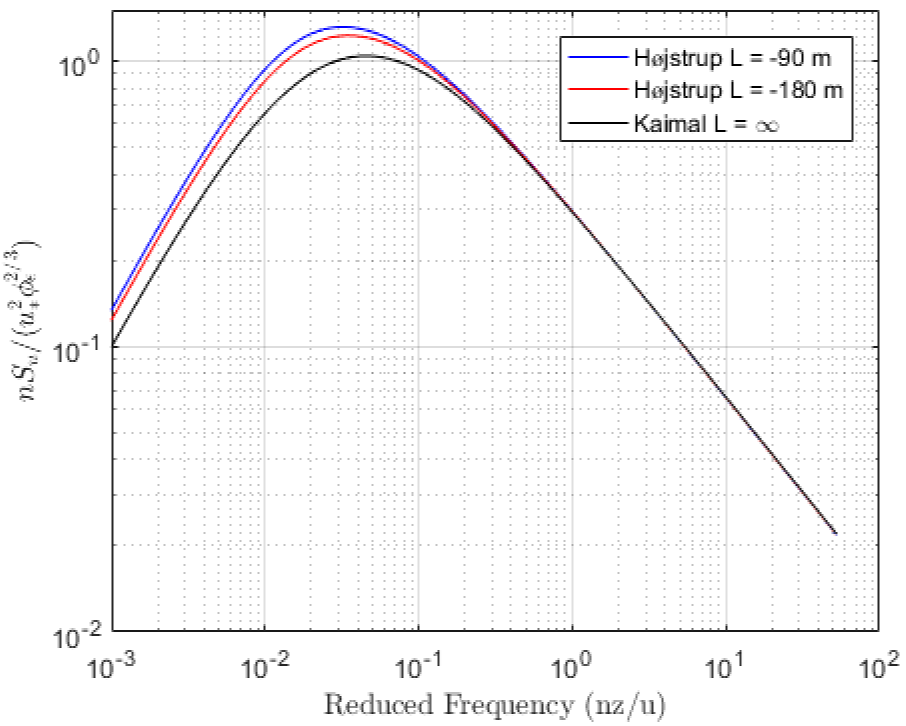

Figure 3.5: Normalized target spectra in the along wind direction at the lowest part of the rotor (30 m)

As was discussed earlier in **Section 2.4**, the Højstrup model was designed using a combination of a low frequency part $S_L(n)$, which is entirely buoyancy produced, and a high frequency part $S_m(n)$, which corresponds to shear production. Given that the high frequency part of the Højstrup model is identical to the Kaimal model, it makes sense that the resulting spectra would converge at high frequencies, as can be seen in *Figure 3.5*. Additionally, special attention should be paid to the low frequency behavior of the spectra, since platform motions near the wave peak frequency may cause significant problems for the FOWT.

3.1.6 Turbulence Intensity

For this study, turbulence intensity was not defined prior to running the MATLAB simulations, but was instead determined based on the simulated wind field. Therefore, part of the MATLAB script involved calculating the turbulence intensity by finding the standard deviation and mean of the simulated velocity spectra. Turbulence intensity is an important part of classifying a wind field and is strongly connected to atmospheric stability. For instance, mechanical turbulence is known to cause shear instability for stable atmospheric conditions, whereas, buoyant turbulence may cause buoyancy instability, which is associated with unstable atmospheric conditions [Obhrai, 2018]. Considering that one of the main objectives of this study is to calculate the fatigue loads on a FOWT, it is also interesting to look at the variance of the mean wind speed, since the variance is what gets translated into the fatigue load. *Figure 3.6* shows the resulting turbulence intensity and wind speed variance for the along wind component at the 90 m hub height, averaged for the six seeds, when varying stability conditions. The three points seen on each curve depict the turbulence intensity at below rated, rated, and above rated wind speeds. Based on the figure, it can be seen that the Højstrup model with very unstable conditions corresponded to a higher turbulence and a larger variation in wind speed than unstable and neutral conditions.

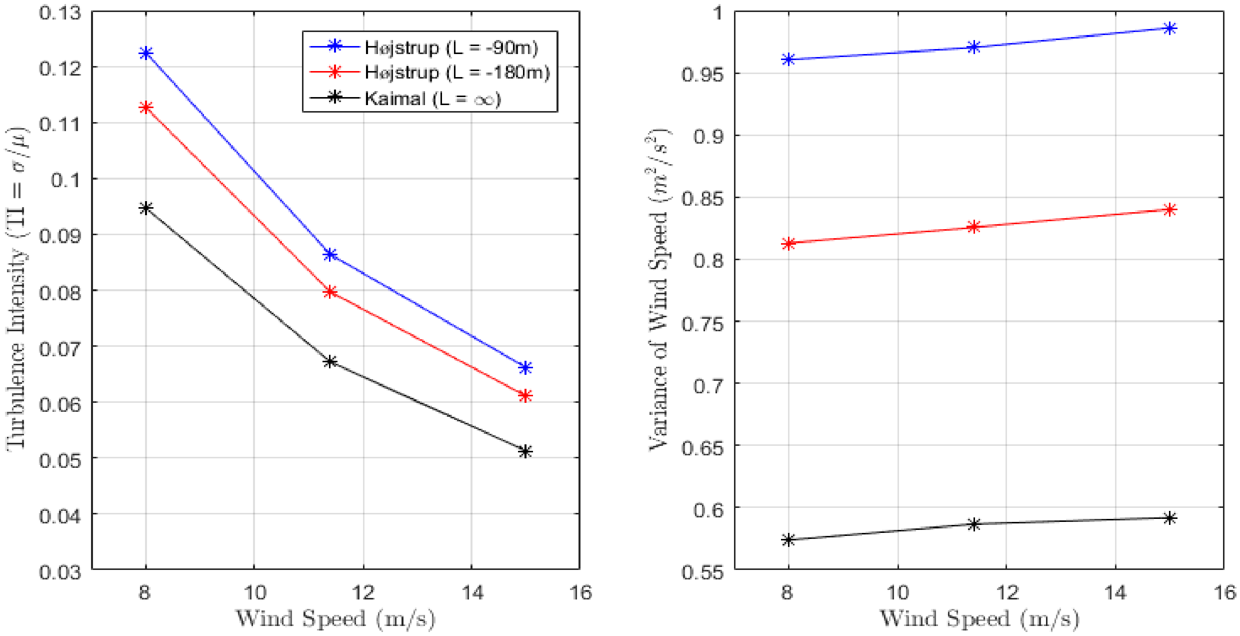

Figure 3.6: Turbulence Intensity and variance of wind speed, associated with simulations using the Højstrup model with varying stability for below rated, rated, and above rated wind speeds

3.2 SIMO-RIFLEX Aerodyne

A FOWT with the specified characteristics of this study was implemented in SIMA, a simulation and analysis tool developed by SINTEF Ocean [Karimirad, M., accessed 2019]. Within SIMA, there is a SIMO-RIFLEX coupling tool that allows for the simulation of multi-body hydrodynamics. Separately, SIMO is capable of modelling flexible multibody systems within a non-linear time domain, and RIFLEX was specifically designed to analyze slender marine structures, while including aerodynamic forces acting on the members. For this study, the example spar-buoy FOWT stored within SIMO-RIFLEX was used and adjusted to model the environment needed to properly analyze the Højstrup model. The turbine tower and blades were modelled with nonlinear beam elements, and the mooring lines were modelled with nonlinear bar elements, which allowed for the rotation of each element [Bachynski and Eliassen, 2019]. In addition, the semisubmersible type FOWT, supported by the NREL 5 MW baseline wind turbine, was provided by SINTEF, one of the major research organizations in Europe. The semisubmersible design is characterized by a large moment of inertia at the waterplane area, giving the platform stability, despite having a shallow draft. Comparatively, the spar-buoy has a small waterplane area, a large draft, and a heavy ballast, which provides stability for the platform [Bachynski and Eliassen, 2019]. After importing the semi-submersible FOWT into SIMA, the environment was modified to match the scenarios used for the spar-buoy FOWT, and the dynamic calculation parameters were altered to match the new design, since the components of the semisubmersible design varied in comparison to the spar-buoy.

The environmental loads implemented in this study included the influence of both wind and waves. The waves were defined using irregular airy waves based on the Joint North Sea Wave Project (JONSWAP) wave spectrum [Hasselmann et al., 1973]. Inputs included a peak parameter (γ) = 3.3, significant wave height (H_s) = 6 m, and a peak period (T_p) = 12 s. This peak period corresponds to a peak wave frequency (f_p) of 0.083 Hz, which is the highest wave excitation for these conditions. The power spectral density of the JONSWAP wave spectrum, using the desired input parameters, is displayed in *Figure 3.7*.

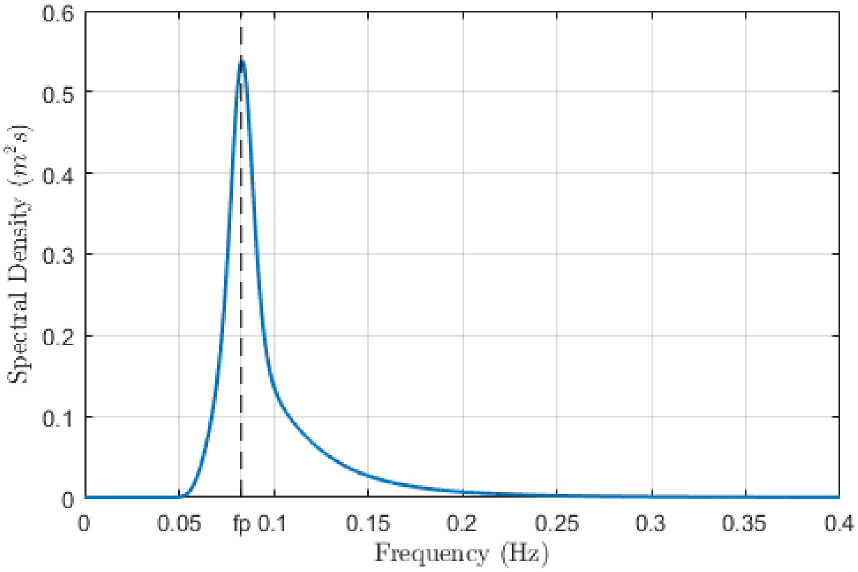

Figure 3.7: JONSWAP wave spectrum input

The synthetic/generated turbulent wind fields, developed in the wind simulation model described previously, were stored in binary format and then used to create the wind loads applied within the coupled SIMO-RIFLEX simulations. These wind loads were based on three fluctuating components, u, v, and w. Below rated (8 m/s), rated (11.4 m/s), and above rated (15 m/s) wind speed scenarios were defined for each simulation, corresponding to groups of the six different seeds, along with mean wind speed factors that varied based on height above ground. The properties of the wind input also included an air density (ρ) = 1.225 kg/m^3, tip loss correction defined through the Prandtl tip loss method, drag force on the turbine tower using the Potential flow tower shadow method, and transient aerodynamics developed through Beddoes-Leishmann dynamic stall method [Putri, 2016].

For the OC3-Hywind spar-buoy FOWT and the OC4-DeepCwind semi-submersible FOWT, two condition sets were considered: 1) *stability sensitivity*, which involved running simulations for neutral (Kaimal spectra), unstable, and very unstable atmospheric conditions and 2) *coherence sensitivity*, which consisted of running the Højstrup spectra with the Modified Coherence Function, Case 1 (varying vertical decay coefficients) and Case 2 (varying horizontal decay coefficients), defined earlier in **Section 3.1.3**. Each scenario described above was simulated for a 1-hour time series, with a 0.02 s time step.

3.3 Damage Equivalent Loads

For a FOWT, it is particularly important to investigate the fatigue damages caused by repetitive loading on all parts of the wind turbine. Based on the material of the component, the stress level, and the number of load cycles, the corresponding deterioration will vary and has the potential to continue until failure. To quantify the level of deterioration, it is common to consider the accumulated damage for each cycle based on Palmgren-Miner linear damage rule (Miner's rule) [Driscol et al., 2016], which assumes that the damage accumulated from each load range can be added linearly [Sathe et al., 2013]. In order to determine the load ranges (σ_i) and the subsequent number of cycles (n_i) for this study, the rain-flow counting method was used in conjunction with Miner's rule. This method breaks down the load time series into bins of load range occurrences. Using this method, the fatigue damage was calculated for each load range using *Equation 3.1* [Lalanne, 2009].

$$D = \sum_i \frac{n_i}{N_i} = \sum_i \frac{n_i}{C} \sigma_i^b \tag{3.1}$$

where n_i is the subsequent number of cycles, N_i is the total number of cycles until failure at the load range, σ_i, $C = N_i \sigma_i^b$, and b is the characteristic parameter of the S-N curve or the Wöhler exponent. For this analysis, b was set as 3 for the tower, tower top, and mooring lines, since they are all made from steel, and 12 for the blades, since they are made from fiberglass [Jonkman et al., 2009].

Using the relationship in *Equation 3.1*, an expression for the equivalent alternating stress, σ_{eq}, can be derived (*Equation 3.2*), corresponding to the same fatigue damage if the loading were applied for the duration of N_{eq} (equivalent number of load cycles), which was assumed as 10^7 for this study, or approximately 20 years of operation [Sathe et al, 2013]. Typically, the fatigue damage is determined experimentally using Wöhler curve, or the stress- number of cycles "S-N curve". However, since it is difficult to define the S-N curve for a particular component, fatigue damage can instead be quantified using the concept of damage equivalent load (DEL), which can be found with *Equation 3.2* [Lalanne, 2009]:

$$\sigma_{eq} = (\sum_i \frac{n_i \sigma_i^b}{N_{eq}})^{1/b} \tag{3.2}$$

where N_{eq} is the equivalent number of load cycles. The lifetime fatigue DEL considers the length of time the wind turbine is designed to operate, at a given wind speed, and can be thought of as a conversion from a load time series of varying amplitude to a sinusoidal load time series of constant amplitude (σ_{eq}) [Sathe et al., 2013].

3.4 Eigen Frequency Analysis & Transfer Functions

Before beginning the simulations, the behavior of the wind turbine can be predicted by comparing the eigen frequencies of the structure, the wave peak frequency, and the wind power spectral density. The response spectral density of the wind turbine can be found through the use of the following equation, given in [Newland, 2005]:

$$S_y(\omega) = |H(\omega)|^2 S_x(\omega) \tag{3.3}$$

where $S_y(\omega)$ is the response spectrum, $H(\omega)$ is the appropriate transfer function, and $S_x(\omega)$ is the corresponding input spectrum. A response amplitude operator (RAO) can be defined as the ratio of the wind turbine response to the wave amplitude and is typically used to evaluate the linear response of a system in the frequency domain [Robertson et al., 2014]. In the work of Robertson et al. [2014], the RAOs for the OC4-DeepCwind FOWT were determined by exciting the system through the use of a white-noise spectrum, which had a frequency range between 0.05 and 0.25 Hz. In that case, the RAO serves as the transfer function, which can be compared to other systems, such as the OC3-Hywind FOWT, in order to analyze how the response may vary under different conditions.

It would be greatly beneficial for future work to include determining a transfer function corresponding to the response of major turbine components of the OC3-Hywind and OC4-DeepCwind FOWTs used within this thesis. This would provide a useful analysis and a general overview as to what is expected from the simulated wind fields and the resulting fatigue loads and platform motions.

4. Results & Discussion

Keeping in mind that the objective of this study is to assess the influence of an unstable turbulent wind spectrum on the loads and motions on a FOWT, the results presented in this section will compare the DELs and motion responses using the Højstrup 1981 Unstable Spectra Model under varying stability and varying coherence, for both the OC3-Hywind FOWT and the OC4-DeepCwind FOWT. In addition to this, the results will be compared to the findings of Putri [2016]; so, in order to make a proper comparison between the two studies, select variables were kept the same, including wind direction, friction velocity, roughness height, wave conditions, and the same characteristics of the OC3-Hywind FOWT.

4.1 OC3-Hywind spar-buoy FOWT

4.1.1 Damage Equivalent Loads

The fatigue loads on the OC3-Hywind FOWT were assessed using the concept of DELs, described earlier in **Section 3.3**. The analysis of the fatigue loads involved two condition sets: stability sensitivity and coherence sensitivity.

4.1.1.1 Stability Sensitivity

The fatigue loads of different components of a wind turbine will theoretically be affected differently by changes in atmospheric stability [Holtslag, 2016]. The DEL on the blade root flap-wise bending moment, the tower top torsion (yaw), and the tower base fore-aft bending moment were considered the most important in analyzing the Højstrup model for stability sensitivity, and are therefore discussed in this section. The DEL on the mooring line tension showed no clear pattern for this condition set, so this component will not be addressed further, but will be displayed in **Appendix A.1.1**. The fatigue loads for other platform modes, such as tower side-to-side moment and blade root edge-wise moment, were not the focus of this analysis. Recall that the atmospheric stability conditions considered for this thesis were classified as very unstable (L = -90 m), unstable (L = -180 m), and neutral ($L = \infty$).

Blade Root Flap-wise Bending Moment

The blade root flap-wise load corresponds to the bending moment acting at the root of the blade [Sathe et al., 2013], and rotates as seen in *Figure 4.1* [Putri, 2016]. The average normalized DELs for the blade root flap-wise moment, normalized with the Kaimal model below rated scenario, are displayed in *Figure 4.2*.

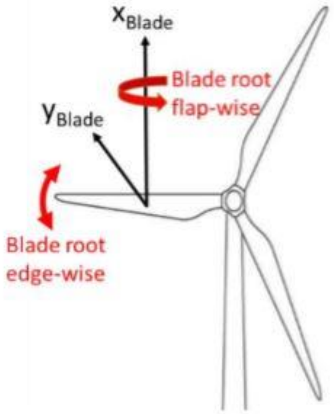

Figure 4.1: Blade root bending moments

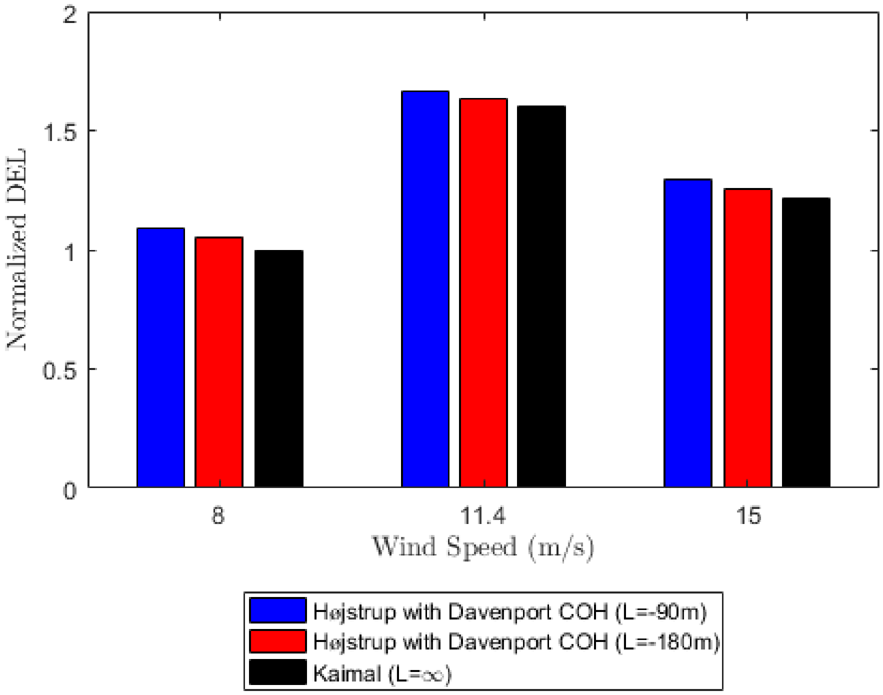

Figure 4.2: Normalized DEL for blade root flap-wise bending, normalized by the Kaimal model at 8 m/s

Theoretically, unstable atmospheric stability conditions correlate to higher turbulence and larger turbulent fluctuations than neutral and stable conditions. As seen in **Section 3.1.6**, the simulations for the Højstrup model with very unstable conditions corresponded to the largest turbulence intensity, which means that the Højstrup model under very unstable conditions should induce larger fatigue loads on the OC3-Hywind FOWT compared to the Højstrup model under unstable conditions, as well as the Kaimal model, which is associated with neutral conditions. This theory is verified in *Figure 4.2*, which shows that the highest DELs corresponded to very unstable conditions. Below rated, rated, and above rated wind speed scenarios were included in the analysis to investigate if the same pattern was observed at the different wind speeds. However, it is important to note that in reality, increasing wind speed implies that there will be less occurrence of unstable conditions [Cheynet et al., 2018]. For each wind speed, very unstable conditions resulted in the largest fatigue damages, followed by unstable and neutral conditions, although the differences appear to be minor. The maximum difference between very unstable conditions and neutral conditions, considering the same wind speed, was approximately 7.5%.

In the research of Putri [2016], it was also found that the blade root flap-wise loads were not significantly influenced by atmospheric stability, with only a 6.5% difference, considering the same wind speed. However, this previous study showed that neutral conditions gave the largest DEL, since the simulations were based on the fitted Mann model for neutral, stable, and unstable conditions. In the study by Sathe et. al [2013], results also showed that atmospheric stability had little influence on the blade root flap-wise bending moment, with only a 3% difference in dynamic loads between non-neutral and neutral wind conditions. Similar to [Putri, 2016], these simulations incorporated the fitted Mann model, and neutral conditions resulted in the largest DEL.

Additionally, it can be seen from the results of this thesis that operating conditions at rated wind speed resulted in the largest fatigue damage, followed by above rated and below rated, which may be related to the pitching mechanism of the wind turbine. *Figure 4.3* illustrates a typical power curve for a wind turbine divided into four operating regions, which correspond to a different control strategy based on cut-in, rated, and cut-out wind speeds.

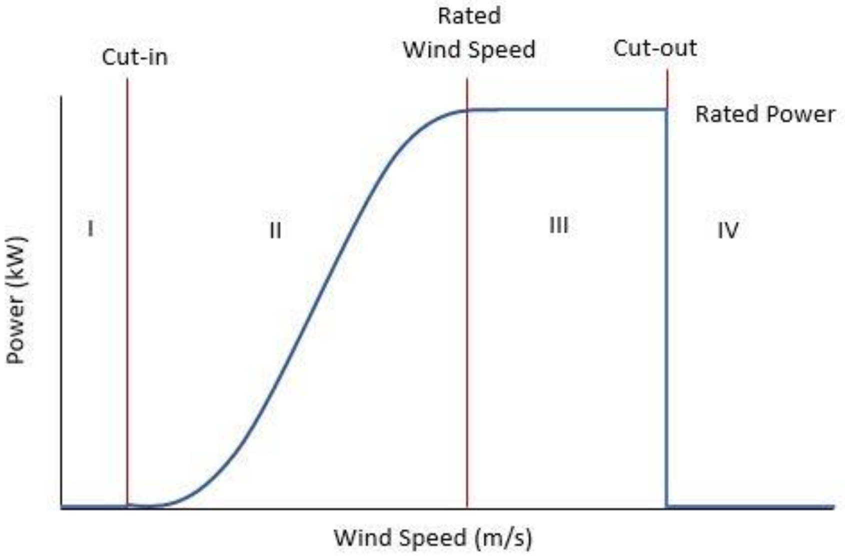

Figure 4.3: Typical power generation curve for a wind turbine, broken down into four operating regions

Below cut-in speed (Region I) and above cut-out speed (Region IV), the turbine is inactive since the wind speeds are either too low or too high for the turbine to function properly. Between cut-in and below rated wind speeds (Region II), the goal is to maximize power extraction [Lackner, 2013]. This is achieved through the use of the generator torque, which adjusts the rotor speed with increasing wind speed and works to maintain a constant tip speed ratio. For above rated operation (Region III), the goal is to maintain a constant rated power output and reduce the loads acting on the wind turbine. In this region, the blades can be pitched to obtain the optimal angle of attack. This means that during times of low wind speeds, the turbine blades are usually pitched into the wind (feathering) to increase lift and consequently, the power output; whereas, during stronger winds, the blades may pitch away from the wind (active stall) to reduce the generated power and regulate the applied loads. The design of the NREL 5 MW wind turbine involves a conventional variable-speed and variable blade-pitch-to-feather control system, which implies that this type of pitching control system for above rated operation is used [Jonkman, et al., 2009]. Since operation in Region III works to generate constant rated power as the wind speed increases, the dynamic response loads acting on the wind turbine are constrained [Lackner, 2013].

It is also beneficial to visualize the blade root flap-wise bending moment using the power spectral density analysis, which highlights the significant excitations of the OC3-Hywind FOWT. *Figures 4.4*, *4.5*, and *4.6* display the spectral density of the blade root flap-wise bending moment for the Højstrup spectra model with varying stability at below rated, rated, and above rated wind speeds, respectively.

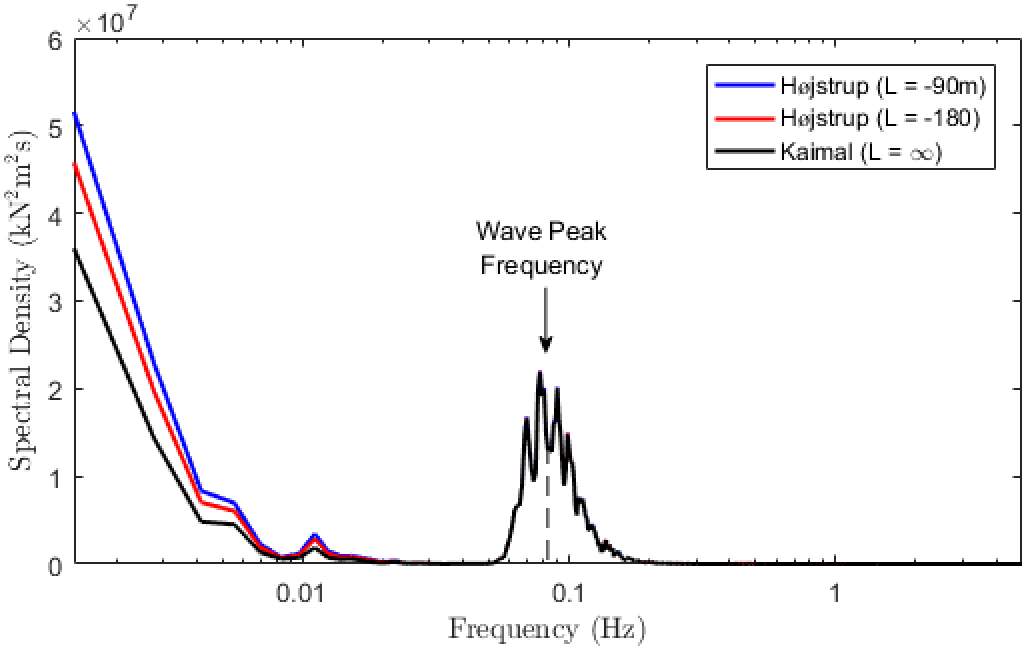

Figure 4.4: Spectral density of blade root flap-wise bending moment at below rated (8 m/s) wind speed

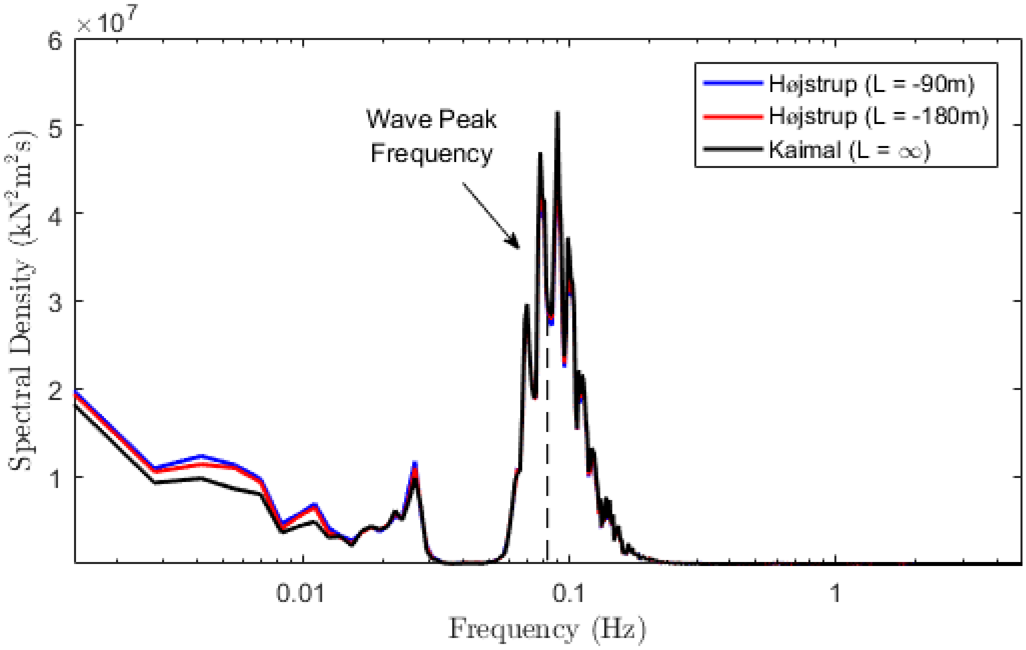

Figure 4.5: Spectral density of blade root flap-wise bending moment at rated (11.4 m/s) wind speed

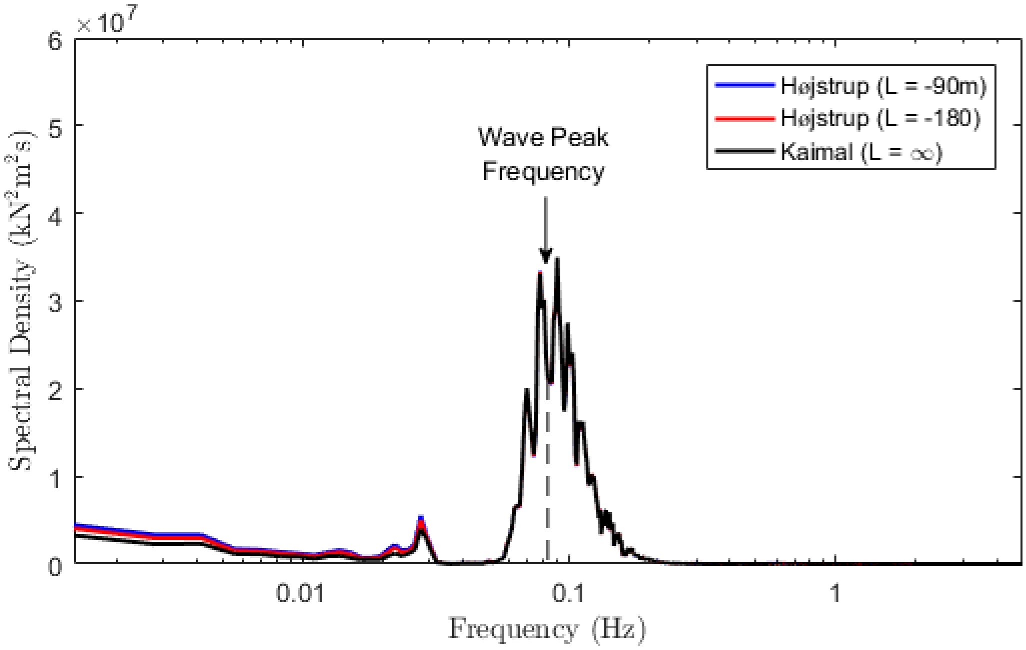

Figure 4.6: Spectral density of blade root flap-wise bending moment at above rated (15 m/s) wind speed

In *Figures 4.4*, *4.5*, and *4.6*, the largest excitation response occurs around the wave peak frequency (0.83 Hz). However, the three stability classes are very similar at this point. Another prominent response is seen at low frequencies, where the Højstrup spectra model for very unstable conditions appears to contain slightly more energy than unstable and neutral conditions, which most likely influenced the results for the DELs. It is also interesting to see that the magnitude of the response at the wave peak frequency is highest at rated wind speed, followed by above rated and below rated wind speeds, which matches the pattern observed in the DEL results.

Since the spectral density is displayed on a semi log x-scale, the 3P response frequency, which is defined for a 3-bladed wind turbine as the blade passing frequency, is not highlighted. The 1P, 2P, and 3P rotation frequencies were calculated using the rotor rotational speeds given in the standards for the NREL 5 MW wind turbine and are displayed in *Table 4.1.*

Table 4.1: Frequencies of Rotating Blades, associated with wind speed, for the NREL 5 MW Wind Turbine

Operating Region	Wind Speed (m/s)	Rotor Rotational Frequency (rpm)	1P Frequency (Hz)	2P Frequency (Hz)	3P Frequency (Hz)
Below Rated	8	9.995	0.16	0.33	0.48
Rated	11.4	12.1	0.20	0.40	0.60
Above Rated	15	12.1	0.20	0.40	0.60

It is important to mention that the Højstrup spectra model with very unstable conditions was noticeably larger than unstable and neutral conditions around the 3P frequency when displayed on a semi log y-scale. However, a semi log x-scale was chosen because the magnitude of the excitation response at the 3P frequency was much lower compared to the excitation response at lower frequencies, and the semi log x-scale highlighted this difference.

Tower Top Torsion

The average normalized DELs for tower top torsion, normalized with the Kaimal model below rated scenario, are displayed in *Figure 4.7*.

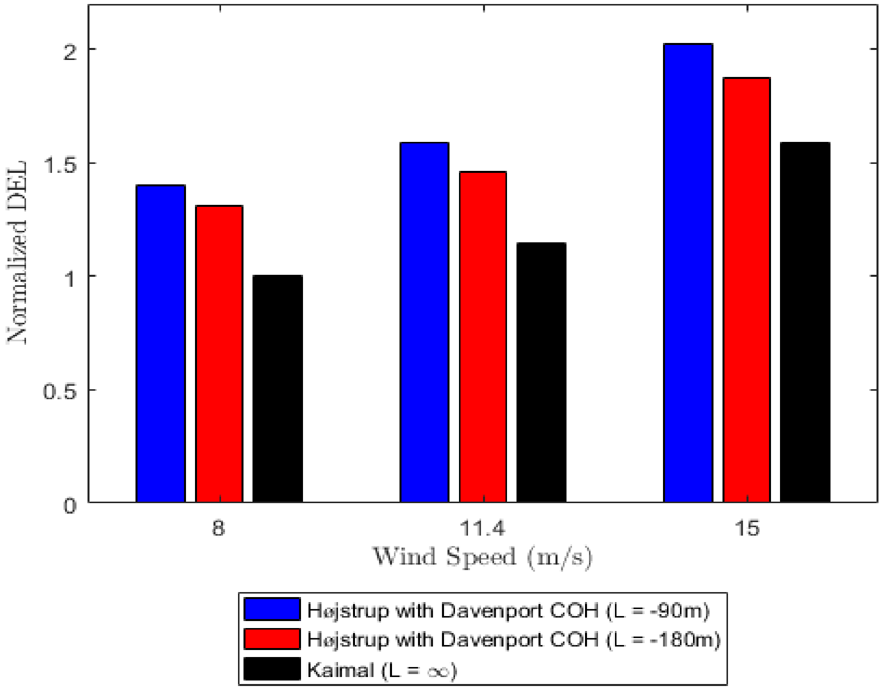

Figure 4.7: Normalized DEL for tower top torsion, normalized by the Kaimal model at 8 m/s

A similar trend was found for tower top torsion, with very unstable conditions giving the largest DELs. However, in this case, atmospheric stability, and its relationship to turbulence intensity, seems to have more of an influence on the resulting DELs compared to its influence on the DELs for the blade root flap-wise bending moment. For tower top torsion, the maximum difference between very unstable conditions and neutral conditions, considering the same wind speed, was approximately 47%.

In the research of Putri [2016], tower top torsion also displayed significant differences between the different load cases, however, with neutral atmospheric conditions resulting in the largest DELs, followed by unstable and stable conditions. Within the study by Putri [2016], wind turbulence was highest under neutral conditions, since the turbulent energy for neutral conditions simulated in that study were related to an increase in mechanically generated/shear produced turbulence. In contrast, this study found that the highest turbulence corresponded to (very) unstable conditions, which was expected due to the inclusion of vertical mixing associated with buoyancy generated turbulence, discussed earlier in **Section 2.2**. Considering these findings, both studies showed that turbulence intensity played an important role in the resulting fatigue loads on the tower top torsion. In the research of Saranyasoontorn and Manuel [2008], it was concluded that turbulence had a negligible effect on the blades and tower base, but had a significant effect on the yaw moments.

The spectral density of tower top torsion for the Højstrup spectra model with varying stability at below rated, rated, and above rated wind speeds is displayed in *Figures 4.8*, *4.9*, and *4.10*.

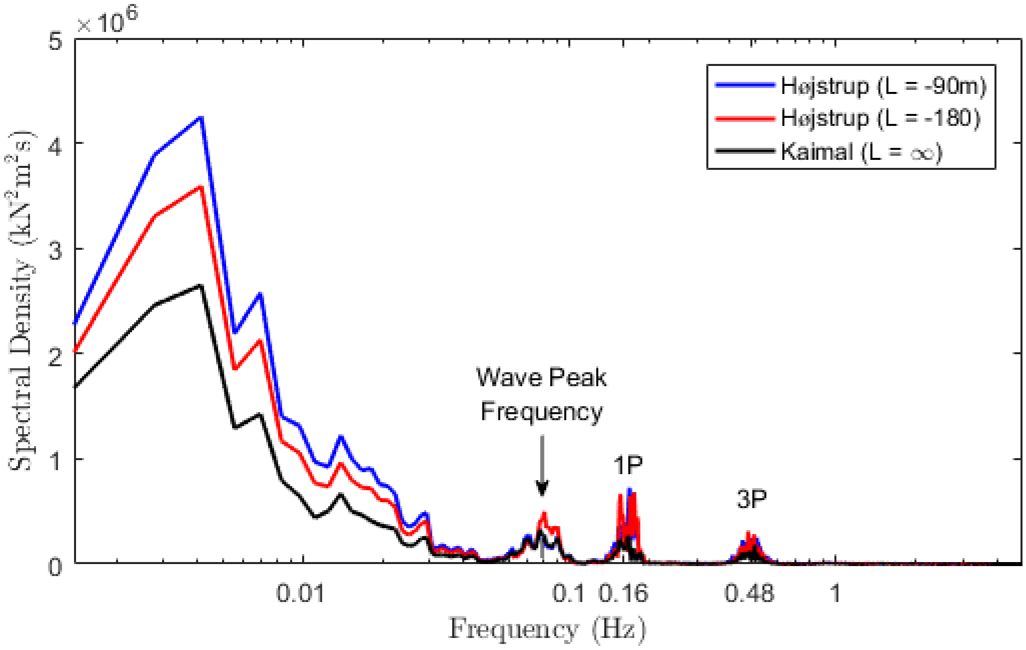

Figure 4.8: Spectral density of tower top torsion at below rated (8 m/s) wind speed

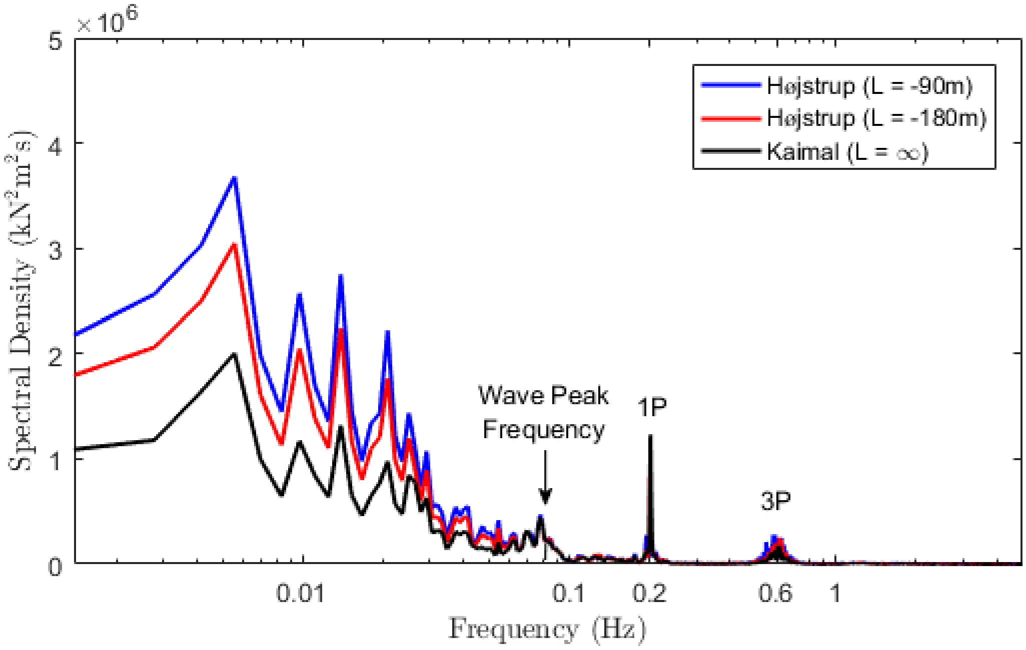

Figure 4.9: Spectral density of tower top torsion at rated (11.4 m/s) wind speed

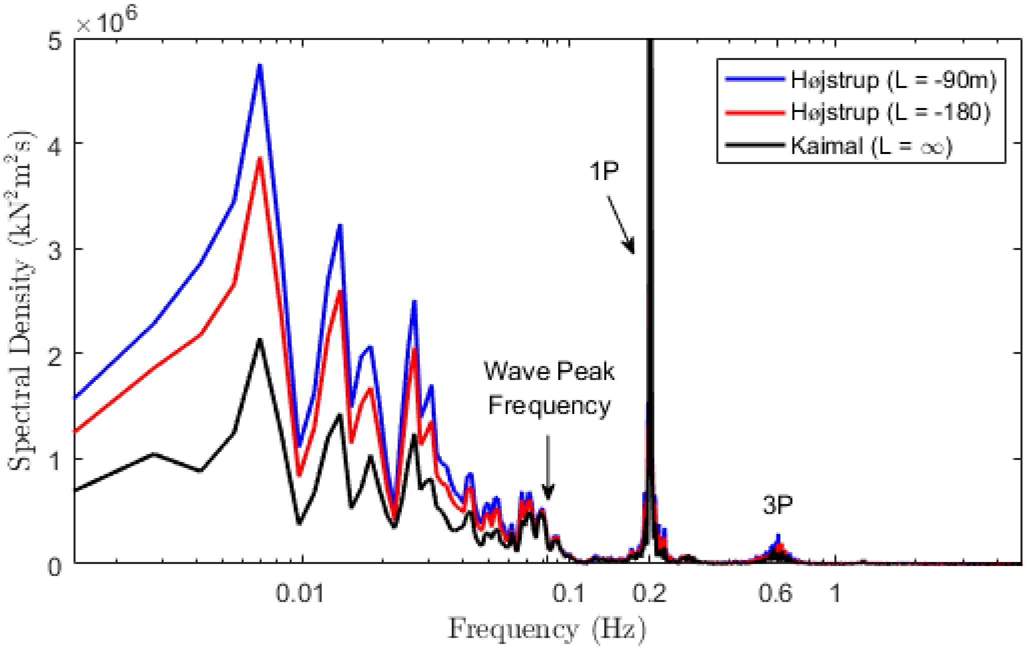

Figure 4.10: Spectral density of tower top torsion at above rated (15 m/s) wind speed

The results show that the tower top torsion for the OC3-Hywind FOWT was excited by the 3P frequency, the 1P frequency, and waves with a peak frequency of 0.83 Hz. The excitation at the wave peak frequency appears more pronounced as the wind speed decreases, whereas, the 1P excitation becomes sharper and larger as the wind speed increases. By comparing the spectral density of tower top torsion for the different wind speeds, one can see that the 1P frequency occurs at about 0.16 Hz for below rated and then shifts to about 0.2 Hz for rated and above rated wind speeds, just as the 3P frequency shifts from 0.48 Hz to 0.6 Hz, as was given in *Table 4.1*.

The most significant response and variation in atmospheric stability seems to have occurred at low frequencies where the very unstable Højstrup model is larger than both unstable and neutral conditions, a pattern which was observed at all wind speeds. Small differences in atmospheric stability were also noticeable around the 3P frequency, which for rated and above rated wind speeds, is very close to the drive train natural frequency (0.63 Hz). However, just as was stated in the blade root flap-wise analysis, the 3P excitation response had a much smaller magnitude compared to the response at low frequencies, and therefore, probably had less contribution to the fatigue damage.

Tower Base Fore-aft Bending Moment

The DELs for the tower base fore-aft bending moment did not show significant differences in the results when varying atmospheric stability. Therefore, the average DELs for the tower base fore-aft bending moment are displayed in **Appendix A.1.1.** The maximum difference between very unstable conditions and neutral conditions, considering the same wind speed, was approximately 4.7%. Results of the study by Putri [2016] also showed that the DELs for the tower base fore-aft bending were similar for the different stabilities, but with the highest DELs corresponding to neutral conditions, followed by unstable and stable conditions.

4.1.1.2 Vertical Coherence Sensitivity (Case 1)

Coherence sensitivity was included in this study as a way to analyze the influence of vertical and lateral coherence on a FOWT. As a reminder, the Højstrup model with the Modified Coherence Function was used for analyzing coherence sensitivity, and the conditions of Case 1 involved keeping the horizontal decay coefficients constant while varying the vertical decay coefficients. Theoretically, in doing this, the effect of vertical coherence would be isolated. The first set of decay coefficients within Case 1, described in more detail in **Section 3.1.3**, will be referred to as Modified COH Case 1a, while the second set will be referred to as Modified COH Case 1b. These two sets of decay coefficients are listed in **Table 3.5**. To identify which set of decay coefficients simulated a more coherent wind field, the along wind simulated coherence (γ_{uu}) using the Modified Coherence Function, for Case 1a and 1b, is displayed in *Figure 4.11* for a 30 m and 120 m vertical separation (Δz) at rated wind speed. The simulated coherence was found by taking the simulated velocities of each wind field and looking at the correlation between two chosen points within the grid, for example two points vertically separated by 30 m. **Appendix C.1.1** provides further details regarding the algorithm used to determine the simulated coherence.

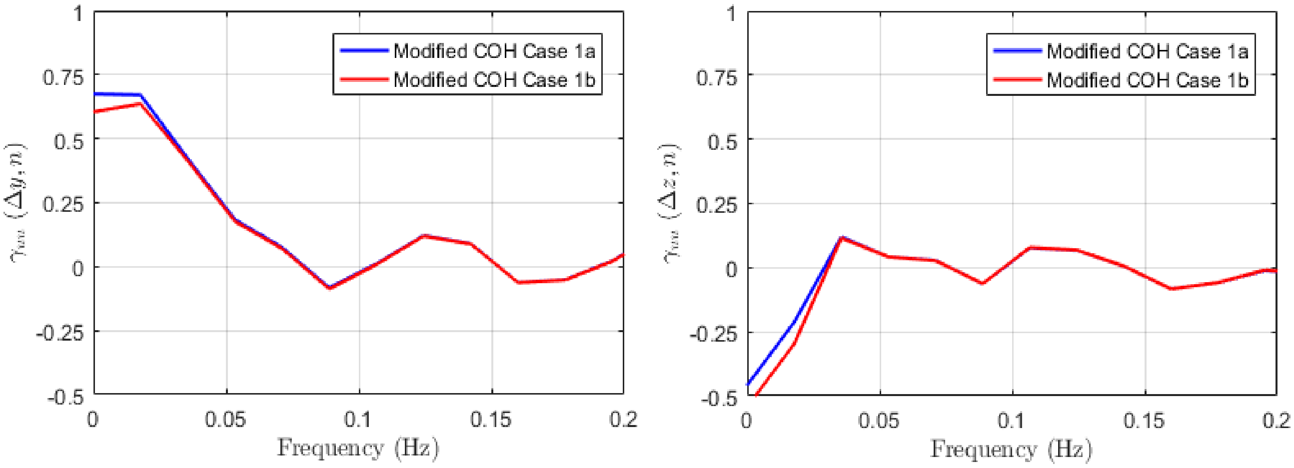

Figure 4.11: Simulated coherence for 30 m (left) and 120 m (right) vertical separation using the Modified Coherence Model for Case 1 at rated wind Speed

As one can see in *Figure 4.11*, Case 1a is slightly more coherent than Case 1b. The decay coefficients used within Case 1a were determined using very unstable conditions, whereas those defined in Case 1b were determined using unstable conditions. Since very unstable conditions correspond to more mixing than less unstable conditions, the wind field is more uniform, and therefore, more coherent. Had stable conditions been included in the analysis, the differences between the decay coefficients would have been larger.

The DELs on the blade root flap-wise bending moment, tower top torsion, and tower base fore-aft moment were considered the most important in analyzing the Højstrup model for vertical coherence sensitivity, and will be discussed in this section. The DELs for the mooring line tension showed no clear pattern, so these results will be presented in **Appendix A.1.1.** For each simulation, the logarithmic wind speed profile was used.

Blade Root Flap-wise Bending Moment

The average normalized DELs for the blade root flap-wise bending moment with varying vertical coherence (Case 1), normalized with the Kaimal model below rated scenario, are displayed in *Figure 4.12*.

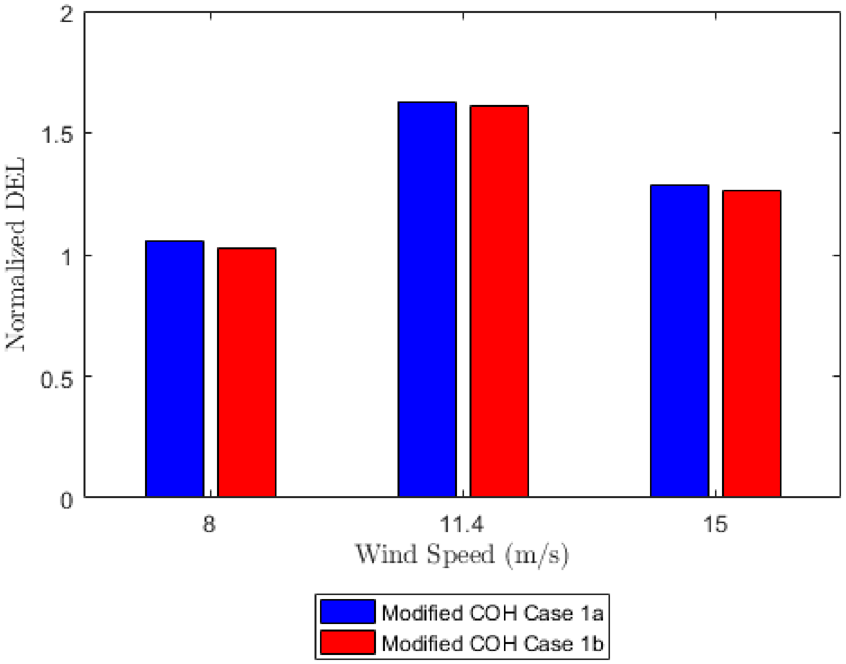

Figure 4.12: Normalized DEL for blade root flap-wise bending, normalized by the Kaimal model at 8 m/s, for the Højstrup model with varying **vertical** coherence

Although the differences in the DELs for the blade root flap-wise moment when varying vertical coherence appear minor, it is interesting to see that simulations using the decay coefficients defined in

Case 1a resulted in the highest fatigue damage compared to simulations using Case 1b. The maximum difference between the Højstrup model with modified coherence Case 1a and with modified coherence Case 1b, considering the same wind speed, was approximately 16.25%. As was previously mentioned, the Højstrup model using the Modified Coherence Function, Case 1a, generated a more coherent wind field than Case 1b. In the work of Eliassen et al. [2015], they concluded that an increase in coherence typically resulted in an increase in fatigue loads [Eliassen and Obhrai, 2016], which was also seen here. This coincides with the definition of turbulent wind loading, in that increased coherence implies an increase in loading.

In the research of Putri [2016], a connection is made between the excitation of the blade root flap-wise moment and the platform pitch motion. Additionally, at wind speeds below rated, Putri [2016] found that higher vertical coherence resulted in higher platform pitch motion. Considering the results found in this study, it seems likely that the blade root flap-wise moment, which is linked to the pitching mechanism of the wind turbine, was at least slightly influenced by changes in vertical coherence.

Tower Top Torsion

The average normalized DELs for tower top torsion with vertical varying coherence, normalized with the Kaimal model below rated scenario, are displayed in *Figure 4.13*.

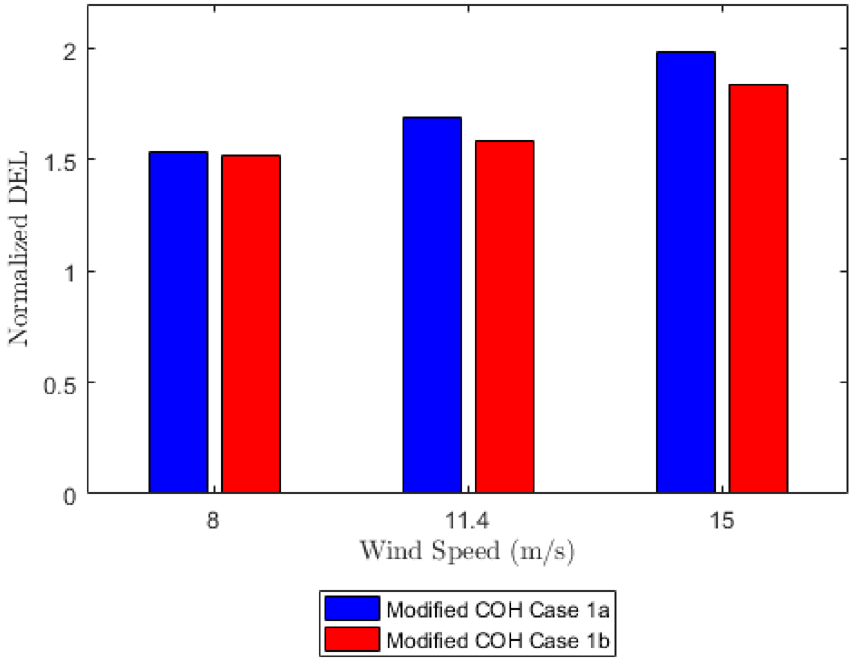

Figure 4.13: Normalized DEL for tower top torsion, normalized by the Kaimal model at 8 m/s, for the Højstrup spectra model with varying **vertical** coherence

Similar to what was found for the DELs for the blade root flap-wise moment, the DELs for the tower top torsion were largest when running simulations with the case associated with a more coherent wind field, Case 1a. The maximum difference between the Højstrup model with modified coherence Case 1a and Case 1b, considering the same wind speed, was approximately 9.68%.

Tower Base Fore-aft Moment

The results for the tower base fore-aft moment were relatively insignificant when varying vertical coherence, with a maximum difference of 4.7% between Case 1a and Case 1b. The DELs for the tower base fore-aft moment are displayed in **Appendix A.1.1**.

4.1.1.3 Lateral Coherence Sensitivity (Case 2)

The influence of lateral coherence was investigated using the Modified Coherence Function with varying horizontal decay coefficients. For Case 2, the vertical decay coefficients were held constant, while the horizontal decay coefficients were varied, therefore, isolating the effect of lateral coherence. The first set of decay coefficients within Case 2, described earlier in **Section 3.1.3**, will be referred to as Modified COH Case 2a and the second set will be referred to as Modified COH Case 2b. These two sets of decay coefficients are listed in **Table 3.6**. The along wind simulated coherence (γ_{uu}) using the Modified Coherence function, for Case 2a and 2b, is displayed in *Figure 4.14* for a 30 m and 120 m lateral separation (Δy) at rated wind speed. By looking at the figure, Case 2b appears to be slightly more coherent than Case 2a for both separation distances.

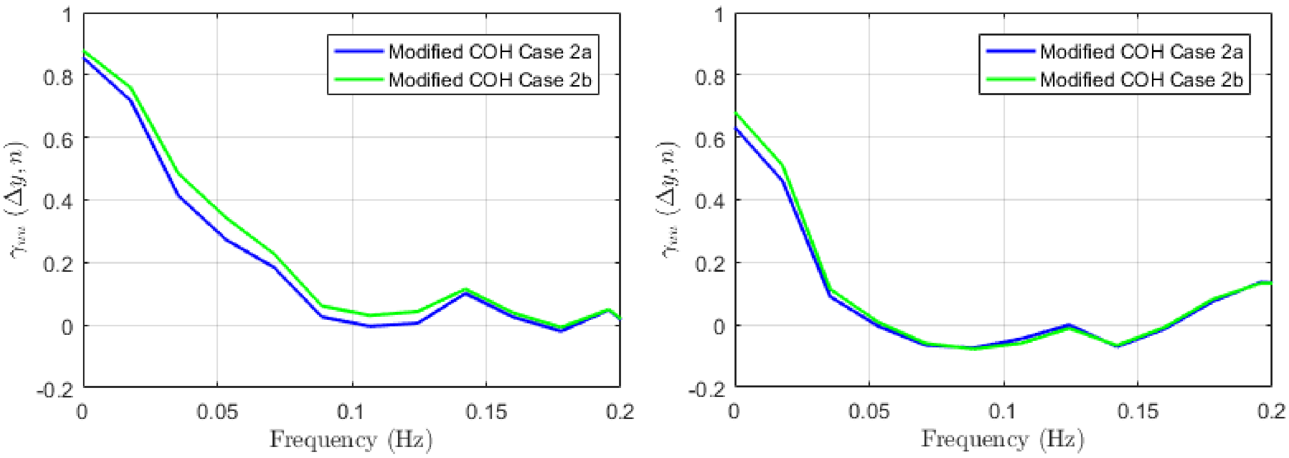

Figure 4.14: Simulated coherence for 30 m (left) and 120 m (right) lateral separation using the Modified Coherence Model for Case 2 at rated wind speed

In addition to determining the DELs on the blade root flap-wise bending moment, tower top torsion, and tower base fore-aft moment, the mooring line tensions were also included in the analysis of the

Højstrup model for lateral coherence sensitivity, as theoretically, they may be influenced by the platform movement in yaw.

Blade Root Flap-wise Bending Moment

The average normalized DELs for the blade root flap-wise moment with varying lateral coherence, normalized with the Kaimal model below rated scenario, are displayed in *Figure 4.15*.

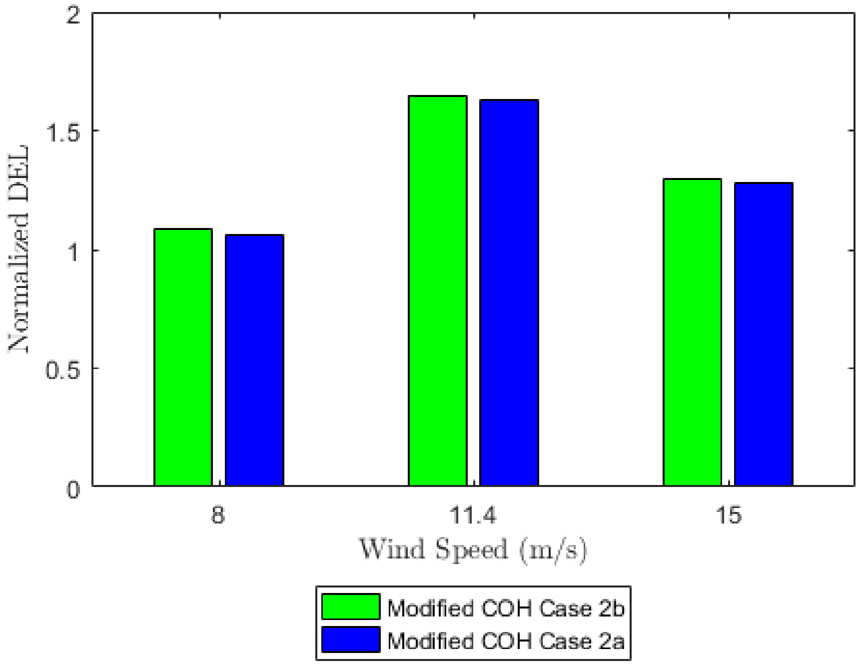

Figure 4.15: Normalized DEL for blade root flap-wise moment, normalized by the Kaimal model at 8 m/s, for the Højstrup spectra model with varying **lateral** coherence

In this case, the largest DELs for the blade root flap-wise moment were found for the Højstrup model with the Modified Coherence Function, Case 2b. The maximum difference between Case 2b and Case 2a was approximately 11.13%. As was pointed out earlier, Case 2b corresponded to a higher lateral coherence. Therefore, just as was seen when varying vertical coherence, the blade root flap-wise moment was most affected by a more coherent wind field. However, based on the maximum percent difference, 16.25% when varying vertical coherence and 11.13% when varying lateral coherence, the blade root flap-wise moment seems to be more influenced by a variation in vertical coherence.

Tower Top Torsion

The average normalized DELs for tower top torsion with varying lateral coherence, normalized with the Kaimal model below rated scenario, are displayed in *Figure* 4.16.

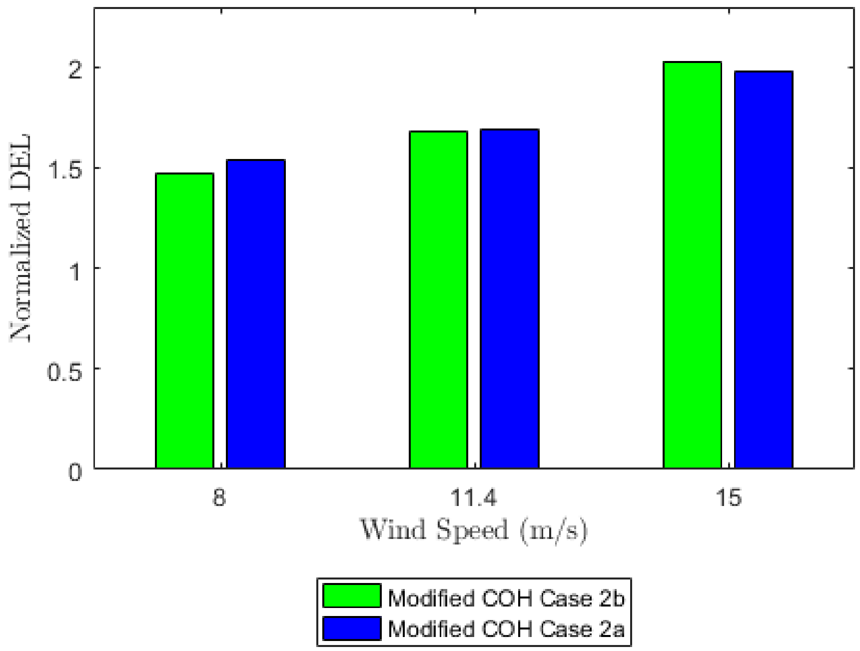

Figure 4.16: Normalized DEL for tower top torsion, normalized by the Kaimal model at 8 m/s, for the Højstrup spectra model with varying **lateral** coherence

In contrast to the results found for the blade root flap-wise bending moment, the largest DEL for the tower top torsion occurred for the Højstrup model with the Modified Coherence Function, Case 2a, for below rated and rated wind speeds. The maximum difference between Case 2a and Case 2b was approximately 13.4%. Since Case 2b corresponded to higher lateral coherence, it is interesting that the less coherent wind field for below and rated wind speed scenarios resulted in the most fatigue damage for the tower top torsion. In order to understand this result, it is helpful to visualize the coherence for larger separation distances of the order of the rotor diameter, which are more likely to influence the tower top movement. Theoretically, if the wind field is less coherent at large separation distances, the wind will apply asymmetric loading on the turbine, causing the tower top to move in yaw. As was depicted earlier in the right plot of *Figure 4.14*, for a 120 m lateral separation, Case 2a was less coherent. Therefore, from the results found in this study, it seems as though lower lateral coherence resulted in higher tower top torsion, except at above rated wind speeds.

Tower Base Fore-aft Moment

The tower base fore-aft moment was seemingly unaffected by changes in lateral coherence, with a maximum difference of approximately 5.7%.

Mooring Line Tensions

The average normalized DELs for mooring line tension with varying lateral coherence, normalized with the Kaimal model below rated scenario, is displayed in *Figures 4.17*, *4.18*, and 4.19 for mooring lines 1, 2, and 3, respectively.

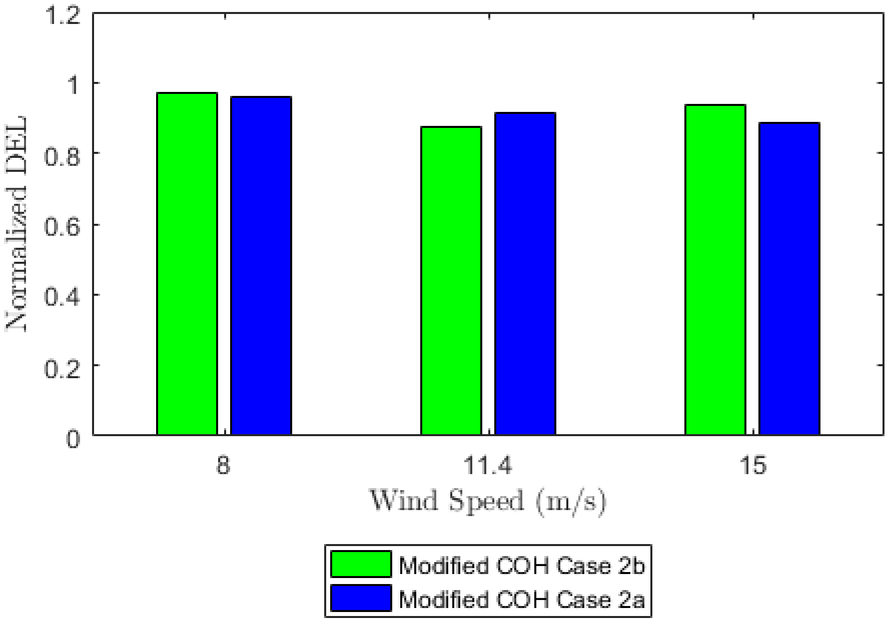

Figure 4.17: Normalized DEL for mooring line 1 tension, normalized by the Kaimal model at 8 m/s, for the Højstrup spectra model with varying **lateral** coherence

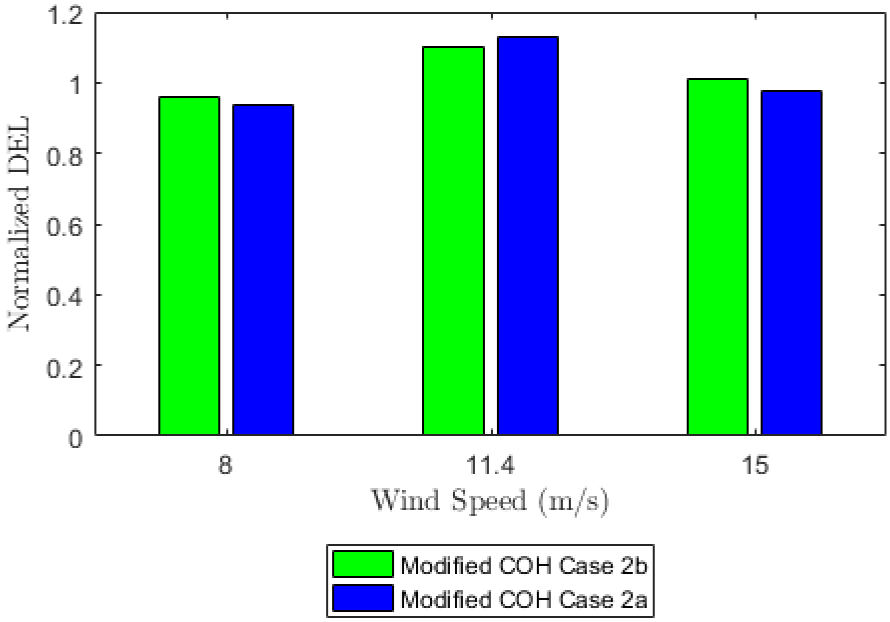

Figure 4.18: Normalized DEL for mooring line 2 tension, normalized by the Kaimal model at 8 m/s, for the Højstrup spectra model with varying **lateral** coherence

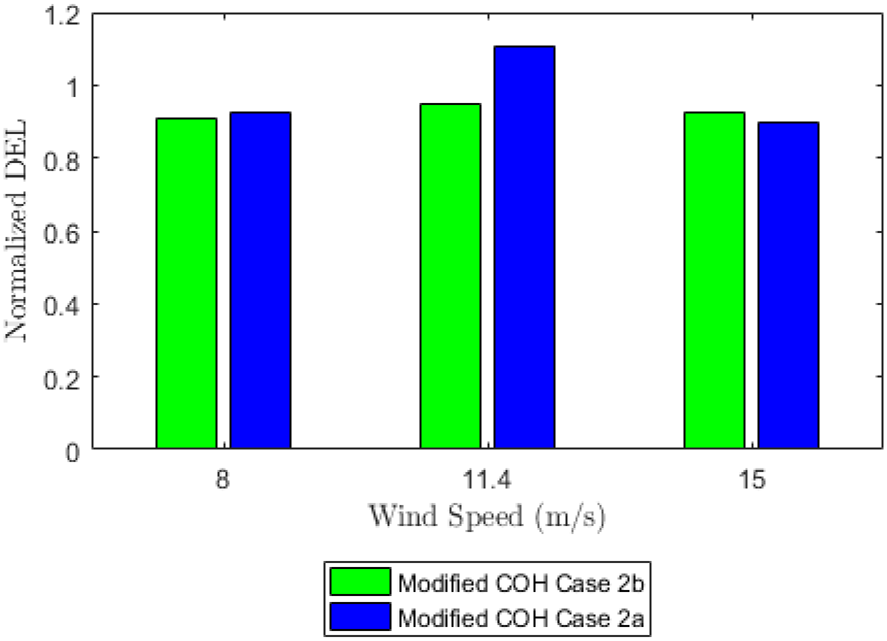

Figure 4.19: Normalized DEL for mooring line 3 tension, normalized by the Kaimal model at 8 m/s, for the Højstrup spectra model with varying **lateral** coherence

The results for the mooring line tensions show that for each mooring line, simulations using the Højstrup model with the Modified Coherence Function Case 2a, found to be the less coherent wind field compared to Case 2b, gave the largest DELs for rated wind speed. The maximum difference between Case 2a and Case 2b was observed for mooring line 3 at rated wind speed with a value of 39.3%. The DELs for mooring line 3 followed the same trend as the DELs for the tower top torsion. As was discussed when analyzing the tower top torsion, asymmetric loading on the wind turbine, laterally, may cause the platform to move in yaw. This yaw movement could then influence the load response of the mooring lines. The research of Bachynski and Eliassen [2019] found that the mooring line fatigue damage was related to the platform motions, and specifically the low frequency yaw response of a spar-buoy type FOWT.

4.1.2 Platform Motions

In order to fully analyze the response of a FOWT, it is important to evaluate the motions in six degrees of freedom that the OC3-Hywind FOWT will experience due to both wind and wave loadings. *Figure 4.20* [Tran and Kim, 2015] shows the six degrees of freedom for a spar-buoy type FOWT, along with the turbine and hub coordinate system and direction of mean wind speed.

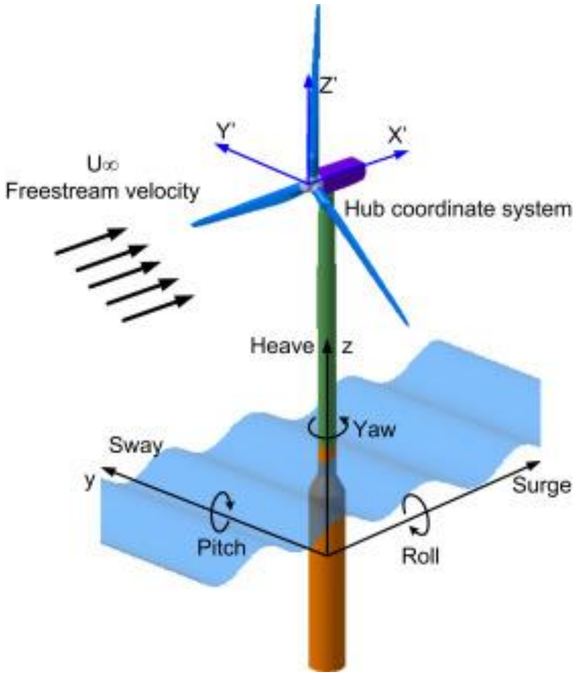

Figure 4.20: The degrees of freedom for a spar-buoy floating offshore wind turbine

Refer to **Chapter 3**, *Table 3.3* for the natural frequencies of the platform motions for the OC3-Hywind FOWT.

4.1.2.1 Stability Sensitivity

The results for the platform sway and heave displacements, along with pitch and yaw rotation under varying stability are the main focus of the results presented in this section, as they exhibited notable differences in atmospheric stability compared to the other platform motions. The remaining platform motions are presented in **Appendix B.1.1**. The platform motions of the OC3-Hywind FOWT were analyzed using power spectral densities, as displayed in *Figures 4.21 – 4.24*. These figures are displayed using a semi log x-scale, as it was decided that the platform motions were best visualized in this format.

Sway

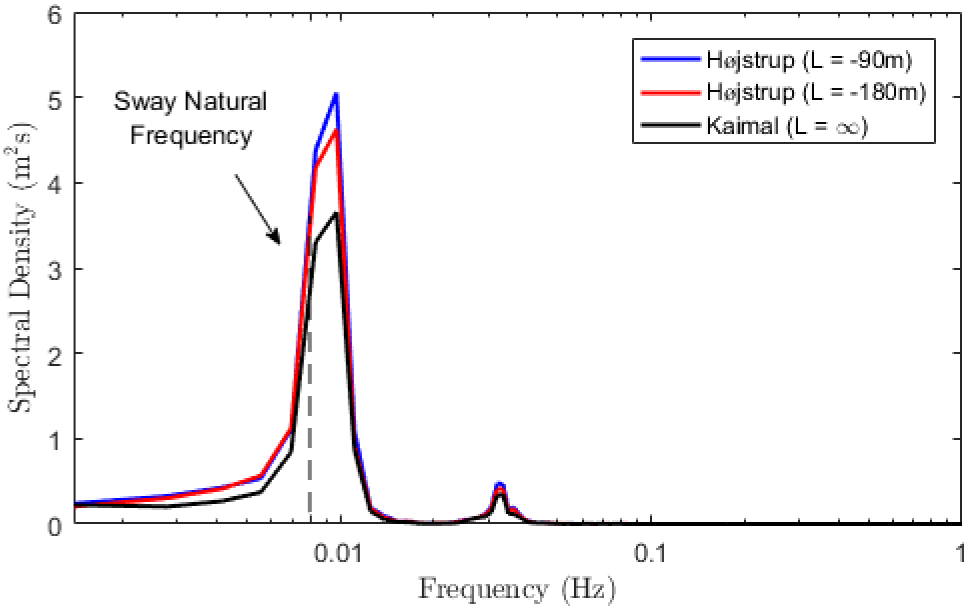

Figure 4.21: Spectral density of sway displacement for varying stability at rated wind speed (11.4 m/s)

The resulting platform displacement in sway was excited by the OC3-Hywind sway natural frequency (0.008 Hz), as well as a multiple of this natural frequency (0.032 Hz). At these frequencies, it is apparent that the spectral energy for sway is higher for very unstable conditions than for unstable and neutral conditions. In the work of [Bachynski and Eliassen, 2019], a response was also seen at the sway natural frequency.

Heave

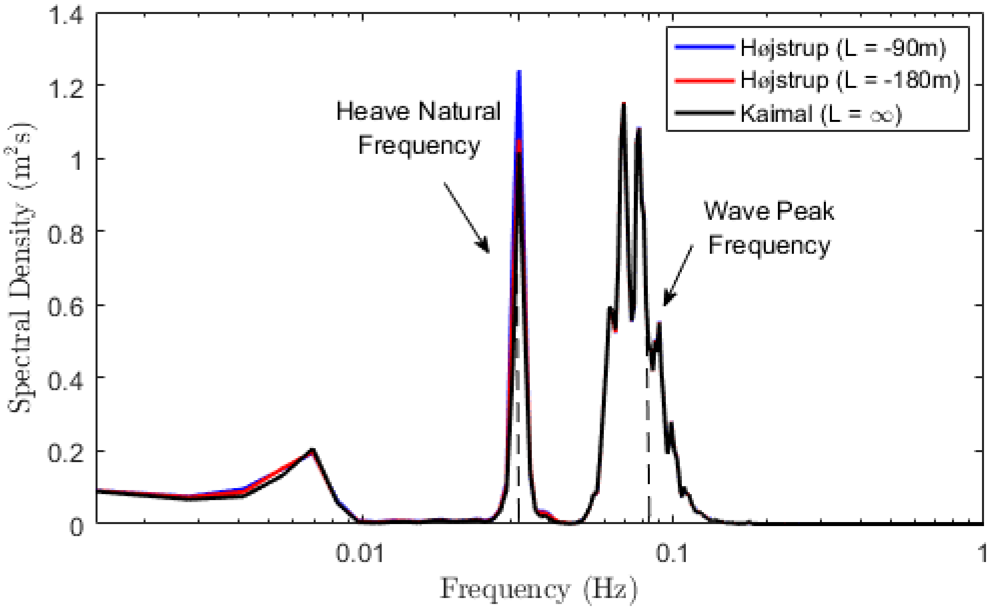

Figure 4.22: Spectral density of heave displacement for varying stability at rated wind speed (11.4 m/s)

Unlike the resulting sway displacement, the platform heave displacement exhibited a notable response at the wave peak frequency (0.083 Hz) in addition to a response at the OC3-Hywind heave natural frequency (0.032 Hz). Bachynski and Eliassen [2019] also observed that the heave motion for a spar-buoy type FOWT involved non-negligible excitation at low frequencies. However, at the wave peak frequency, the three models are almost identical, whereas, at the heave natural frequency, the very unstable Højstrup model contains the highest spectral energy.

Pitch

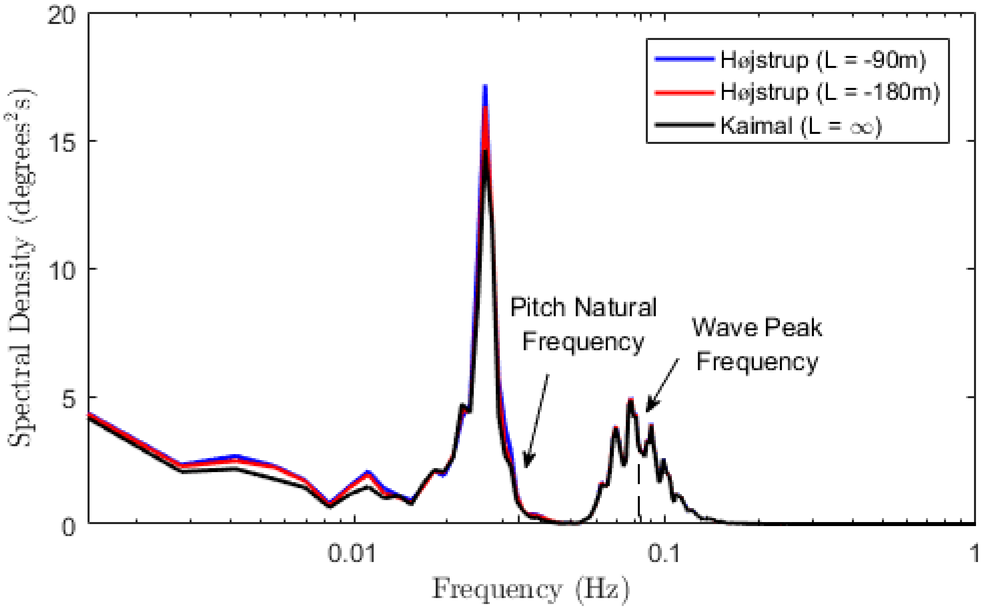

Figure 4.23: Spectral density of pitch rotation for varying stability at rated wind speed (11.4 m/s)

Under the conditions defined within this study, the OC3-Hywind platform seems to experience higher changes in pitch rotation compared to sway and heave displacement and yaw rotation. Note that a larger range of values is used on the y-axis to display the spectral density of pitch rotation. The platform pitch rotation appears to have been excited by the wave peak frequency as well as frequencies just before the pitch natural frequency (0.034 Hz). This result may indicate that the pitch natural frequency for the OC3-Hywind platform used for this analysis was actually slightly lower than what was given by [Jonkman, 2010]. Also, the resulting platform pitch motion of the OC3-Hywind FOWT may be connected to the negative damping associated with the blade pitch control system, which stems from the reduction in rotor thrust as the wind speed increases above rated [Lackner, 2012]. In the study by Jonkman [2010], it is also mentioned that negative damping could lead to large resonant motions of a FOWT. However, if the duration of the negative damping becomes too large, the turbine may experience catastrophic failure.

Yaw

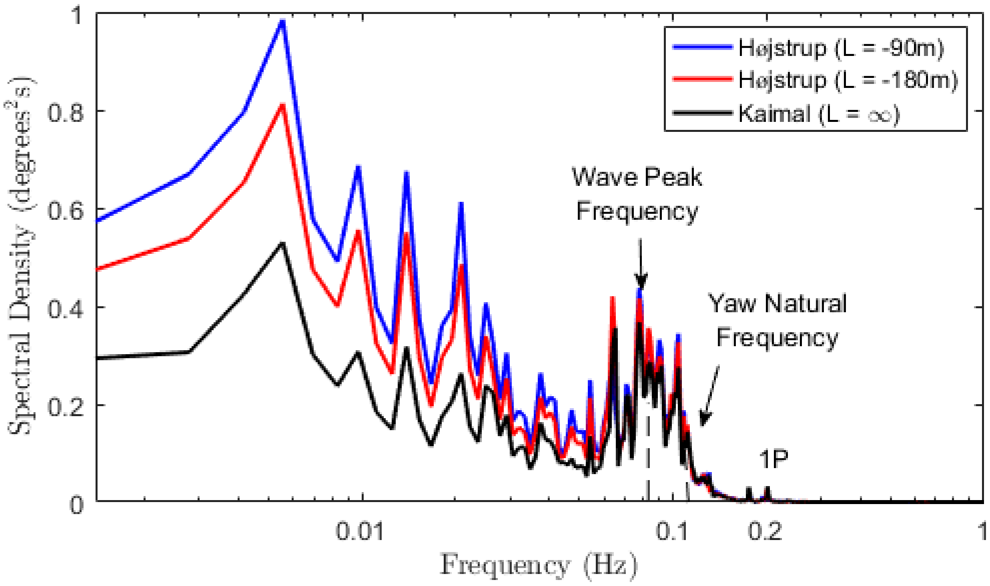

Figure 4.24: Spectral density of yaw rotation for varying stability at rated wind speed (11.4 m/s)

The differences between the turbulence models were noticeable in the results for the yaw rotation. Excitation responses can be seen at low frequencies, around the wave peak frequency, at the OC3-Hywind yaw natural frequency (~0.11 Hz), and a very small response at the 1P natural frequency (0.2 Hz). Since the spar-buoy foundation is characterized by high mooring stiffness and a low moment of inertia in yaw about the center of mass, it makes sense to see a "quasi-static" yaw response at low frequencies [Bachynski and Eliassen, 2019]. In the study by Bachynski and Eliassen [2019], it was also found that the spar-buoy type FOWT responded at the 1P natural frequency, which was believed to be related to turbulence sampling. Additionally, results seen in the study by Putri [2016] revealed that unstable conditions gave the largest yaw rotation for rated wind speed, followed by neutral and stable conditions. Although stable conditions were not analyzed for this thesis, it is clear that very unstable conditions resulted in the largest excitation response in yaw, followed by unstable and neutral conditions.

4.1.2.2 Coherence Sensitivity

Although there were minimal differences in the platform motions for the Højstrup model under varying coherence, the platform motions with the most notable variation were pitch and yaw. Theoretically, the platform pitch motion of a FOWT can be analyzed using vertical coherence. Typically, higher vertical coherence results in higher platform pitch motion, which was seen here and also in the results of Putri [2016]. However, although platform pitch was slightly larger when using simulations with a more coherent wind field, the difference between the mean value of the pitch motion with the Modified

Coherence Function Case 1a (more coherent) and Case 1b (less coherent) was just about 2%, which is extremely small. *Figure 4.25* shows the power spectral density of the platform pitch motion for the Højstrup model under varying coherence. As one can see in the figure, the two sub-condition sets within Case 1 are very similar, with only a small difference between the two at very low frequencies.

Pitch

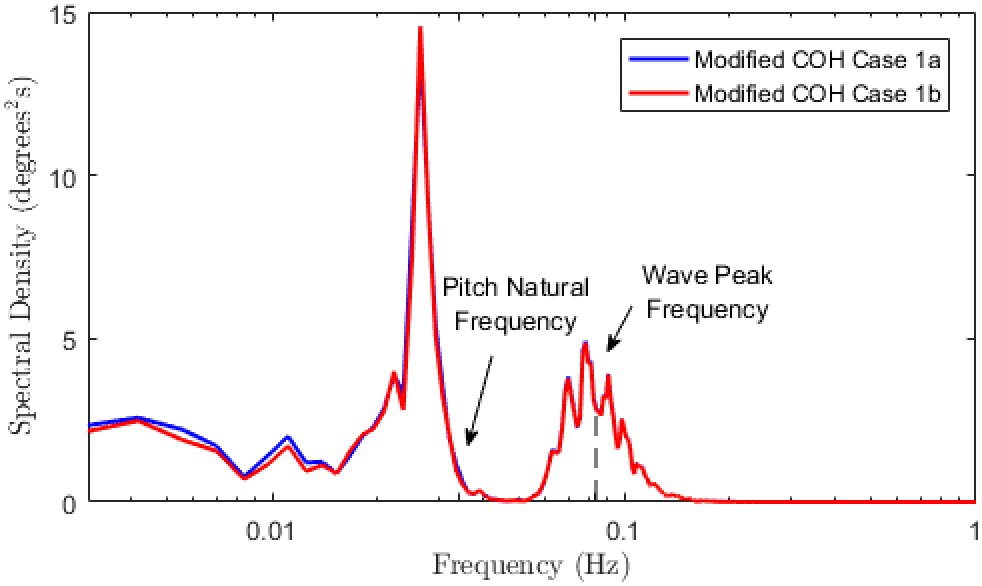

Figure 4.25: Spectral density of pitch rotation for varying **vertical** coherence at rated wind speed (11.4 m/s)

Additionally, the OC3-Hywind FOWT yaw response was analyzed using lateral coherence. As pointed out earlier when analyzing tower top torsion, a larger coherence for large lateral separations, such as the rotor diameter (120m), could reduce the platform's yaw response. In the study by Putri [2016], results showed that for neutral conditions, higher lateral coherence for separation distances above 40 m resulted in lower platform yaw motions. *Figure 4.26* shows the power spectral density of the platform yaw motion for the Højstrup model under varying coherence. Recall that the Højstrup model with the Modified Coherence Function Case 2b is more coherent than Case 2a. As *Figure 4.26* shows, the two sub-condition sets within Case 2 are very similar, although Case 2a appears somewhat larger than Case 2b at lower frequencies; hence, the less coherent wind field resulted in a larger yaw response at very low frequencies.

Yaw

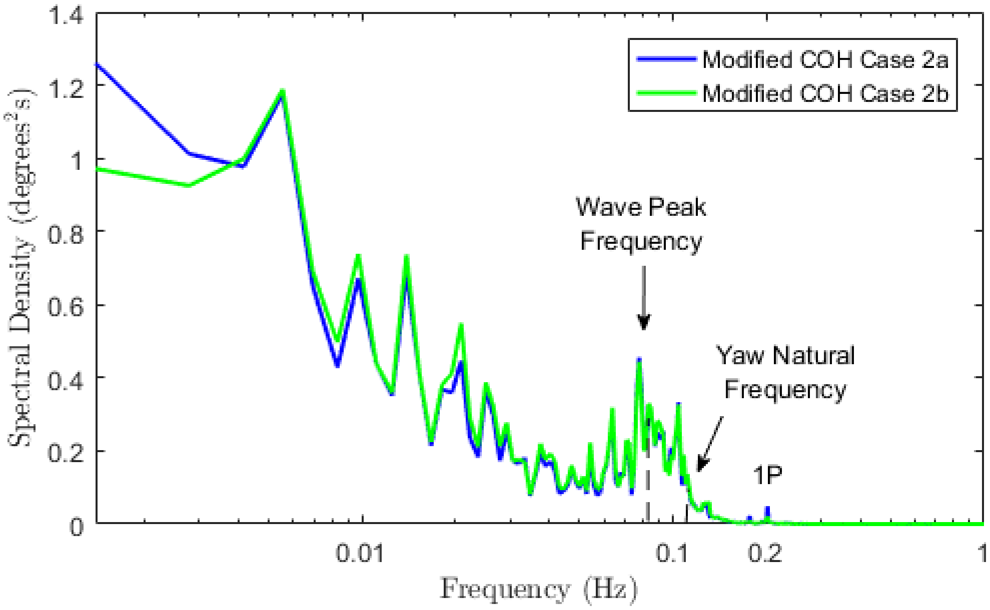

Figure 4.26: Spectral density of yaw rotation for varying **lateral** coherence at rated wind speed (11.4 m/s)

4.2 OC4-DeepCwind Semisubmersible FOWT

4.2.1 Damage Equivalent Loads

The DELs for the OC4-DeepCwind semisubmersible FOWT will be presented using the same condition sets as the OC3-Hywind spar FOWT: stability sensitivity and coherence sensitivity.

4.2.1.1 Stability Sensitivity

Results for the Højstrup model with varying stability will be focused on the blade root flap-wise bending moment, tower top torsion, and tower base fore-aft bending moment. Tower side-to-side moment and blade root edge-wise moment were not the focus of this analysis. Mooring line tensions did not show a clear pattern for this condition set and are therefore displayed in **Appendix A.1.2**.

Blade Root Flap-wise Bending Moment

The average normalized DELs for the blade root flap-wise moment are displayed in *Figure* 4.27. Note that these DELs are normalized with the Kaimal model below rated scenario using a *semisubmersible* foundation, whereas the results displayed in **Section 4.1** were normalized with the Kaimal model below rated scenario using a *spar* foundation.

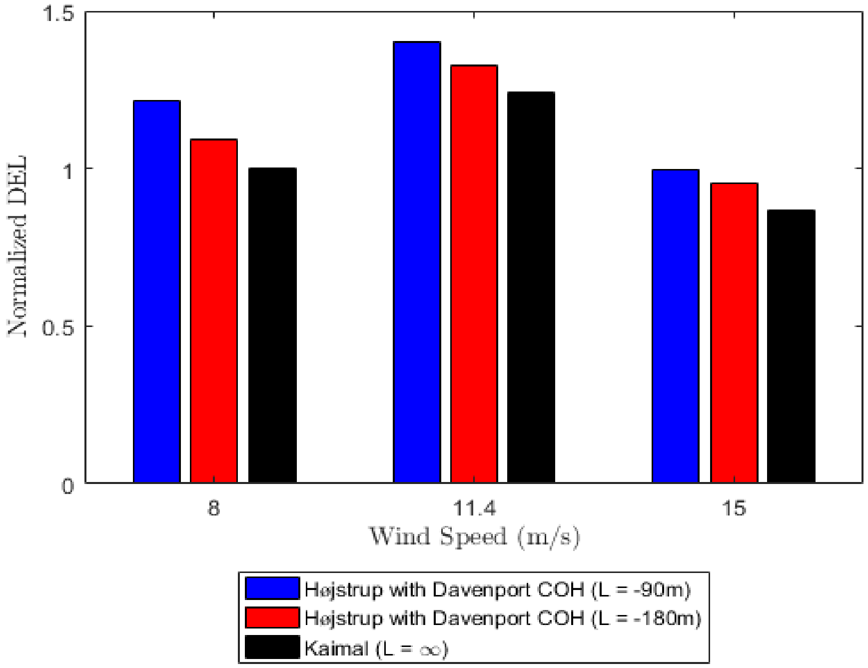

Figure 4.27: Normalized DEL for blade root flap-wise bending, normalized by the Kaimal model at 8 m/s, with the semisubmersible foundation

The Højstrup model under very unstable conditions resulted in the largest fatigue DELs for each wind speed, just as was seen when simulating the Højstrup model with varying stability on the spar-buoy FOWT. The maximum difference between very unstable conditions and neutral conditions, considering the same wind speed, was approximately 23%. In the case of a semisubmersible foundation, the largest fatigue loads occurred for rated wind speed, followed by below rated, and then above rated. This result is interesting and leads one to conclude that the pitching mechanism for the OC4-DeepCwind semisubmersible, which is very similar to the control methodology used for the OC3-Hywind spar [Robertson, et al., 2014], allows for the fatigue loads to be largely restrained for wind speeds above rated.

The blade root flap-wise bending moment was also analyzed using spectral density, which is presented in *Figures 4.28*, *4.29*, and 4.30 for the below rated, rated, and above rated wind speed scenarios, respectively.

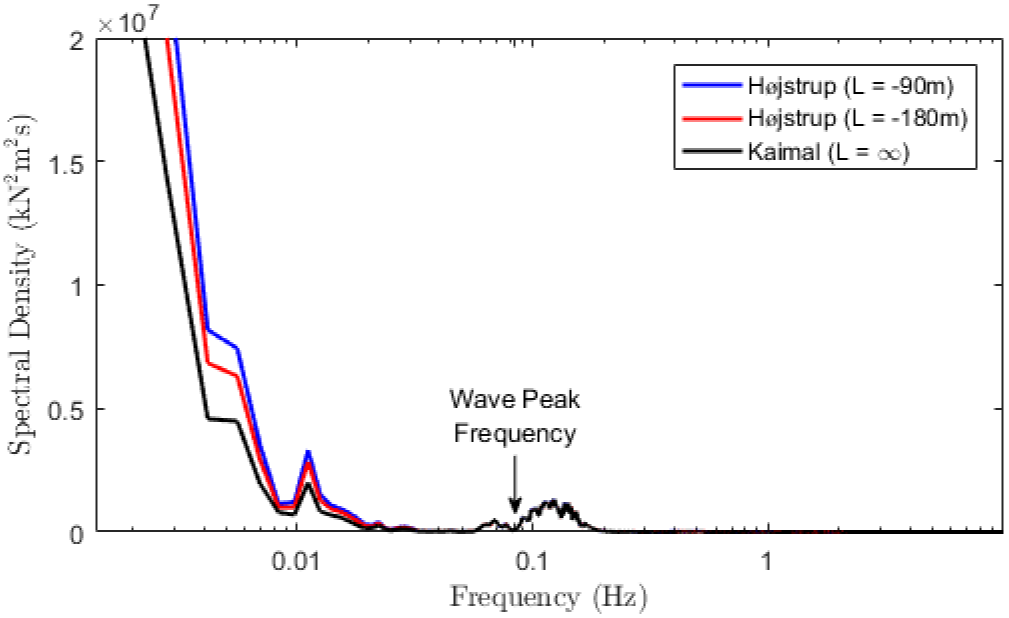

Figure 4.28: Spectral density of blade root flap-wise bending moment at below rated (8 m/s) wind speed with the semisubmersible foundation

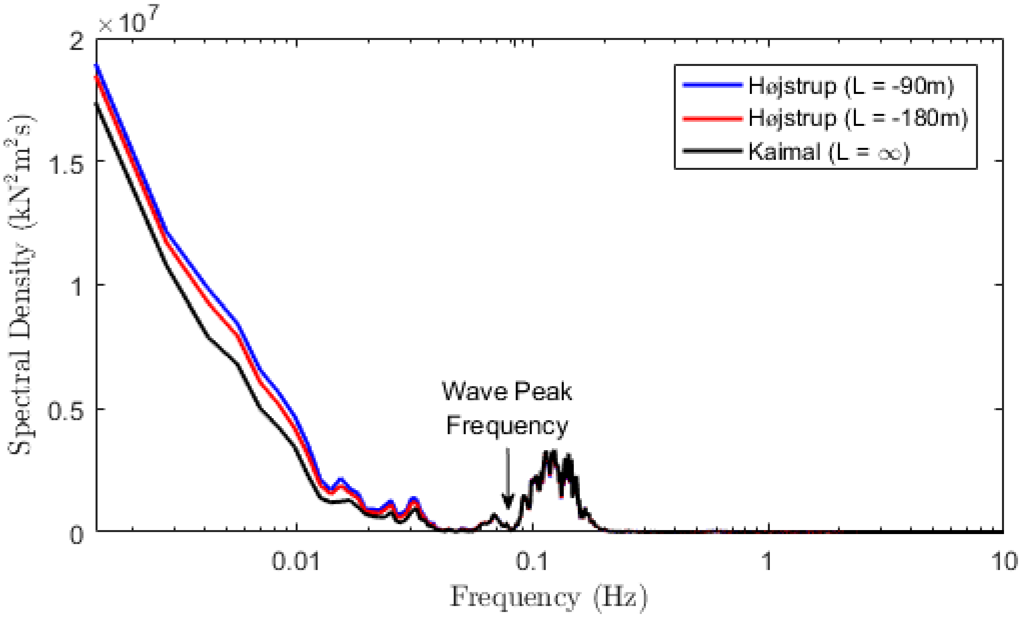

Figure 4.29: Spectral density of blade root flap-wise bending moment at rated (11.4 m/s) wind speed with the semisubmersible foundation

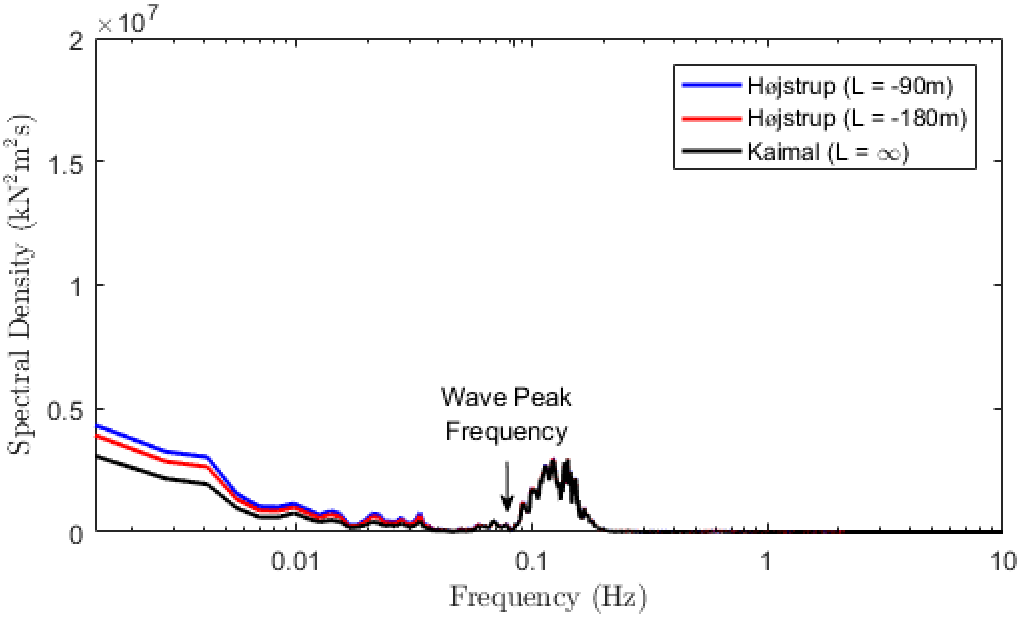

Figure 4.30: Spectral density of blade root flap-wise bending moment at above rated (15 m/s) wind speed with the semisubmersible foundation

The blade root flap-wise bending moment appears to exhibit an excitation response just after the wave peak frequency (0.083 Hz) and at low frequencies, where the difference between the Højstrup model with varying stability is most apparent. According to [Robertson et al., 2014], the low frequency responses follow dynamic wake theory, which delays the turbine's response to changes in the environmental conditions and therefore, dampens the higher frequency responses. This theory may explain why the largest excitation response occurred after the wave peak frequency, which shows a delayed response of the wind turbine.

Here, the spectral density is again displayed on a semi log x-scale, meaning that the response at the 3P frequency (0.48 Hz for below rated and 0.6 Hz for rated and above rated) is not highlighted. The differences in the Højstrup model with varying stability was evident around the 3P frequency, but the magnitude of the response was much smaller in comparison to the low frequency response.

Tower Top Torsion

The average DELs for the tower top torsion, normalized with the Kaimal model below rated scenario, are displayed in *Figure 4.31*.

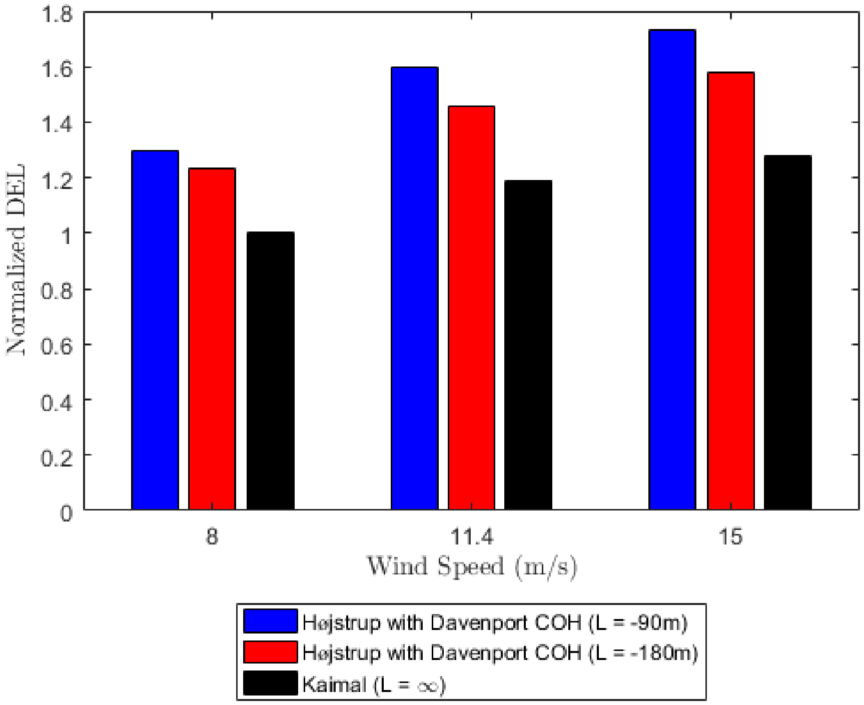

Figure 4.31: Normalized DEL for tower top torsion, normalized by the Kaimal model at 8 m/s with the semisubmersible foundation

The Højstrup model with very unstable conditions, associated with higher turbulence, resulted in the largest DELs for tower top torsion. The maximum difference between very unstable conditions and neutral conditions, considering the same wind speed, was approximately 30.4%. From the figure, it is also clear that the fatigue damage increases with increasing wind speed, as was seen in the research of both Putri [2016] and Bachynski and Eliassen [2019].

The power spectral density of tower top torsion is presented in *Figures 4.32, 433*, and 4.34 for the below rated, rated, and above rated wind speed scenarios, respectively.

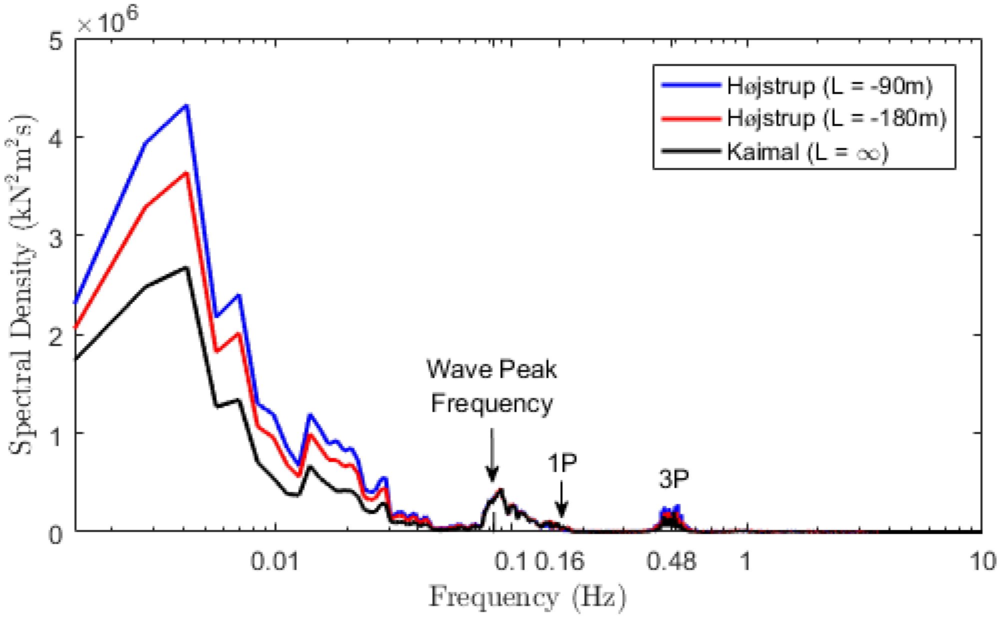

Figure 4.32: Spectral density of tower top torsion at below rated (8 m/s) wind speed with the semisubmersible foundation

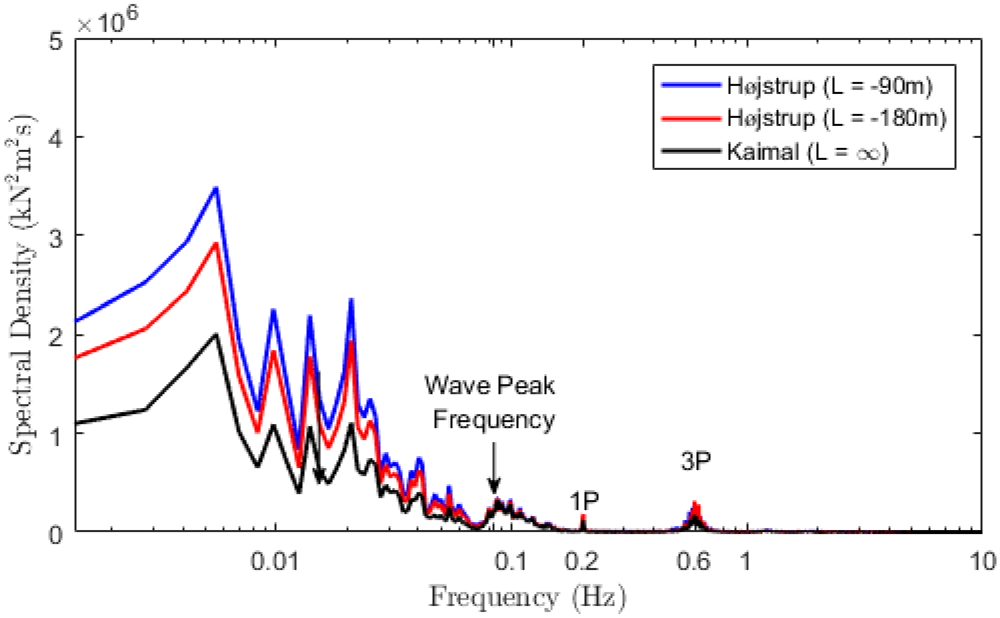

Figure 4.33: Spectral density of tower top torsion at rated (11.4 m/s) wind speed with the semisubmersible foundation

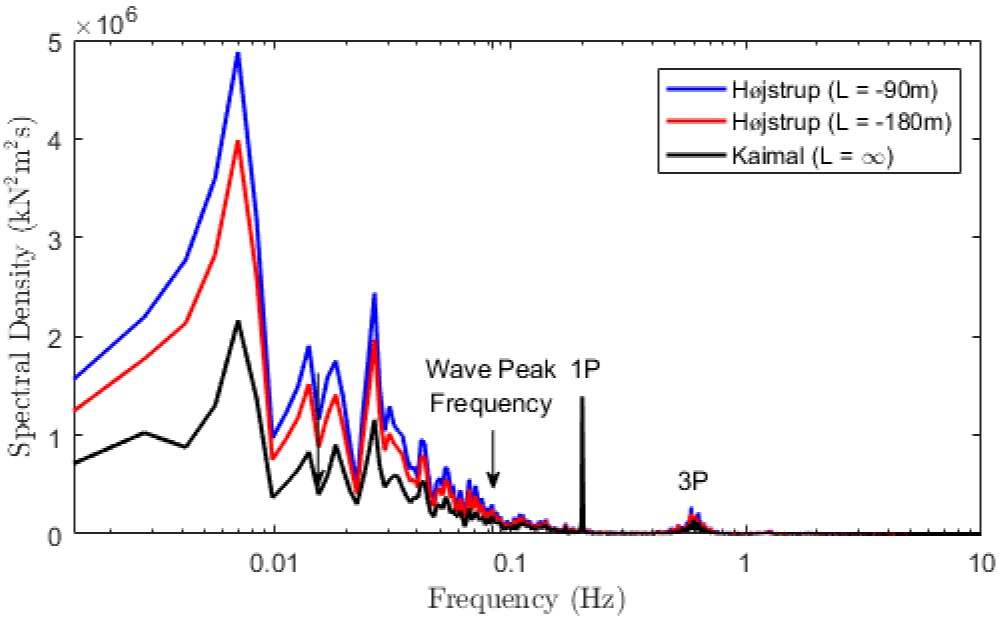

Figure 4.34: Spectral density of tower top torsion at above rated (15 m/s) wind speed with the semisubmersible foundation

For the tower top torsion, an excitation response occurred around the wave peak frequency, at the 1P and 3P frequencies, and at low frequencies. The magnitude of the response near the wave peak frequency decreased with increasing wind speed, whereas the response at the 1P frequency became sharper and larger with increasing wind speed. The low frequency behavior appeared to have the most significant contribution to the resulting fatigue loads, since very unstable conditions were notably larger than unstable and neutral conditions at low frequencies.

Tower Base Fore-Aft Moment

Comparatively, the tower base fore-aft moment did not result in significant changes between the different stability conditions analyzed. With that being said, the Højstrup model with very unstable conditions resulted in the largest DEL compared to unstable and neutral conditions for each wind speed. The maximum difference between very unstable conditions and neutral conditions, considering the same wind speed, was approximately 8.3%.

4.2.1.2 Vertical Coherence Sensitivity (Case 1)

For the OC4-DeepCwind FOWT, vertical coherence was also analyzed by using the Modified Coherence Function in conjunction with the Højstrup spectra model. The conditions of Case 1 remained the same, which involved keeping the horizontal decay coefficients constant while varying the vertical decay coefficients. A summary of Case 1 can be found in **Section 3.1.3**, which details the two sub-condition sets: Modified COH Case 1a and Modified COH Case 1b, both of which are listed in **Table 3.5**. It is also important to remember that Case 1a was found to be slightly more coherent than Case 1b, as seen in *Figure 4.11* in **Section 4.1.1.2**.

The DELs on the blade root flap-wise bending moment, tower top torsion, and tower base fore-aft moment were considered the most important in analyzing the Højstrup model for vertical coherence sensitivity, and will be discussed in this section. The DELs for the mooring line tension showed no clear pattern, so these results are presented in **Appendix A.1.2.**

Blade Root Flap-wise Bending Moment

The average normalized DELs for the blade root flap-wise bending moment with varying vertical coherence (Case 1), normalized with the Kaimal model below rated scenario, are displayed in *Figure 4.35*.

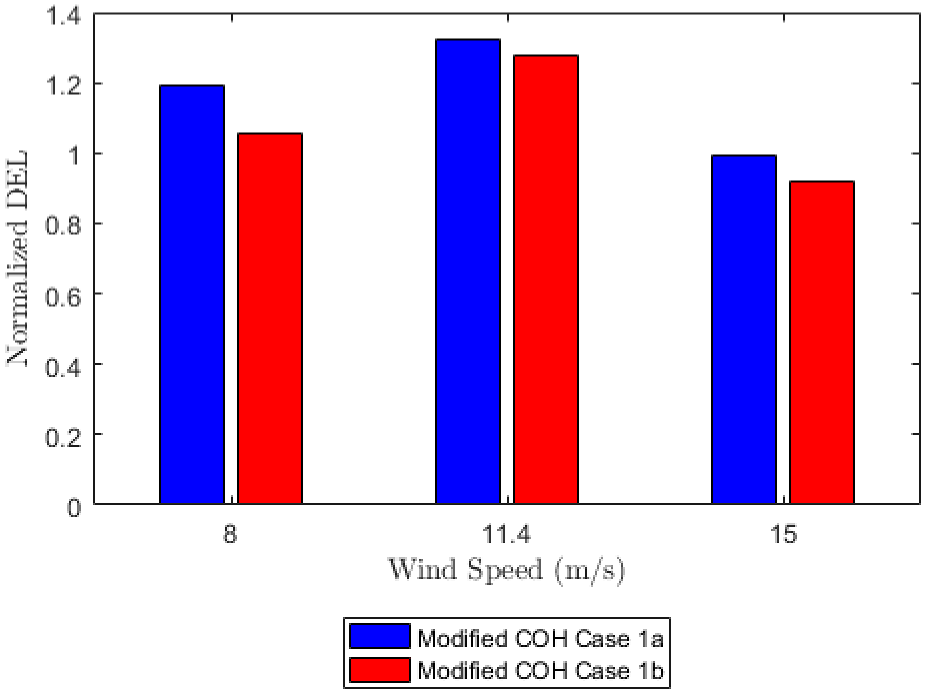

Figure 4.35: Normalized DEL for blade root flap-wise bending, normalized by the Kaimal model at 8 m/s, for the Højstrup spectra model with varying **vertical** coherence with the semisubmersible foundation

The resulting DELs show that the more coherent wind field, simulated under the Modified Coherence Function Case 1a, gave the largest fatigue loads for the blade root flap-wise bending moment, with a maximum difference of 38.8% between Case 1a and Case 1b. As pointed out earlier, a higher vertical coherence leads to higher fatigue loads on the turbine blades, which was also seen here for the semisubmersible foundation.

The average normalized DELs for the tower top torsion and tower base fore-aft moment with varying vertical coherence (Case 1), normalized with the Kaimal model below rated scenario, are displayed in *Figures 4.36* and *4.37*.

Tower Top Torsion

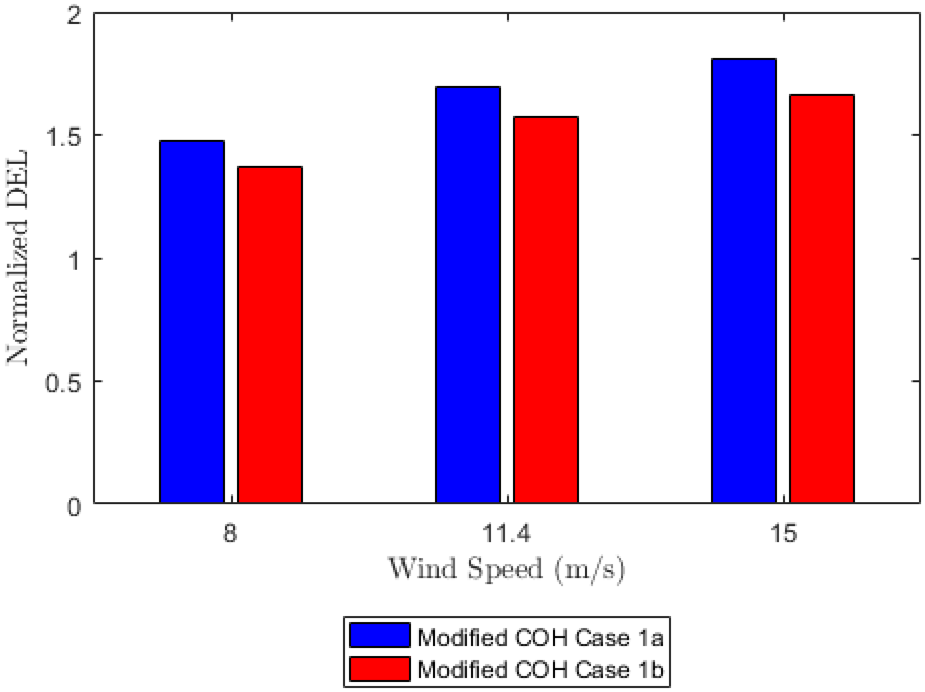

Figure 4.36: Normalized DEL for tower top torsion, normalized by the Kaimal model at 8 m/s, for the Højstrup spectra model with varying **vertical** coherence with the semisubmersible foundation

Tower Base Fore-aft Moment

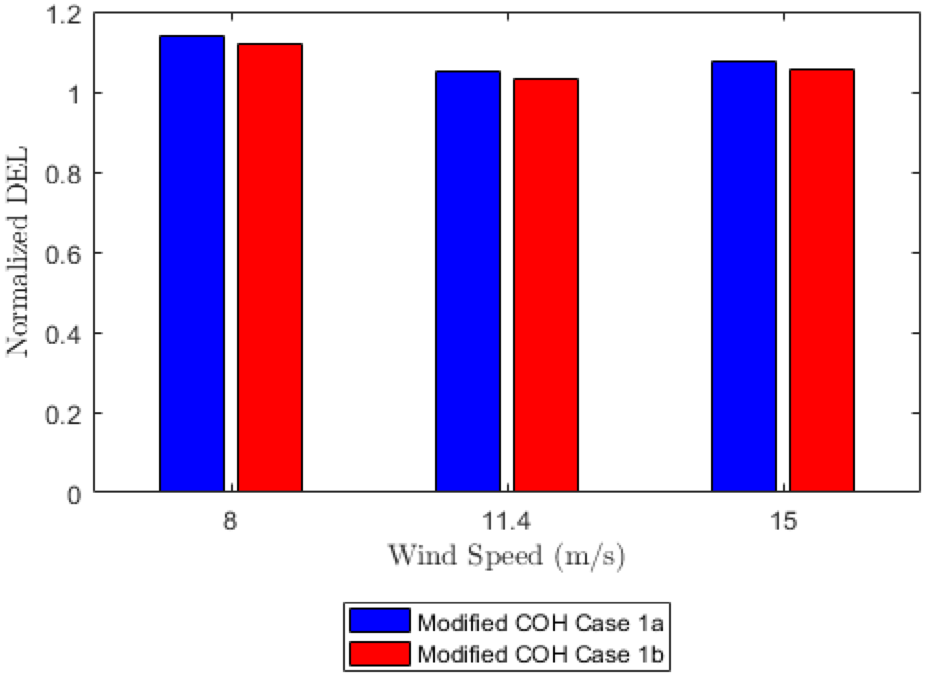

Figure 4.37: Normalized DEL for the tower base fore-aft moment, normalized by the Kaimal model at 8 m/s, for the Højstrup spectra model with varying **vertical** coherence with the semisubmersible foundation

Similar to the results found for the blade root flap-wise moment, the highest fatigue loads for tower top torsion and tower base fore-aft moment occurred for the more coherent wind field, Case 1a. The maximum difference between Case 1a and 1b was 16.1% for tower top torsion and 12.6% for the tower base fore-aft moment. It can also be seen that the fatigue loads for tower top torsion increased with increasing wind speed, whereas, the largest fatigue loads for the tower base fore-aft moment occurred for below rated wind speed, followed by above rated and rated wind speeds. For a typical wind turbine design, when the wind speed increases above rated wind speed, the tower base begins to pitch, causing a reduction in the loads [Sathe et al., 2013]. However, this result is different than what was seen for the blade root flap-wise moment, where fatigue loads were largest at rated wind speed, followed by below and above rated.

4.2.1.3 Lateral Coherence Sensitivity (Case 2)

Lateral coherence sensitivity was evaluated by applying the Modified Coherence Function Case 2, defined earlier in **Section 3.1.3**, with the two sub-condition sets: Modified COH Case 2a and Modified COH Case 2b, listed in **Table 3.6**. The blade root flap-wise bending moment, as well as tower top torsion were considered for this analysis, while the tower base fore-aft moment and the mooring line tensions will not be addressed further as the results for these modes showed no clear pattern.

Blade Root Flap-wise Bending Moment

The average normalized DELs for the blade root flap-wise bending moment with varying lateral coherence (Case 2), normalized with the Kaimal model below rated scenario, are displayed in *Figure 4.38*.

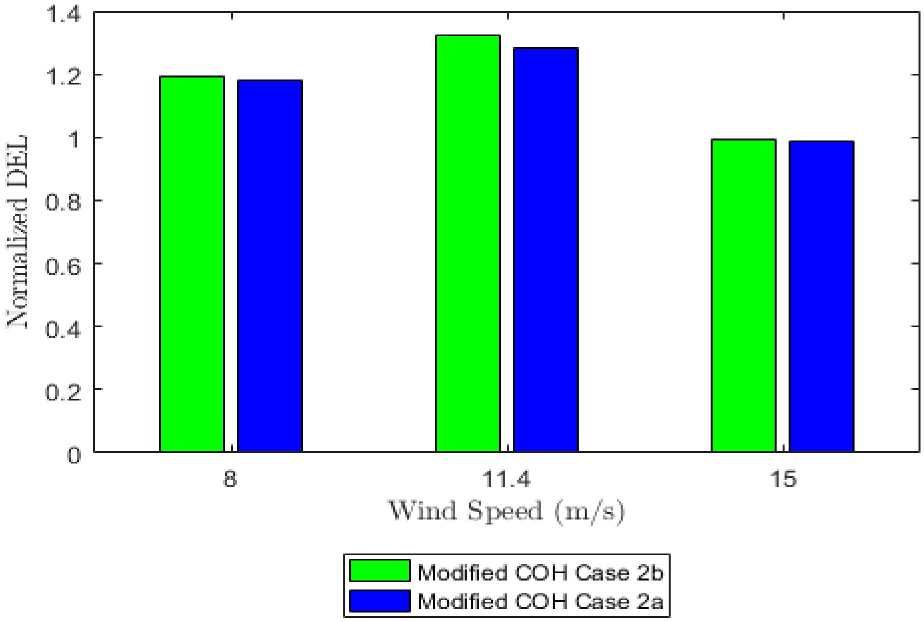

Figure 4.38: Normalized DEL for blade root flap-wise moment, normalized by the Kaimal model at 8 m/s, for the Højstrup spectra model with varying **lateral** coherence, with the semisubmersible foundation

Again, the blade root flap-wise moment was influenced the most by the more coherent wind field, Case 2b. The maximum difference between Case 2b and Case 2a was 13.6%. Comparing this value to the result of varying vertical coherence, 38.8%, it seems as though the blade root flap-wise moment is more affected by changes in vertical coherence than lateral coherence. This conclusion is most likely related to the pitching mechanism of the wind turbine, which rotates around the y-axis, and thus varies in relation to the vertical plane.

Tower Top Torsion

The average normalized DELs for tower top torsion with varying lateral coherence (Case 2), normalized with the Kaimal model below rated scenario, are displayed in *Figure 4.39*.

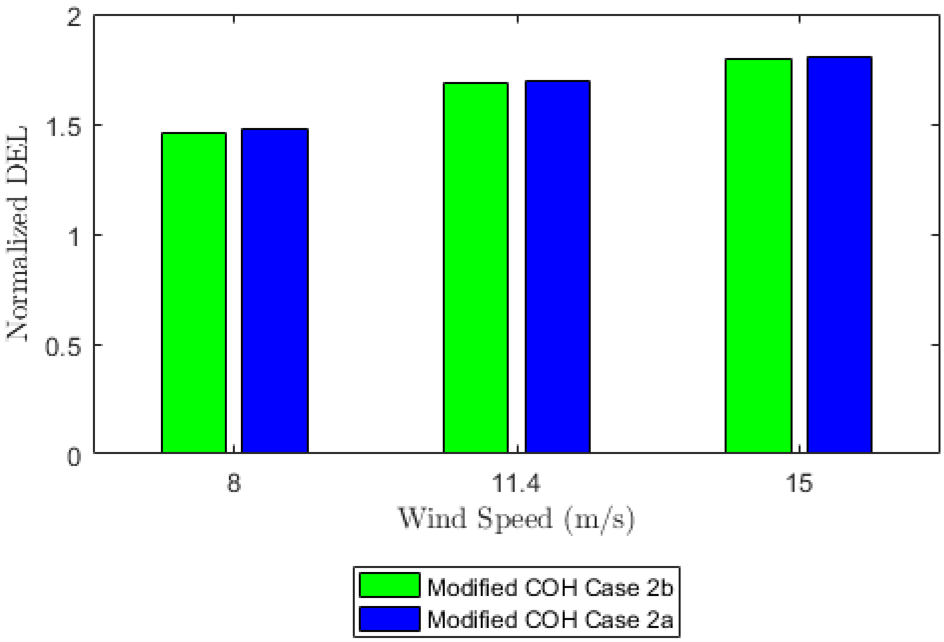

Figure 4.39: Normalized DEL for tower top torsion normalized by the Kaimal model at 8 m/s, for the Højstrup spectra model with varying **lateral** coherence, with the semisubmersible foundation

In contrast to the fatigue loads on the turbine blades, the tower top torsion resulted in the largest fatigue loads using a less coherent wind field, corresponding to Case 2a. The maximum difference between Case 2a and Case 2b was 20.7% when considering the same wind speed. This result indicates that the tower top torsion is more influenced by a variation in lateral coherence than a variation in vertical coherence, and reinforces the theory that the tower top torsion is linked to the platform yaw motion.

4.2.2 Platform Motions

In addition to affecting the loads in various components of the wind turbine, the defined wind fields also had an effect on the platform motions. The OC4 DeepCwind semisubmersible was designed so that the natural frequencies would fall below the range of typical wave frequencies, and theoretically reduce the platform response. The natural frequencies of the platform motions for the OC4-DeepCwind FOWT, found through testing in “still water and no wind” [Robertson et al., 2014], are displayed back in **Chapter 3**, *Table 3.3*.

4.2.2.1 Stability Sensitivity

The platform motions most affected by varying atmospheric stability conditions using the OC4-DeepCwind FOWT included surge, sway, pitch, and yaw, and are therefore be presented in this section. The remaining platform motions are displayed in **Appendix B.1.2**. These platform motions were analyzed using power spectral densities, as displayed in *Figures 4.40 – 4.43*.

Surge

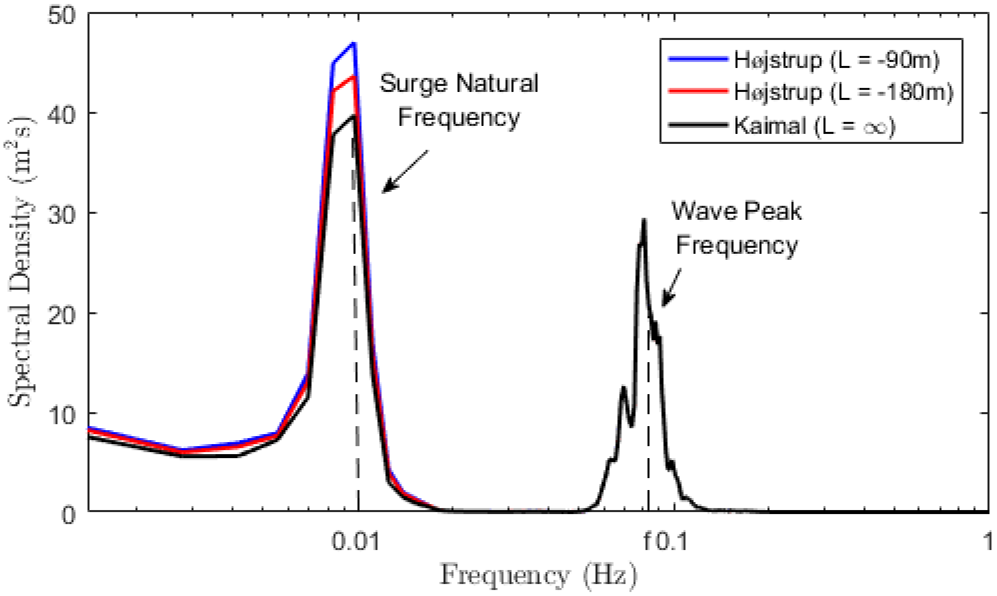

Figure 4.40: Spectral density of surge displacement for varying stability at rated wind speed (11.4 m/s) with the semisubmersible foundation

Sway

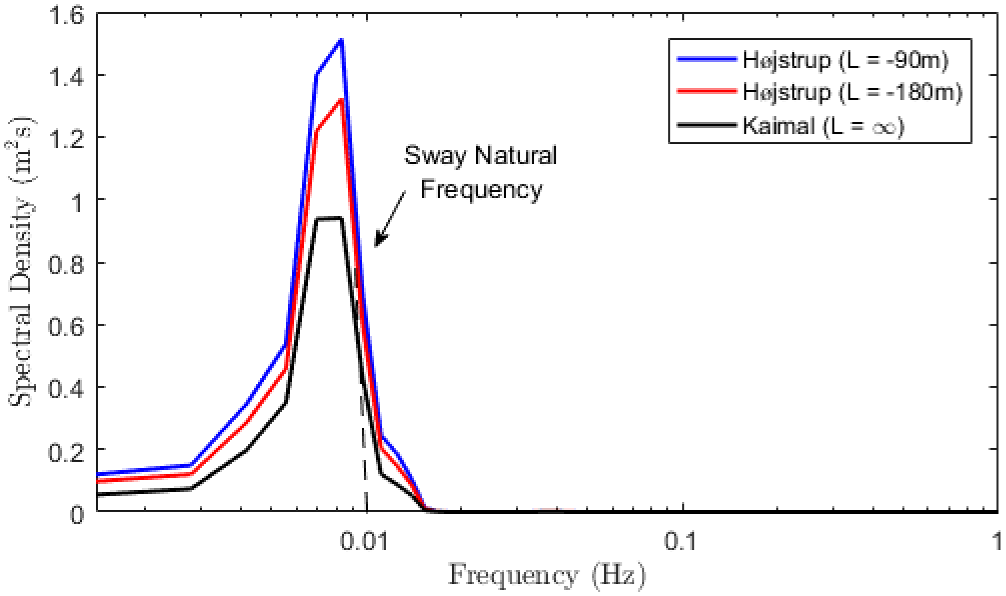

Figure 4.41: Spectral density of sway displacement for varying stability at rated wind speed (11.4 m/s) with the semisubmersible foundation

Pitch

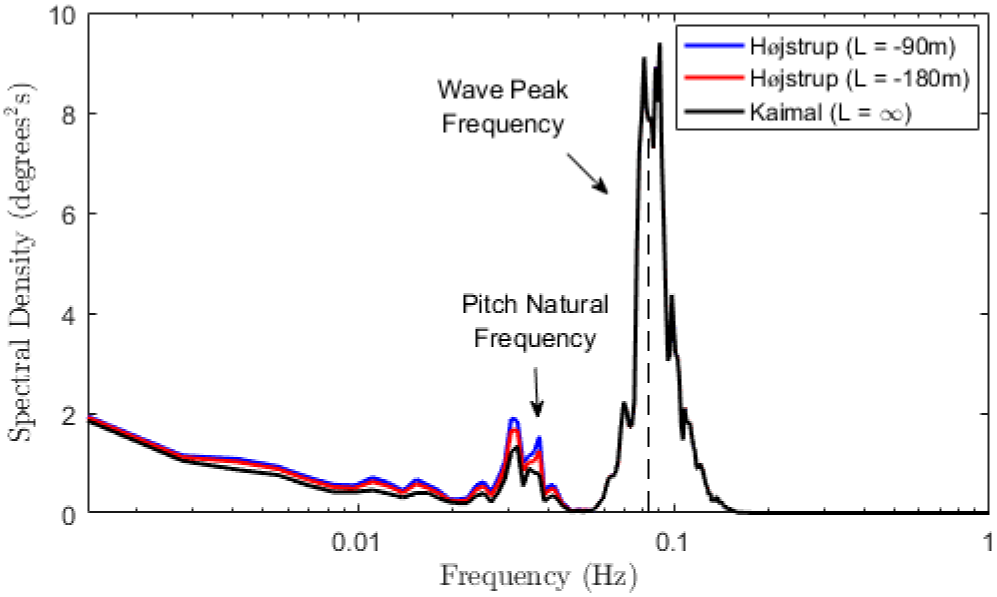

Figure 4.42: Spectral density of pitch rotation for varying stability at rated wind speed (11.4 m/s) with the semisubmersible foundation

Yaw

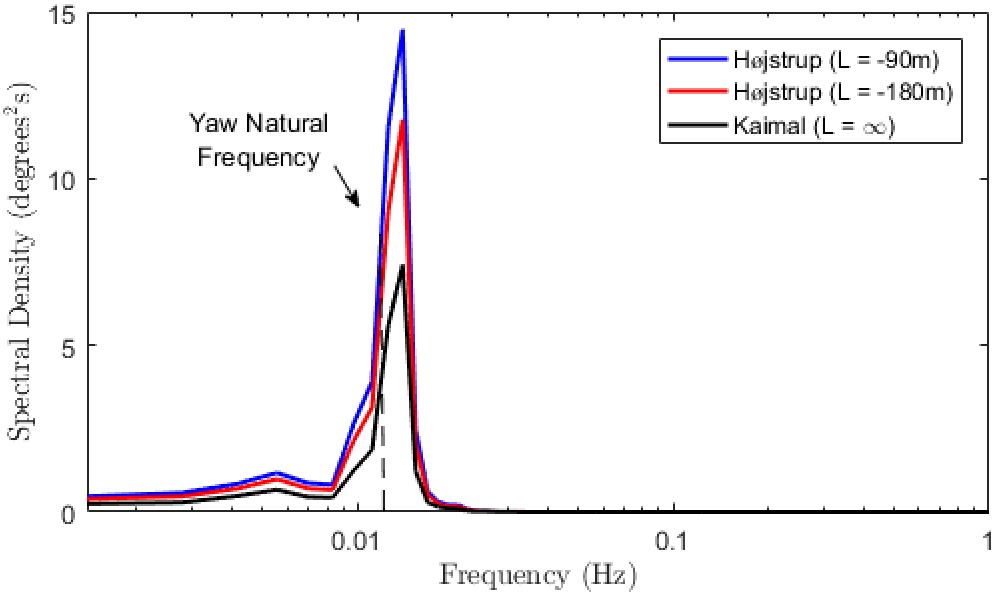

Figure 4.43: Spectral density of yaw rotation for varying stability at rated wind speed (11.4 m/s) with the semisubmersible foundation

Under the conditions created using the OC4-DeepCwind FOWT, platform surge displacement and pitch rotation were both influenced by the wave peak frequency (0.083 Hz) and their respective natural frequencies; surge (0.01 Hz) and pitch (0.04 Hz). On the other hand, the platform sway displacement and yaw rotation were only influenced by their natural frequencies (sway: 0.01 Hz and yaw: 0.012 Hz) and exhibited no response at the wave peak frequency. Since a semisubmersible foundation is typically characterized by a soft mooring tension and a large moment of inertia in yaw [Bachynski and Eliassen, 2019], it seems likely that the yaw response would primarily occur at the yaw natural frequency.

The study by Bachynski and Eliassen [2019] found that a FOWT with a semi-submersible foundation had a larger platform pitch response at the pitch natural frequency compared to the wave natural frequency, unlike the results seen here. However, the semi-submersible foundation used in that study has the wind turbine tower connected to one of the offset columns, which is different than the OC4-DeepCwind semisubmersible used in this study, where the wind turbine is placed on the main column, situated in the center of the platform.

For each platform motion presented, the Højstrup model under very unstable conditions maintained the largest spectral energy, which is most likely attributed to very unstable conditions having a higher turbulence and larger turbulent fluctuations. Since each degree of freedom for the OC4-DeepCwind FOWT has a fairly low natural frequency, there was no significant excitation response at frequencies higher than the wave peak frequency.

4.2.2.2 Coherence Sensitivity

Coherence sensitivity had very little influence on the OC4-DeepCwind platform motions. Therefore, the pitch and yaw rotations for vertical and lateral coherence sensitivity, respectively, are displayed in **Appendix B.1.2**.

4.3 Comparison of OC3-Hywind Spar & OC4-DeepCwind Semisubmersible

In order to visualize how changing the foundation type influenced the FOWTs defined in this study, the DELs for the blade root flap-wise moment, tower top torsion, and tower base fore-aft moment were compared using the OC3-Hywind spar-buoy FOWT and the OC4-DeepCwind semisubmersible FOWT. The DELs for the aforementioned turbine components were simulated using the Højstrup 1981 Unstable Spectra Model under very unstable conditions, paired with the Davenport Coherence Function, and are presented in *Figures 4.44 - 4.46*. These DELs are not normalized to provide a clear picture of the fatigue loads.

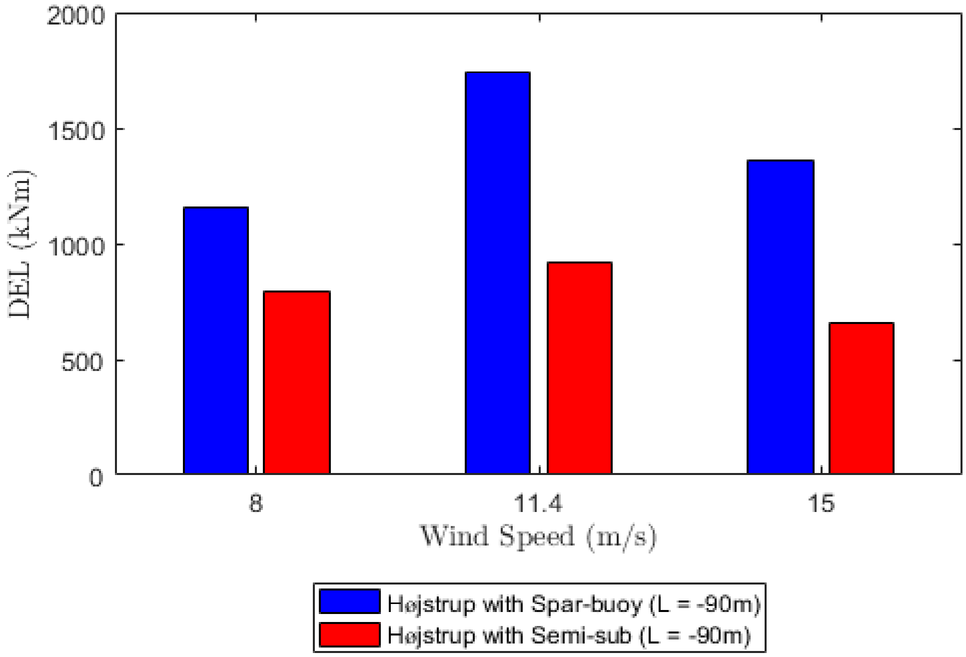

Figure 4.44: DEL for blade root flap-wise bending for the Højstrup model with varying foundation type

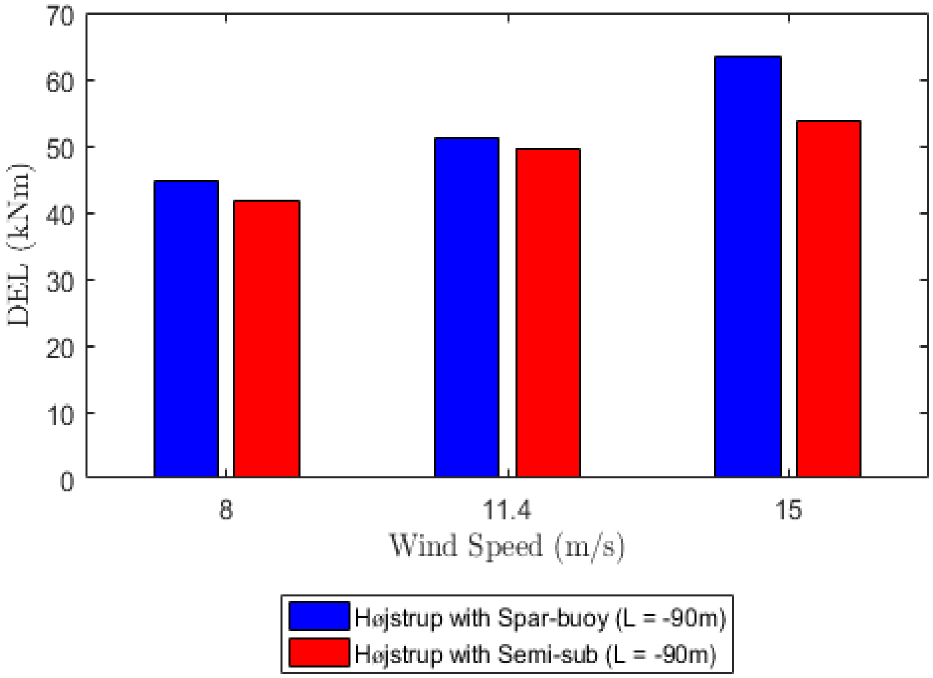

Figure 4.45: DEL for tower top torsion for the Højstrup model with varying foundation type

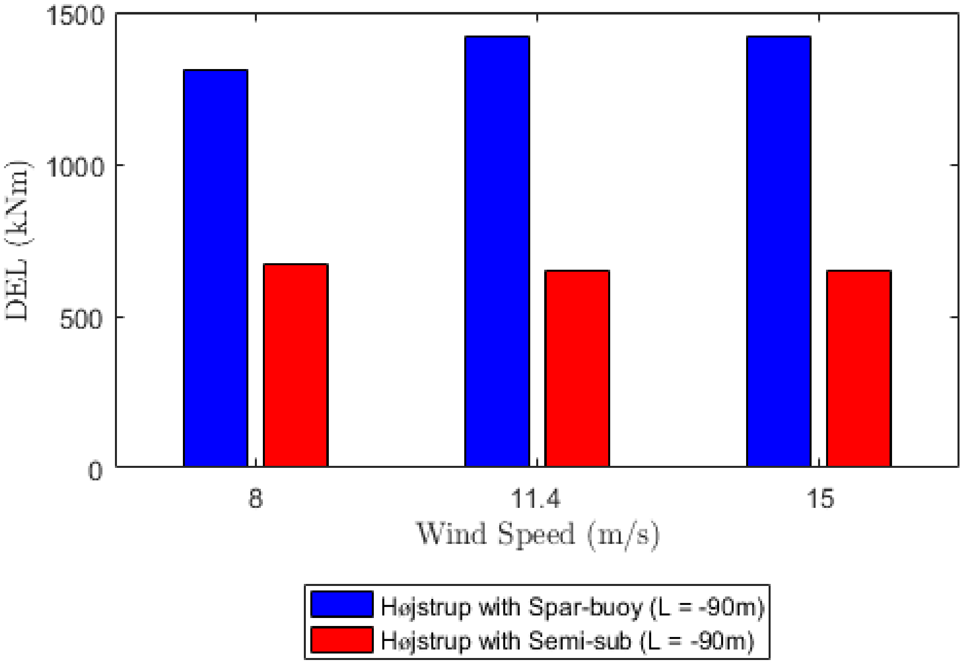

Figure 4.46: DEL for tower base fore-aft moment for the Højstrup model with varying foundation type

From *Figures 4.44 - 4.46,* it is evident that the simulations using the OC3-Hywind spar-buoy type foundation resulted in greater fatigue loads than simulations using the OC4-DeepCwind semisubmersible foundation. The differences were significantly larger when comparing the fatigue loads for the tower base fore-aft moment, with a maximum difference of 71%, considering the same wind speed. The blade root flap-wise moment also showed significant differences, with a maximum difference of 64.2%. For tower top torsion, the maximum difference between the OC3-Hywind and OC4-DeepCwind FOWTs was 33.2%, considering the same wind speed. The differences between the spar and the semisubmersible foundation may have something to do with how each foundation achieves its stability. Similar to other semisubmersible designs, the OC4-DeepCwind semisubmersible achieves good stability in wind and waves due to its large waterplane area, which limits the platform motion in roll and pitch [Cheng, et al., 2015]. On the other hand, the OC3-Hywind spar-buoy achieves stability with its heavy ballast, which can also reduce platform roll and pitch. The spar-buoy defined in this study also has a lower moment of inertia in both pitch and yaw, which means less force is needed from wind and waves to cause the FOWT to rotate. Additionally, the semisubmersible has a lower yaw natural frequency, far from the wave peak frequency. As seen in **Section 4.2.2.1**, the semisubmersible showed little to no yaw response at the wave peak frequency, whereas, the spar-buoy did, as seen in **Section 4.1.2.1**.

Bachynski and Eliassen [2019] also compared fatigue loads between different platform foundations and found that the tower top torsion is relatively similar between spar and semisubmersible types for wind speeds of 15 m/s and lower, although the semisubmersible experienced somewhat larger fatigue loads. It was also found that the semisubmersible resulted in larger loads on the tower base fore-aft moment compared to simulations using the spar-buoy, which is substantially different than the results seen here. Unfortunately, a perfect comparison between this study and the study of Bachynski and Eliassen [2019] cannot be made since the semisubmersible FOWT used in that study has a different arrangement than the OC4-DeepCwind semisubmersible.

Another comparative study by Cheng et al. [2015] should be made note of, which looked at the dynamic responses of three floating wind turbine concepts: the OC3 spar, the OC4 semisubmersible, and a tension leg platform (TLP). Unlike the simulations of this study, which used a horizontal axis wind turbine (HAWT), the study by Cheng et al. [2015] used these floating concepts in conjunction with a 5 MW Darrieus rotor, a vertical axis wind turbine (VAWT) design. Although this again is not the best comparison, the study by Cheng, et al. [2015] found that the mean values for the tower base fore-aft moment using a spar foundation were larger than the mean values for the semisubmersible foundation, which is aligned with the results seen here.

Since one of the main objectives of this study was to analyze the influence of atmospheric stability conditions on a FOWT, it was interesting to see that varying the atmospheric stability influenced the blade root flap-wise moment more when using the semisubmersible foundation than when using the spar-buoy foundation, with a 23% difference between very unstable and neutral conditions for the semisubmersible and a 7.5% difference for the spar-buoy. On the other hand, tower top torsion was more influenced by changes in atmospheric stability with the spar-buoy foundation, since the maximum difference between very unstable and neutral conditions was 47% for the spar-buoy and 30.4% with the semisubmersible.

5. Conclusion

In this study, fatigue loads and platform motions were computed and discussed in order to analyze the influence of different unstable turbulent wind fields and simulated wind coherence on a floating offshore wind turbine, specifically using the Højstrup 1981 Unstable Spectra Model. Results were presented using normalized damage equivalent loads and power spectral density plots of the loads and platform motions, with stability and coherence sensitivity. The most significant difference between the turbulent wind fields generated in this study was observed for the tower top torsion under varying stability conditions. Very unstable conditions resulted in fatigue loads for the tower top torsion that were 47% larger than neutral conditions for the OC3-Hywind FOWT and 30.4% larger for the OC4-DeepCwind FOWT. As expected, very unstable conditions corresponded to the highest turbulence intensities and the largest turbulent fluctuations. This is due to the inclusion of buoyancy generated turbulence, which, consequently, resulted in larger fatigue loads for the tower top torsion. The blade root flap-wise and tower base fore-aft bending moments were relatively unaffected by variations in turbulence. In an offshore environment, unstable atmospheric conditions are typically dominant [Sathe et al., 2013], and should therefore be considered for the design calculations of FOWTs. Since the fitted Mann model does not take into account the added effect of buoyancy generated turbulence, this may explain why the results from both Putri [2016] and Sathe et. al [2013] found that the highest turbulence correlated to neutral conditions. However, it is important to recognize that very unstable conditions are typically associated with lower wind speeds than neutral and moderately unstable conditions [Cheynet et al., 2018].

Variations in unstable conditions had more of an influence on the loads and motions of the OC3-Hywind and OC4-DeepCwind FOWTs than variations in wind coherence. With that being said, vertical coherence was shown to have some impact on the blade root flap-wise moment and pitch rotation, and lateral coherence affected the tower top torsion and yaw rotation. A higher vertical coherence was linked to higher fatigue loads on the blade root flap-wise bending moment, with a 16.25% and 38.8% difference for the OC3-Hywind and OC4-DeepCwind FOWT, respectively. On the other hand, a higher lateral coherence resulted in lower fatigue loads for the tower top torsion, with a 13.4% and 20.7% difference for the OC3-Hywind and OC4-DeepCwind FOWT, respectively. Overall, coherence sensitivity was fairly insignificant. From the results, one can conclude that the inclusion of the low frequency content when simulating unstable conditions was of more importance than changes in coherence. Additionally, the low frequency behavior was most important for both the damage equivalent loads and platform motions, especially the low frequency yaw response. This result is connected to the eigen frequencies of the FOWT, which are relatively low and, therefore, led to a larger response of low frequency fluctuations.

The purpose of the Højstrup model is to include the low frequency response of wind turbulence, which was found to be particularly influential in the resulting loads and platform motions. However, it is important to remember that the Højstrup model was developed based on measurements collected in Kansas, USA and Minnesota, USA [Højstrup, 1982]. This is a noteworthy limitation of the Højstrup model in the fact that the model is based on onshore measurements and may not fully capture the conditions typically found offshore. In addition, a limitation of the Kansas research is that measurements were cut off at 5 minutes, which has the effect of applying a high pass filter. This effect may have attenuated the spectra components at low frequencies, limiting their contribution to the model.

Considering these limitations, the use of an alternate composite spectral model developed in the work of Cheynet et al. [2018] is suggested, which uses local similarity theory and a combination of a pointed and a blunt model to describe the wind turbulence spectra for different atmospheric stabilities. The resulting spectra incorporated measurements collected from the FINO1 platform and would most likely result in a better depiction of unstable conditions for an offshore environment. However, using just one turbulence model to describe different offshore sites may not be a reasonable assumption. Jonkman and Veers [2019] concluded that specific turbulence intensity levels are needed to accurately represent offshore sites, which can be dominated by different atmospheric stability conditions. Therefore, implementation of the Pointed-blunt model would be best suited for a location with similar site conditions as was found at the FINO1 platform.

5.1 Future Work & Recommendations

To further the analysis of this study, recommended future work includes:

- Implementation of the Pointed-blunt model developed by Cheynet et al. [2018]
- Improve the Højstrup 1981 Unstable Spectra Model through sensitivity studies and parameterizations
- Conduct a thorough eigen frequency analysis for both the OC3-Hywind and OC4-DeepCwind FOWTs and determine the associated transfer functions, with simulations excited by white noise or an impulse load
- Further study of lateral wind coherence, since lateral effects have primarily been the focus of research in bridge engineering
- Sensitivity study on increasing the turbine rotor size (i.e. 10 MW DTU reference wind turbine) to analyze the effect of larger wind turbines on the fatigue loads and platform motions
- Running simulations with parameterizations of boundary layer height as suggested by Beljaars [1992]

References

1. Air Pollution Training Institute. (accessed 2019). *PBL Defined*. OS 411: Computational Atmospheric Sciences. The Shodor Education Foundation, Inc. [Image Online] Available at: < https://www.shodor.org/os411/courses/411c/module06/unit01/page01.html > [Accessed February 21, 2019]
2. *Atmospheric Stability: Stability of Dry Air*. (uploaded 2011, accessed 2019) PowerPoint PPT Presentation. SlideServe. Available at: < https://www.slideserve.com/Jimmy/atmospheric-stability > [Accessed January 2019]
3. Bachynski, E. and Eliassen, L. (2019). *The effects of coherent structures on the global response of floating offshore wind turbines*. Wind Energy. John Wiley & Sons, Ltd.
4. Beljaars, A. (1992). *The parameterization of the planetary boundary layer*. European Centre for Medium-Range Weather Forecasts. Meteorological Training Course Lecture Series.
5. Betz, A. (1926). *Wind Energie und ihre Ausnutzung durch Windmühlen* (Wind Energy and its Extraction through Windmills). Göttingen, Vandenhoeck.
6. Bui, Chuan, et al. [Accessed 2019]. *Stabilizing Systems*. Floating Wind Turbines. Weebly. Available at: < floatingwindfarm.weebly.com/stabilizing-systems.html > [Accessed January 2019]
7. Charnock, H. (1955). *Wind Stress on a Water Surface*. Quarterly Journal of the Royal Meteorological Society, 81(350), pp. 639 – 640.
8. Cheng, Z., Wang, K., Gao, Z., and Moan, T. (2015). *Dynamic Modelling and Analysis of Three Floating Wind Turbine Concepts with Vertical Axis Rotor*. ISOPE 2015 pp. 415-423.
9. Cheynet, E., Jakobsen, J., and Obhrai, C. (2017). *Spectral characteristics of surface-layer turbulence in the North Sea*. Science Direct. Energy Procedia 137, pp. 414-427.
10. Cheynet, E. (2018). *Wind field simulation (the fast version)*. MathWorks File Exchange. Available at: < https://se.mathworks.com/matlabcentral/fileexchange/68632-wind-field-simulation-the-fast-version > [Accessed September 2018]
11. Cheynet, E. and Jakobsen, J. (2018). *Wind Load on Structures Part 1*. Course- OFF580 Marine Technology. 14 March 2018.
12. Cheynet, E., Jakobsen, J., Reuder, J. (2018). *Velocity Spectra and Coherence Estimates in the Marine Atmospheric Boundary Layer*. Boundary-Layer Meteorology. Springer Nature B.V.
13. Chougule, A. (2017). *Modeling Atmospheric Turbulence via Rapid Distortion Theory: Spectral Tensor of Velocity and Buoyancy*. Journal of the Atmospheric Sciences, Vol. 74.

14. Davenport, A.G. (1961). *The Spectrum of Horizontal Gustiness near the Ground in High Winds*. Quarterly Journal of the Royal Meteorological Society 87, pp. 194-211.
15. Det Norske Veritas AS. (2010). *DNV-RP-C205: Environmental Conditions and Environmental Loads*. Oslo: Veritas Offshore Technology and Service AS, DNV.
16. Driscoll, F., Jonkman, J., Robertson A., Sirnivas, S., Skaare, B., and Nielsen, F. (2016). *Validation of a FAST Model of the Statoil-Hywind Demo Floating Wind Turbine*. 13th Deep Sea Offshore Wind R&D Conference, EERA, DeepWind'2016, Trondheim, Norway. Energy Procedia 94, pp. 3-19.
17. Eliassen, L., Jakobsen, J., and Krokstad, J. (2015). *The effect of turbulent wind field on loads of a wind turbine rotor of increasing size*. 14th International Conference on Wind Engineering, Porto Alegre, Brazil.
18. Eliassen, L. and Obhrai, C. (2016). *Coherence of turbulent wind under neutral wind conditions*. 13th Deep Sea Offshore Wind R&D Conference, EERA DeepWind'2016, Trondheim, Norway. Energy Procedia 94, pp. 388-398.
19. Gitano-Briggs, H. (2012). *Low Speed Wind Turbine Design*. Advances in Wind Power. IntechOpen, DOI: 10.5772/53141. Available at: < https://www.intechopen.com/books/advances-in-wind-power/low-speed-wind-turbine-design >
20. Gryning, S., Batchvarova, E., Brümmer, B., Jørgensen, H., & Larsen, S. (2007). *On the Extension of the Wind Profile over Homogeneous Terrain beyond the Surface Boundary Layer*. Boundary Layer Meteorology, 124, pp. 251 – 268.
21. *GWEC Global Wind Report*. (April 2018). Annual Market Update 2017. Global Wind Energy Council.
22. Hasselmann, et al, (1973) *Measurements of wind-wave growth and swell decay during the Joint North Sea Wave Project (JONSWAP).* Deutsche Hydro. Zeitschr. Riehe, A8
23. Haugen, D. A., Kaimal, J. C. and Bradley, E.F. (1971). *An experimental study of Reynolds stress and heat flux in the atmospheric surface layer*. Quart. J. R. Met. Soc., 97, pp. 168-180
24. Holtslag, M.C., Bierboom, W.A.A.M, and van Bussel, G.J.W. (2016). *Wind turbine fatigue loads as a function of atmospheric conditions offshore*. Wind Energy, 19, pp. 1917-1932.
25. Högström, U. (1988). *Non-dimensional wind and temperature profiles in the atmospheric surface layer: A re-evaluation*. Boundary-Layer Meteorology, Vol. 42, Issue 1-2, pp. 55-78.
26. Højstrup, J. (1981). *A Simple Model for the Adjustment of Velocity Spectra in Unstable Conditions Downstream of an Abrupt Change in Roughness and Heat Flux*. Boundary-Layer Meteorology 21 pp. 341-356.

27. Højstrup, J. (1982). *Velocity Spectra in the Unstable Planetary Boundary Layer*. J Atmos Sci 39(10): pp. 2239–2248.
28. Højstrup, J. (1999). *Spectral coherence in wind turbine wakes*. Journal of Wind Engineering and Industrial Aerodynamics 80: pp. 137-146.
29. International Electrotechnical Commission (2005*). IEC 61400-1 Wind turbines- Part 1: Design Requirements*. Geneva: International Electrotechnical Commission, IEC.
30. Jonkman, J., Butterfield, S., Musial, W., and Scott, G. (2009). *Definition of a 5-MW Reference Wind Turbine for Offshore System Development*. NREL/TP-500-38060.
31. Jonkman, J. (2010). *Definition of the Floating System for Phase IV of OC3*. National Renewable Energy Laboratory (NREL), Golden.
32. Jonkman et al. (2010). *Offshore Code Comparison Collaboration within IEA Wind Task 23: Phase IV Results Regarding Floating Wind Turbine Modeling*. Conference Paper. NREL/CP-500-47534.
33. Jonkman, J. and Veers, P. (2019). *DNV GL Joint Industry Project on Validation of Turbulence Models*. Cooperative Research and Development Final Report, CRD-17-673. NREL/TP-5000-73167.
34. Kaimal, J.C., Wyngaard, J.C., Izumi, Y., and Coté, O.R. (1972). *Spectral characteristics of surface-layer turbulence*. Quarterly Journal of the Royal Meteorological Society, Vol. 98, No. 417.
35. Kaimal, J.C. et al. (1976). *Turbulence Structure in the Convective Boundary Layer*. Journal of the Atmospheric Sciences. Vol. 33.
36. Kaimal, J.C. and Finnigan, J.J. (1994). *Atmospheric Boundary Layer Flows. Their Structure and Measurement*. Oxford University Press, Inc.
37. Karimirad, M. [Accessed 2019]. *MARINTEK Numerical Tools for Coupled Aero-Hydro-Servo-Elastic Simulations of Offshore Wind Turbines*. SINTEF. MARINTEK.
38. Kolmogorov, A. (1941). *The Local Structure of Turbulence in Incompressible Viscous Fluid for Very Large Reynold's Numbers*. Doklady Akademiia Nauk SSSR, Vol. 30, pp. 301-305.
39. Kraus, E.B., and Businger, J.A. (1994). *Atmosphere-ocean interaction*. Vol. 27. Oxford University Press.
40. Kretschmer, Shwede, Guzmán, Lott, and Cheng. (2018). *Influence of atmospheric stability on the load spectra on wind turbines at alpha ventus*. The Science of Making Torque from Wind. IOP Conf. Series: Journal of Physics: Conf. Series 1037.
41. Lackner, M. (2013). *An investigation of variable power collective pitch control for load mitigation of floating offshore wind turbines*. Wind Energy, 16, pp. 519-528.

42. Lalanne, C. (2009). *Fatigue Damage*. Mechanical Vibration and Shock Analysis, Second Edition, Vol. 4. Wiley.
43. Manwell, J., McGowan, J., and Rogers, A. (2010). *Wind Energy Explained: Theory, Design and Application*. Second Edition, Wiley.
44. McNaughton, K.G. (2004). *Turbulence Structure of the Unstable Atmospheric Surface Layer and Transition to the Outer Layer*. Boundary-Layer Meteorology 112: pp. 199-221.
45. Micallef, D. and Sant, T. (2016). *A Review of Wind Turbine Yaw Aerodynamics*. INTECH Chapter 2: Wind Turbines – Design, Control, and Applications. Available at: < http://dx.doi.org/10.5772/63445 >
46. Monin, A. and Obukhov, A. (1954) *Basic laws of turbulent mixing in the surface layer of the atmosphere*. Contrib. Geophys. Inst. Acad. Sci. USSR, 24(151): pp. 163-187.
47. Obhrai, C. (2018) *Climatology of Offshore Wind*. Course- OFF610 Offshore Wind Turbine Engineering. Lecture 3.
48. Olesen, H.R., Larsen, S.E., and Højstrup J. (1984). *Modelling Velocity Spectra in the Lower Part of the Planetary Boundary Layer*. Boundary-Layer Meteorology 29: pp. 285-312.
49. Panofsky, H. A. (1962). *Scale Analysis of Atmospheric Turbulence at 2 Meters*. Quarterly Journal of the Royal Meteorological Society 88, pp. 57-69.
50. Panofsky, H.A. and Singer, I. (1965). *Vertical Structure of Turbulence*. Quarterly Journal of the Royal Meteorological Society 91, pp. 339-344.
51. Peña, A., Gryning, S., and Hasager, C. (2008). *Measurements and Modelling of the Wind Speed Profile in the Marine Atmospheric Boundary Layer*. Boundary-Layer-Meteorology 129: pp. 479-495.
52. Pielke, R.A. and Panofsky, H.A. (1970). *Turbulence characteristics along several towers*. Boundary-Layer Meteorology. 1(2), pp. 115–130.
53. Putri, R. (2016). *A Study of the Coherences of Turbulent Wind on a Floating Offshore Wind Turbine*. University of Stavanger, Master Thesis.
54. Robertson, A., Jonkman, J., Masciola, M., Song, H., Goupee, A., Coulling, A., and Luan, C. (2014). *Definition of the Semisubmersible Floating System for Phase II of OC4*. National Renewable Energy Laboratory. Technical Report. NREL/TP-5000-60601.
55. Robertson et al. (2014). *Offshore Code Comparison Collaboration Continuation Within IEA Wind Task 30: Phase II Results Regarding a Floating Wind System*. Conference Paper. NREL/CP-5000-61154.

56. Ropelewski, C.F., Tennekes, H., and Panofsky, H.A. (1973). *Horizontal Coherence of Wind Fluctuations*. Boundary-Layer Meteorology 5: pp. 353-363.
57. Saranyasoontorn, K. and Manuel L. (2008). *On the propagation of uncertainty in inflow turbulence to wind turbine loads*. Journal of Wind Engineering and Industrial Aerodynamics 96(5): 503–523.
58. Sathe, A., Mann, J., Barlas, T., Bierbooms, W. A. A. M., van Bussel, G. J. W. (2013). *Influence of Atmospheric Stability on Wind Turbine Loads*. Wind Energy, Vol. 16, pp. 1013-1032.
59. Shinozuka, M. and Deodatis, G. (1991). *Simulation of Stochastic Processes by Spectral Representation*. Applied Mechanics Review 44(4), pp. 191-204.
60. Solari, G. and Piccardo, G. (2001). *Probabilistic 3-D turbulence modeling for gust buffeting of structures*. Probabilistic Engineering Mechanics 16, pp. 73-86.
61. Soucy, R., Woodward, R., and Panofsky, H.A. (1982). *Vertical Cross-Spectra of Horizontal Velocity Components at the Boulder Observatory*. Boundary Layer Meteorology 24(1), pp. 57-66.
62. Tieleman, H.W. (1995). *Universality of velocity spectra*. Journal of Wind Engineering and Industrial Aerodynamics 56(1), pp. 55–69.
63. Tran, T. and Kim, D. (2015). *The platform pitching motion of floating offshore wind turbine: A preliminary unsteady aerodynamic analysis*. Journal of Wind Engineering and Industrial Aerodynamics. 142, pp. 65-81.
64. *WindFloat*. (2015). Principle Power, Inc. Available at:
    < http://www.principlepowerinc.com/en/windfloat > [Accessed April 2019]

Appendix

A.1 Damage Equivalent Loads

A.1.1 OC3-Hywind FOWT

Tower Base Fore-aft Bending Moment

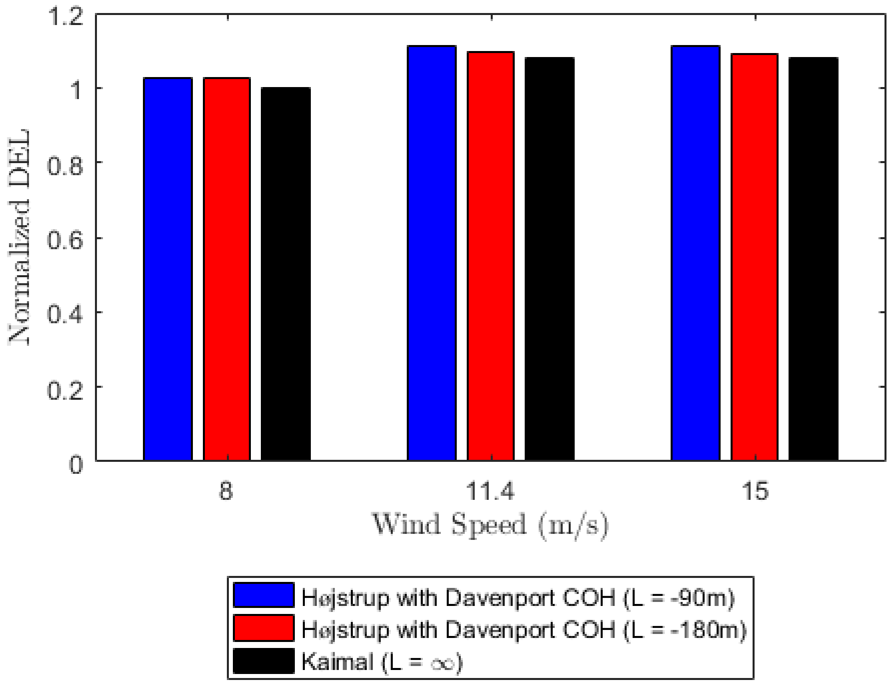

Figure A1: Normalized DEL for tower base fore-aft moment, normalized by the Kaimal model at 8 m/s

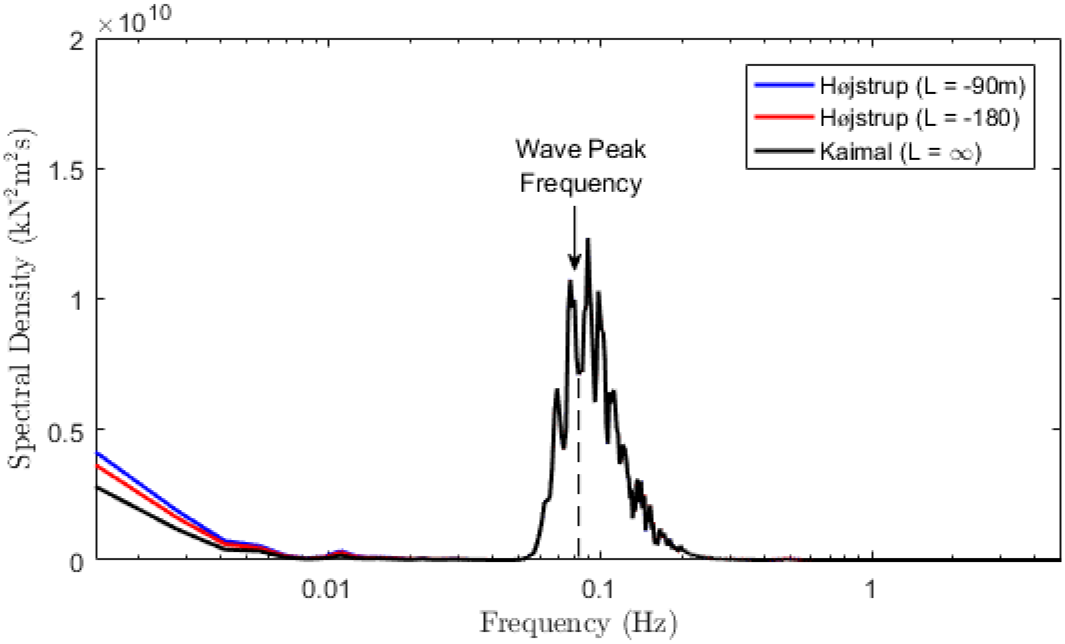

Figure A2: Spectral density of tower base fore-aft moment at below rated (8 m/s) wind speed

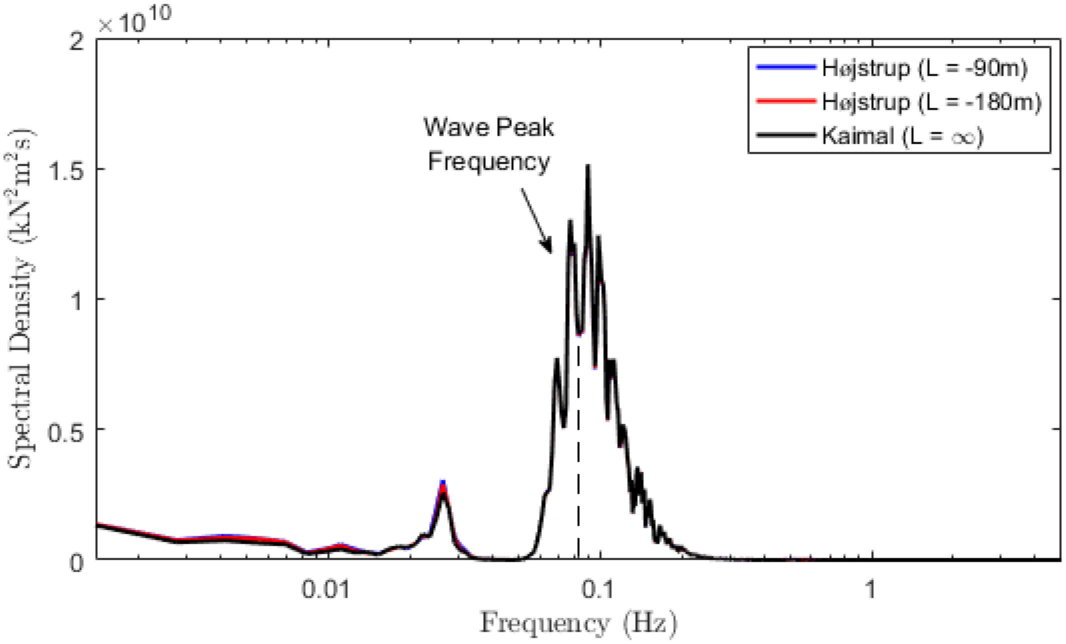

Figure A3: Spectral density of tower base fore-aft moment at rated (11.4 m/s) wind speed

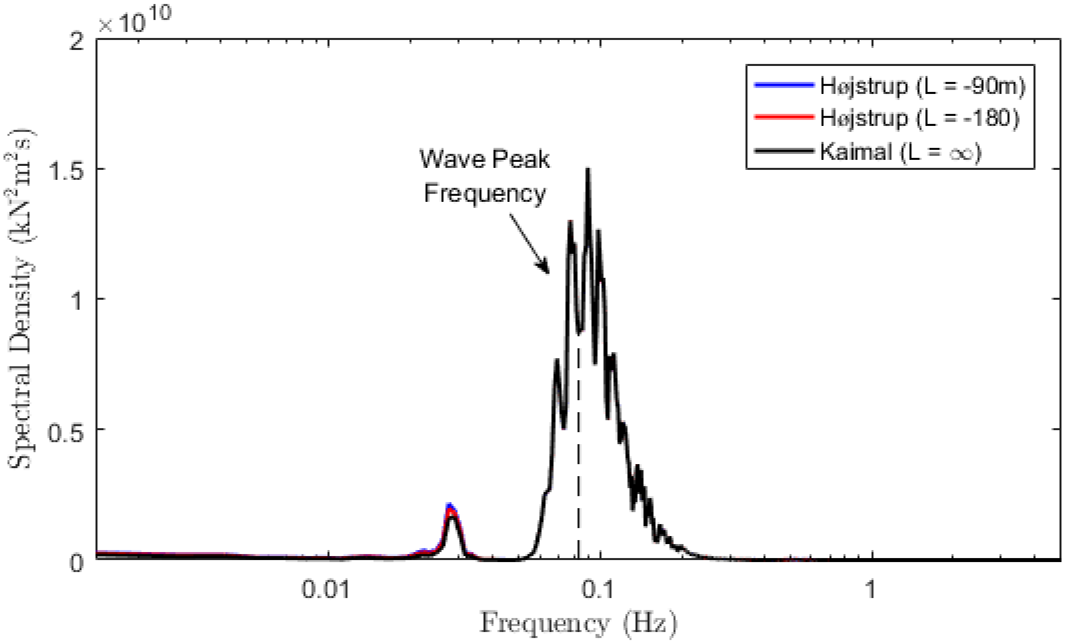

Figure A4: Spectral density of tower base fore-aft moment at above rated (15 m/s) wind speed

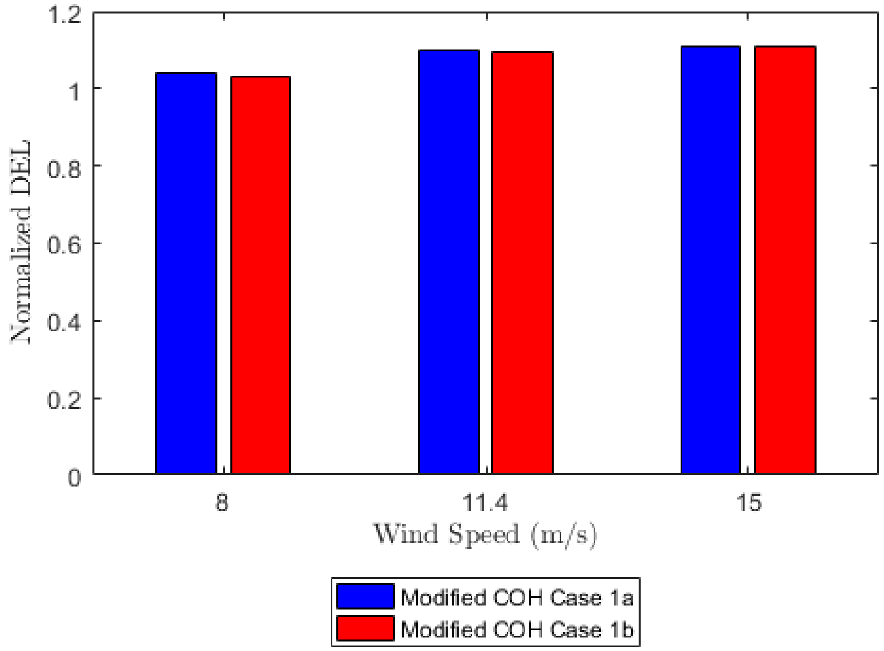

Figure A5: Normalized DEL for tower base fore-aft moment, normalized by the Kaimal model at 8 m/s, for the Højstrup spectra model with varying **vertical** coherence

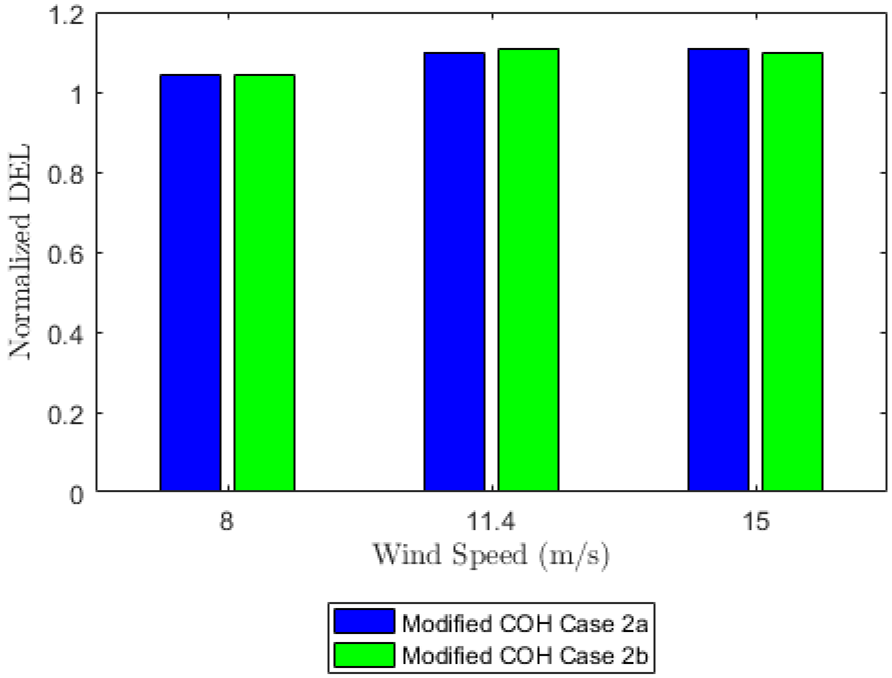

Figure A6: Normalized DEL for tower base fore-aft moment, normalized by the Kaimal model at 8 m/s, for the Højstrup spectra model with varying **lateral** coherence

Mooring Line Tensions

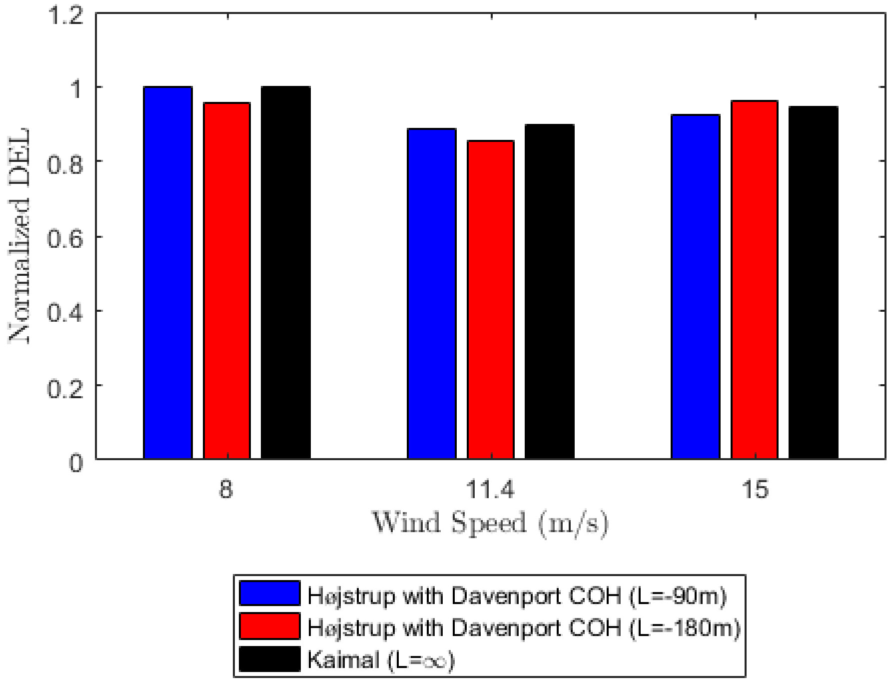

Figure A7: Normalized DEL for mooring line 1 tension, normalized by the Kaimal model at 8 m/s

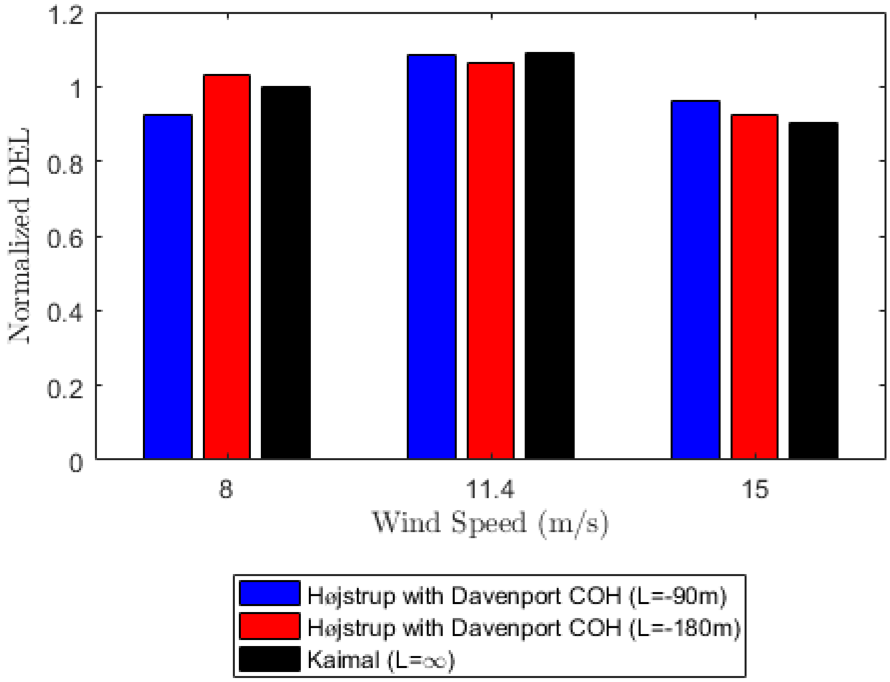

Figure A8: Normalized DEL for mooring line 2 tension, normalized by the Kaimal model at 8 m/s

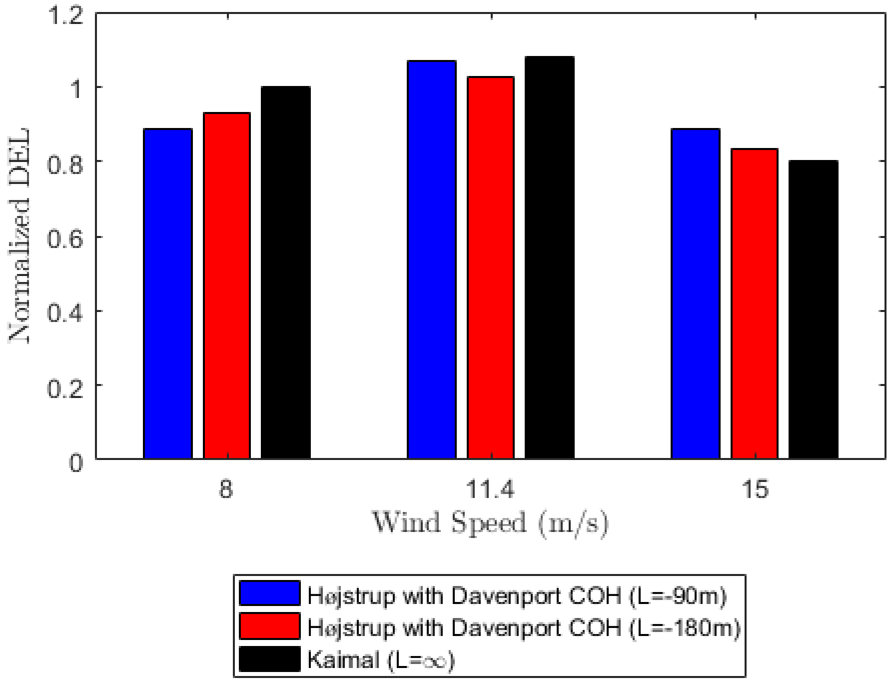

Figure A9: Normalized DEL for mooring line 3 tension, normalized by the Kaimal model at 8 m/s

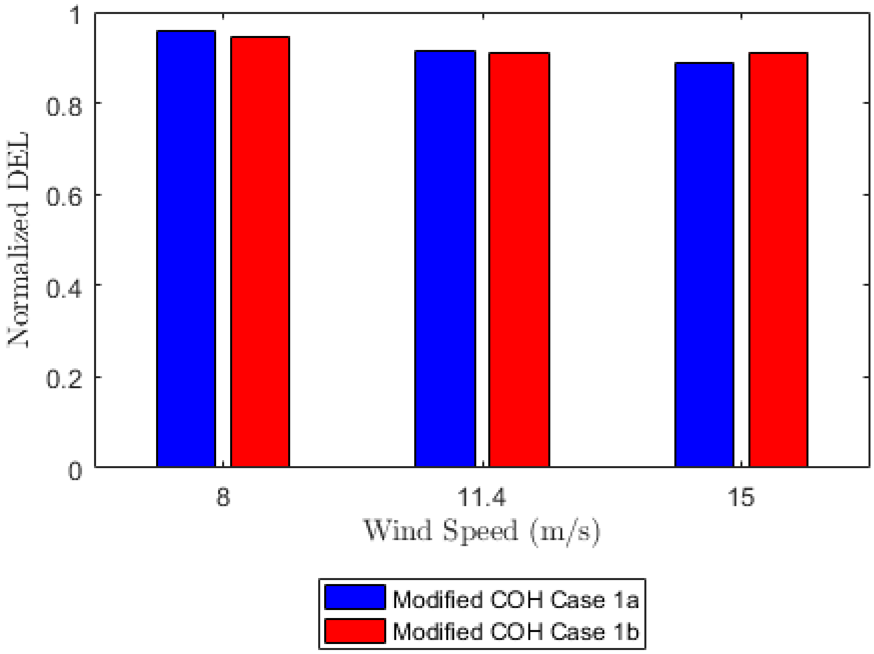

Figure A10: Normalized DEL for mooring line 1 tension, normalized by the Kaimal model at 8 m/s, for the Højstrup spectra model with varying **vertical** coherence

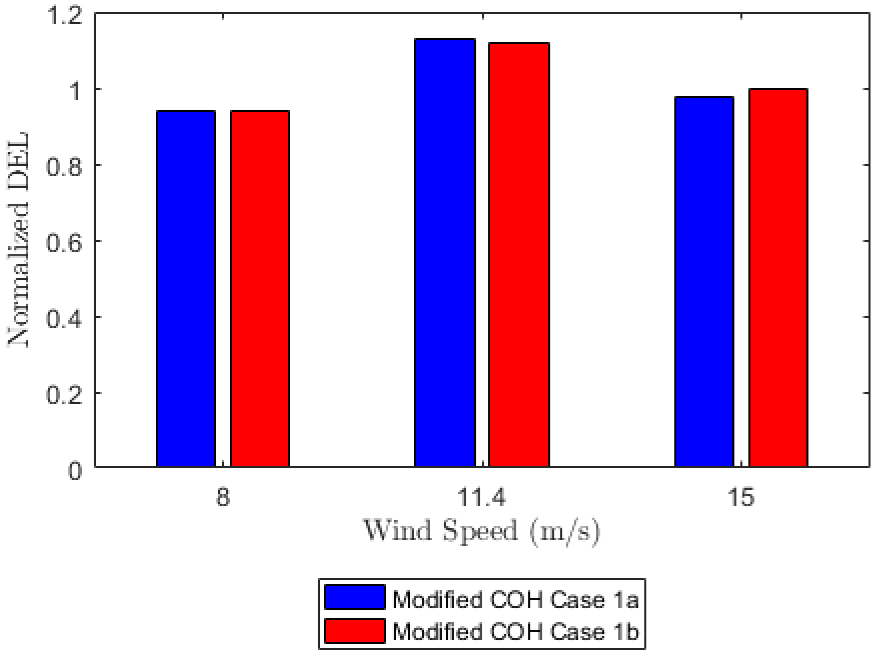

Figure A11: Normalized DEL for mooring line 2 tension, normalized by the Kaimal model at 8 m/s, for the Højstrup spectra model with varying **vertical** coherence

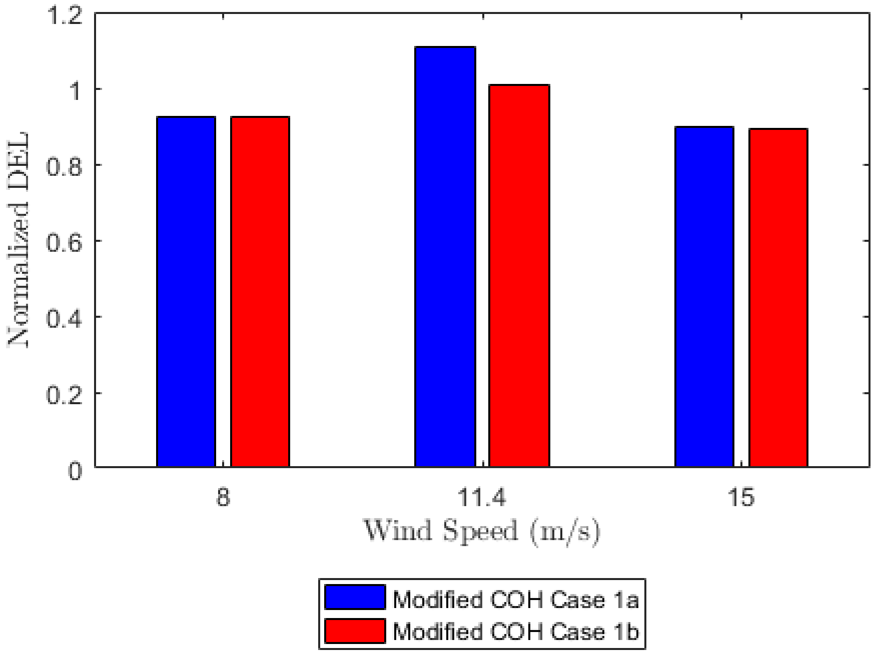

Figure A12: Normalized DEL for mooring line 3 tension, normalized by the Kaimal model at 8 m/s, for the Højstrup spectra model with varying **vertical** coherence

A.1.2 OC4-DeepCwind FOWT

Tower Base Fore-aft Bending Moment

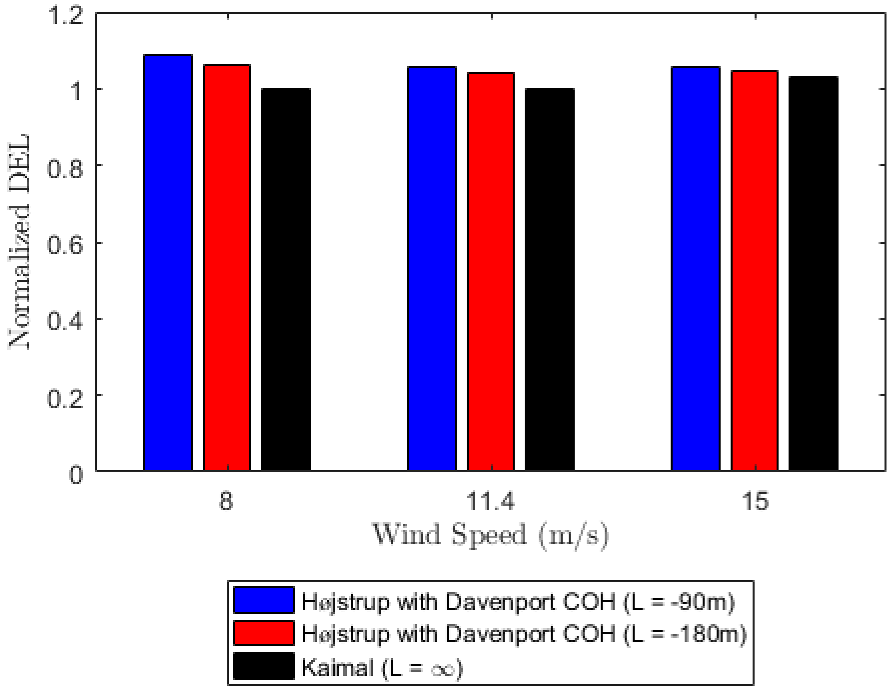

Figure A13: Normalized DEL for tower base fore-aft bending, normalized by the Kaimal model at 8 m/s, with the semisubmersible foundation

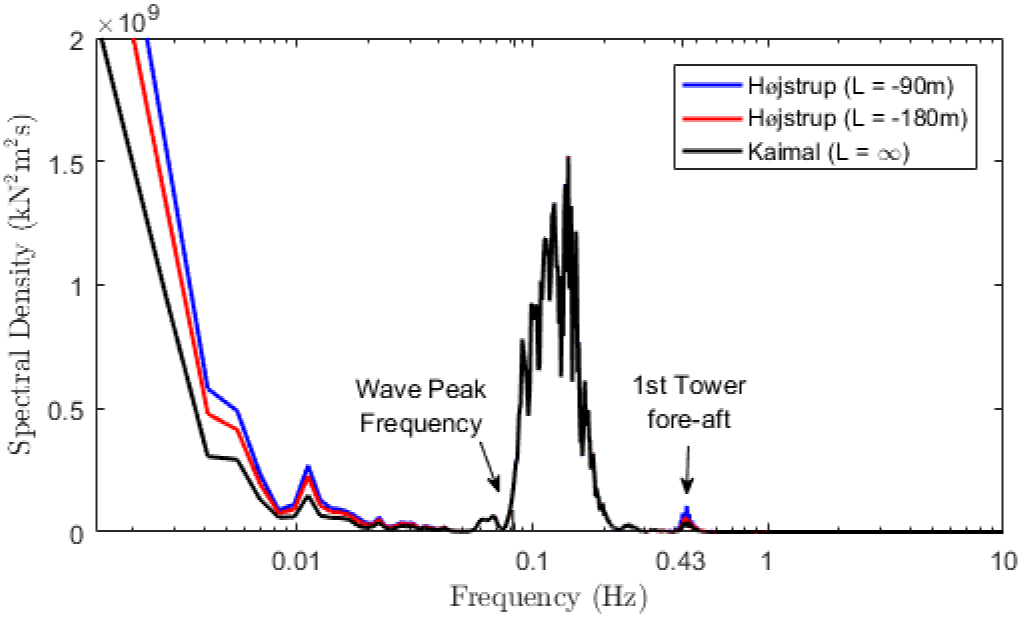

Figure A14: Spectral density of tower base fore-aft moment at below rated (8 m/s) wind speed with the semisubmersible foundation

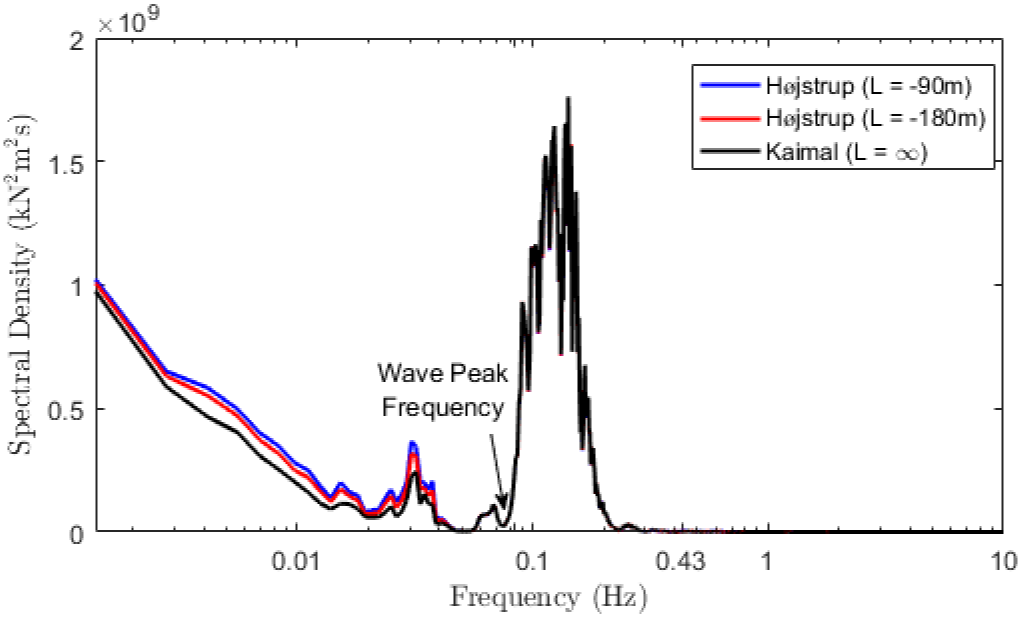

Figure A15: Spectral density of tower base fore-aft moment at rated (11.4 m/s) wind speed with the semisubmersible foundation

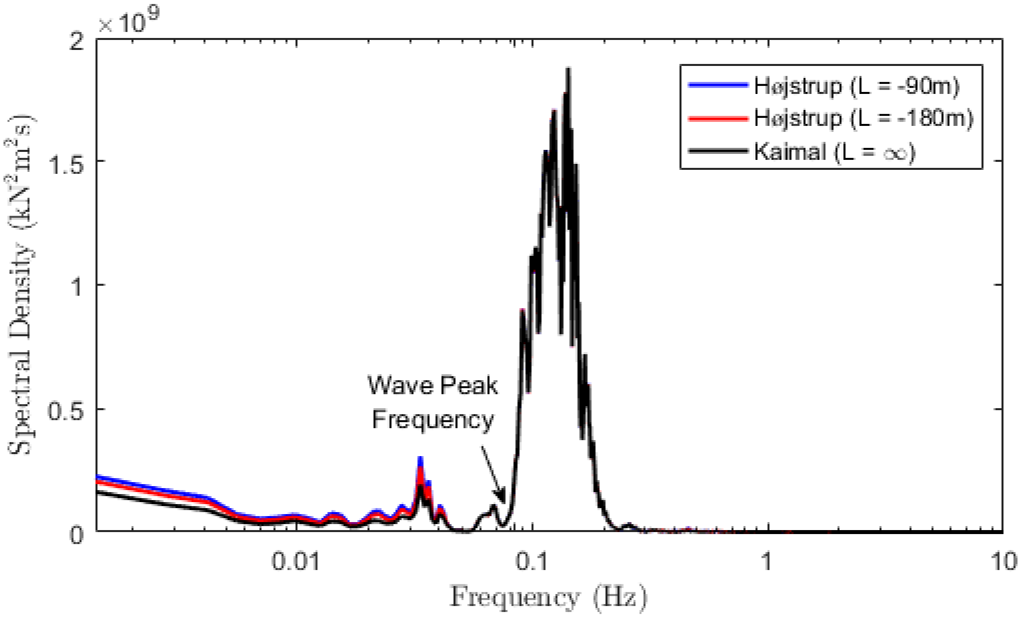

Figure A16: Spectral density of tower base fore-aft moment at above rated (15 m/s) wind speed with the semisubmersible foundation

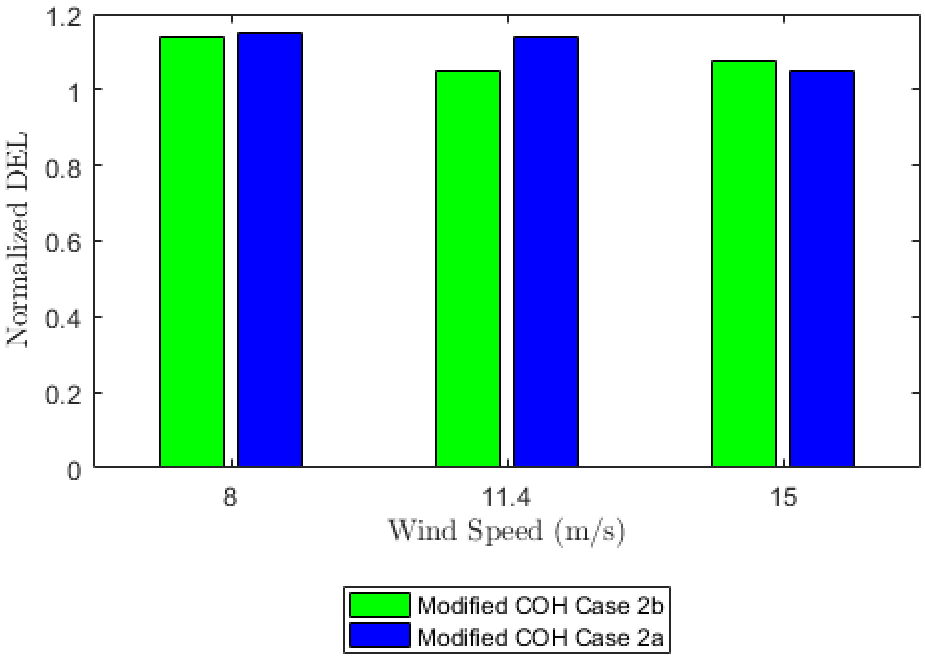

Figure A17: Normalized DEL for tower base fore-aft moment, normalized by the Kaimal model at 8 m/s, for the Højstrup spectra model with varying **lateral** coherence with the semisubmersible foundation

Mooring Line Tensions

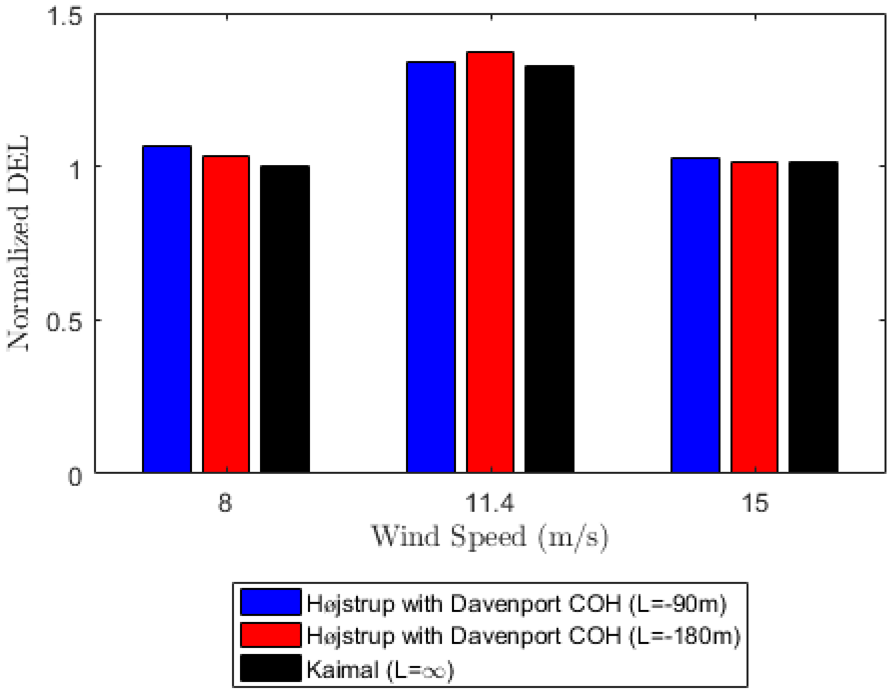

Figure A18: Normalized DEL for mooring line 1 tension, normalized by the Kaimal model at 8 m/s, with the semisubmersible foundation

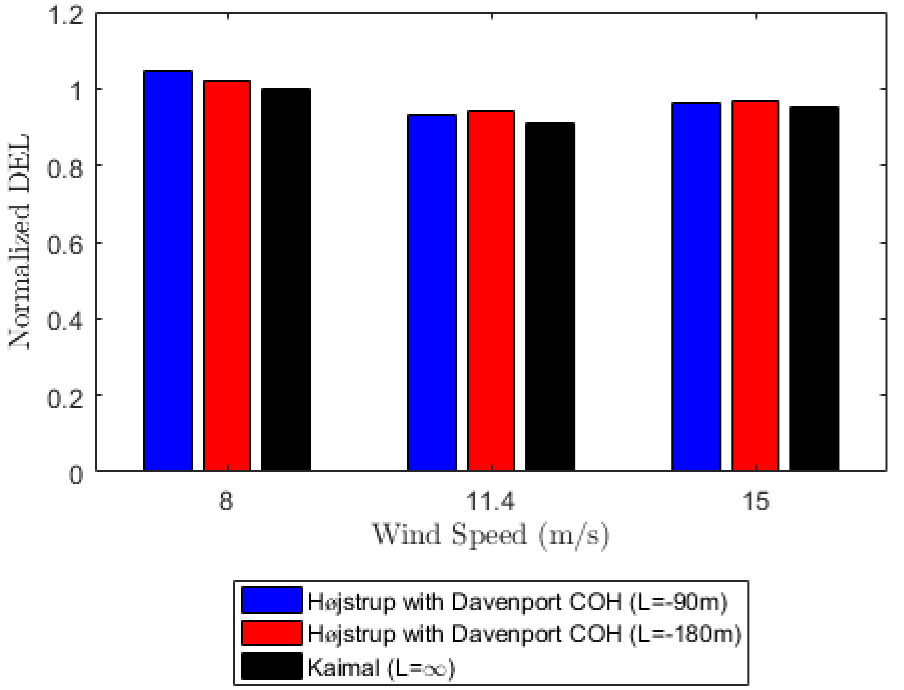

Figure A19: Normalized DEL for mooring line 2 tension, normalized by the Kaimal model at 8 m/s, with the semisubmersible foundation

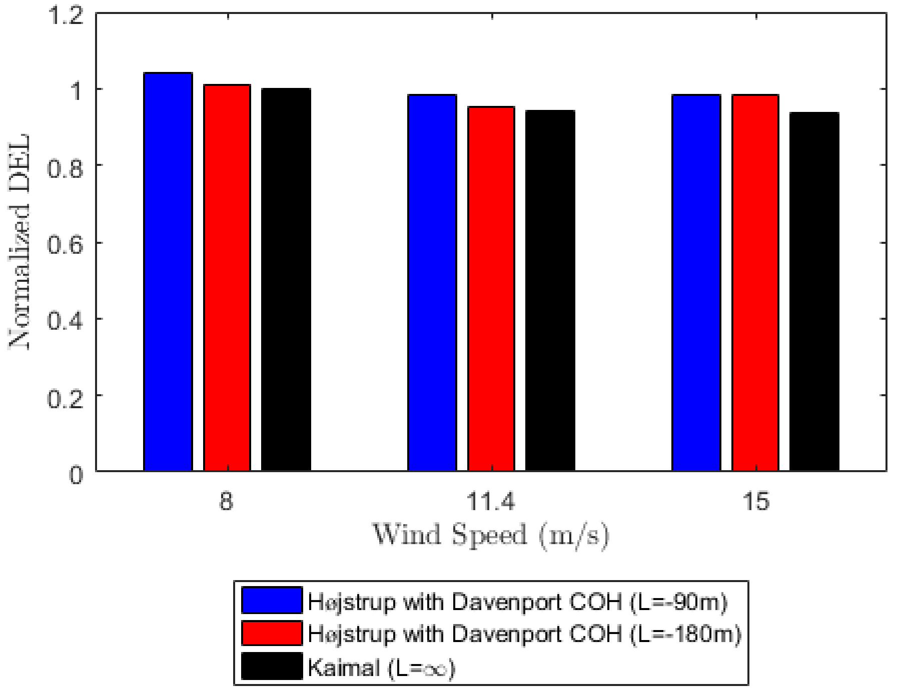

Figure A20: Normalized DEL for mooring line 3 tension, normalized by the Kaimal model at 8 m/s, with the semisubmersible foundation

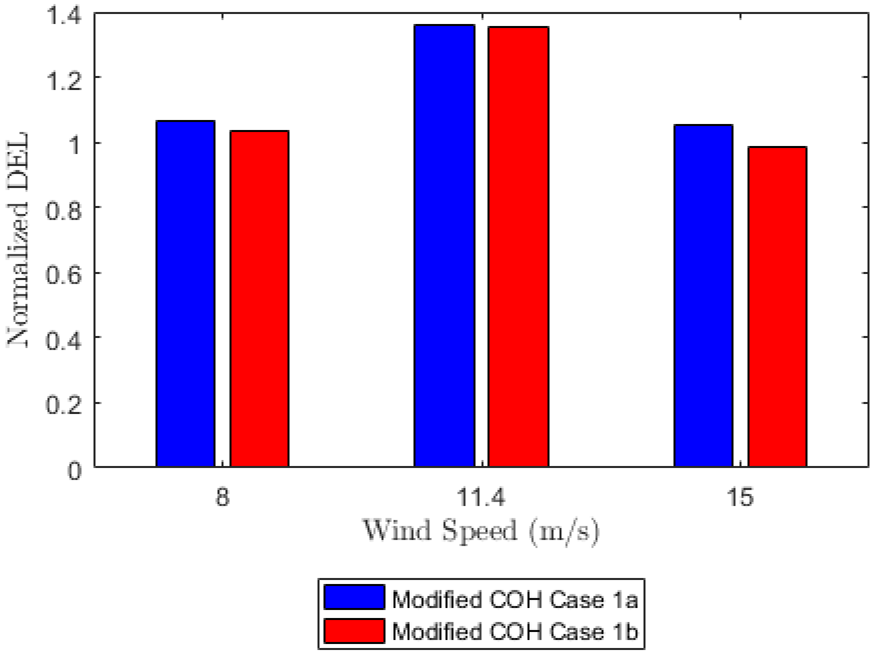

Figure A21: Normalized DEL for mooring line tension 1, normalized by the Kaimal model at 8 m/s, for the Højstrup spectra model with varying **vertical** coherence with the semisubmersible foundation

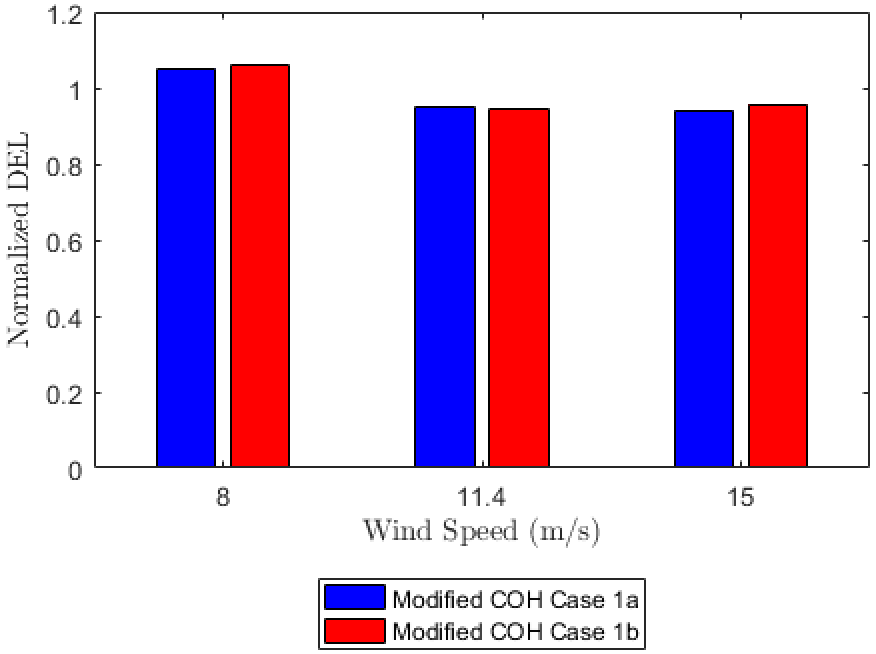

Figure A22: Normalized DEL for mooring line tension 2, normalized by the Kaimal model at 8 m/s, for the Højstrup spectra model with varying **vertical** coherence with the semisubmersible foundation

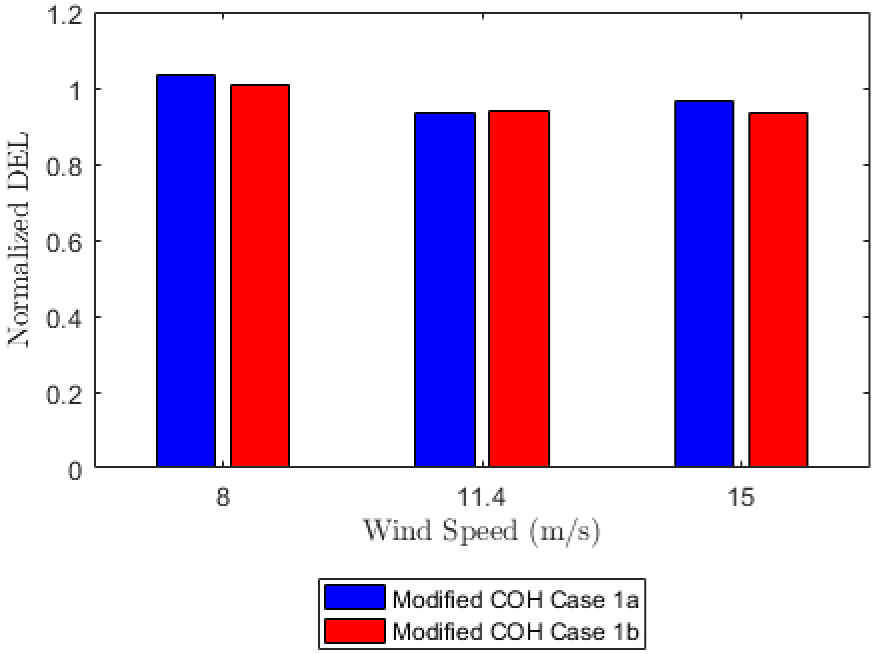

Figure A23: Normalized DEL for mooring line tension 3, normalized by the Kaimal model at 8 m/s, for the Højstrup spectra model with varying **vertical** coherence with the semisubmersible foundation

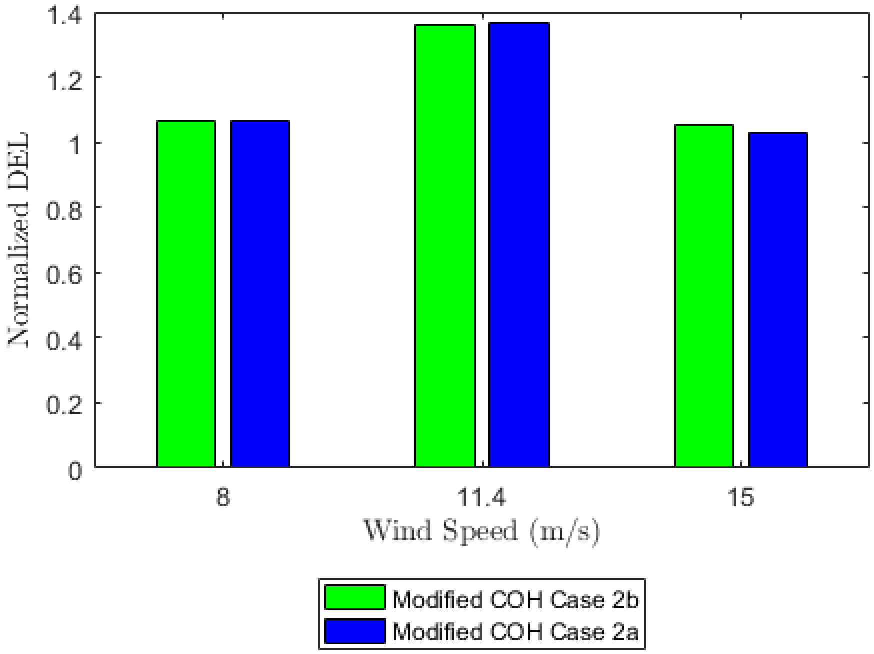

Figure A24: Normalized DEL for mooring line tension 1, normalized by the Kaimal model at 8 m/s, for the Højstrup spectra model with varying **lateral** coherence with the semisubmersible foundation

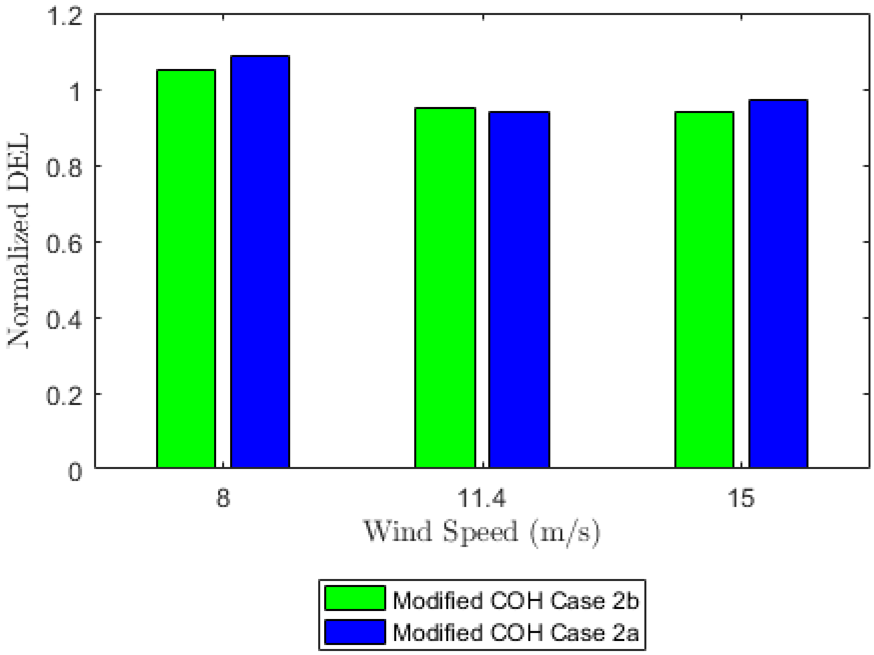

Figure A25: Normalized DEL for mooring line tension 2, normalized by the Kaimal model at 8 m/s, for the Højstrup spectra model with varying **lateral** coherence with the semisubmersible foundation

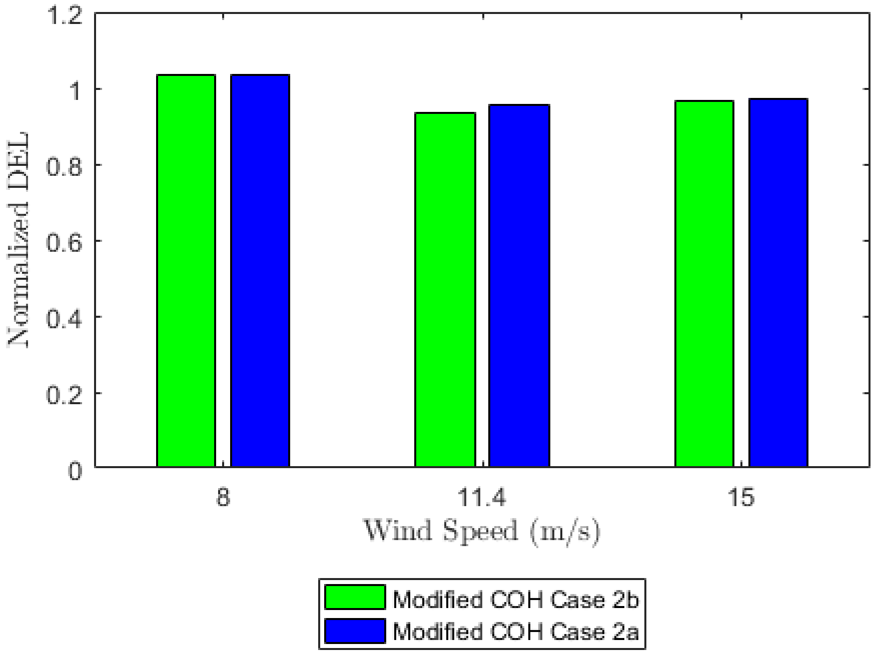

Figure A26: Normalized DEL for mooring line tension 3, normalized by the Kaimal model at 8 m/s, for the Højstrup spectra model with varying **lateral** coherence with the semisubmersible foundation

B.1 Platform Motions

B.1.1 OC3-Hywind FOWT

Surge

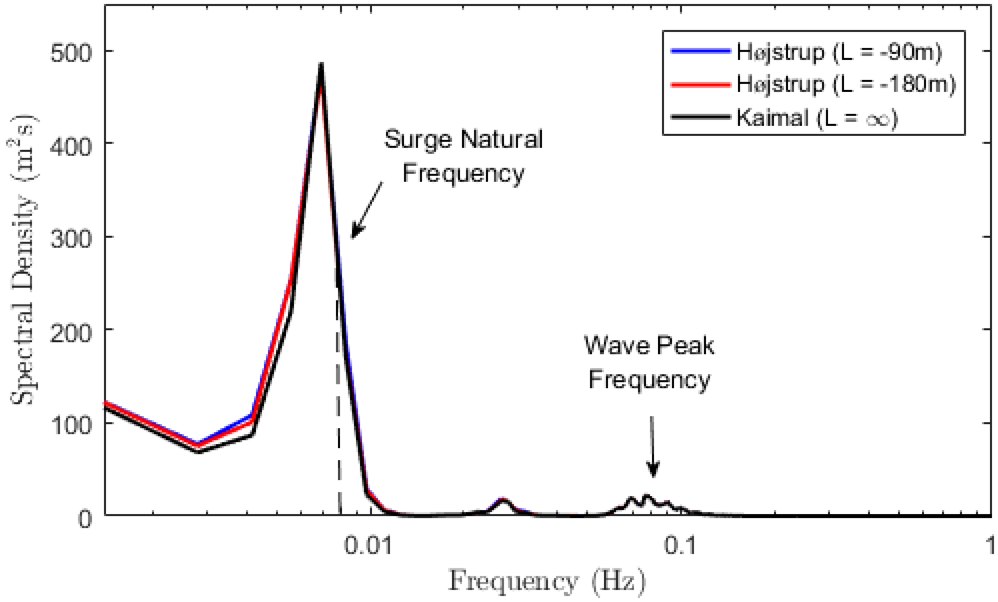

Figure B1: Spectral density of surge displacement for varying stability at rated wind speed (11.4 m/s)

Roll

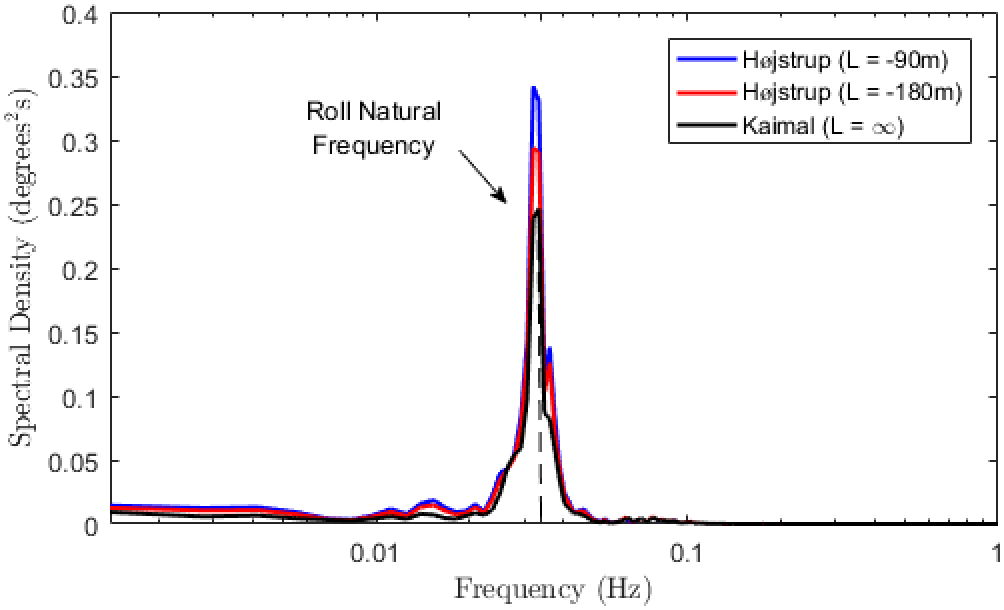

Figure B2: Spectral density of roll rotation for varying stability at rated wind speed (11.4 m/s)

B.1.2 OC4-DeepCwind FOWT

Heave

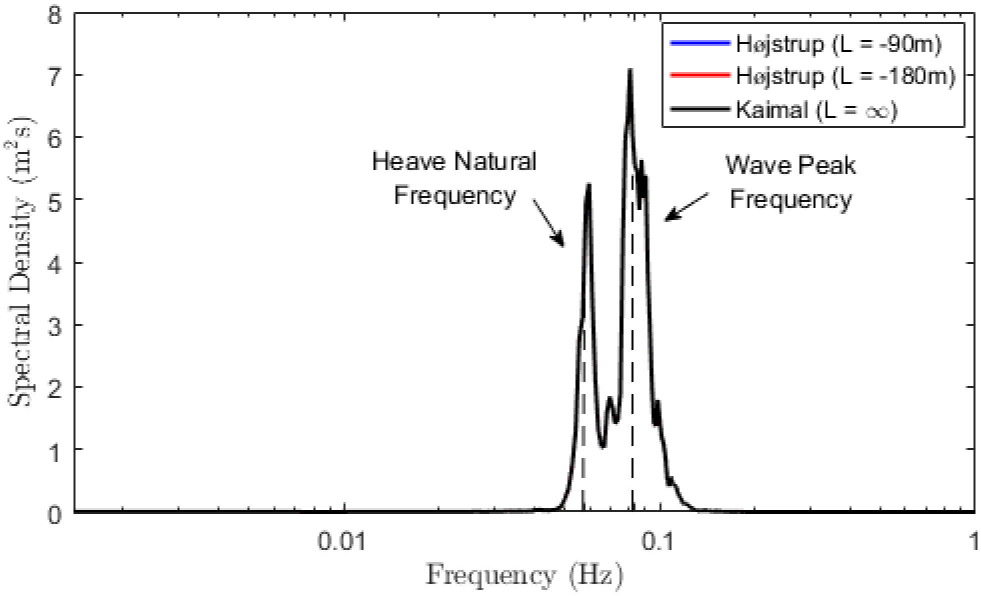

Figure B3: Spectral density of heave displacement for varying stability at rated wind speed (11.4 m/s) with the semisubmersible foundation

Roll

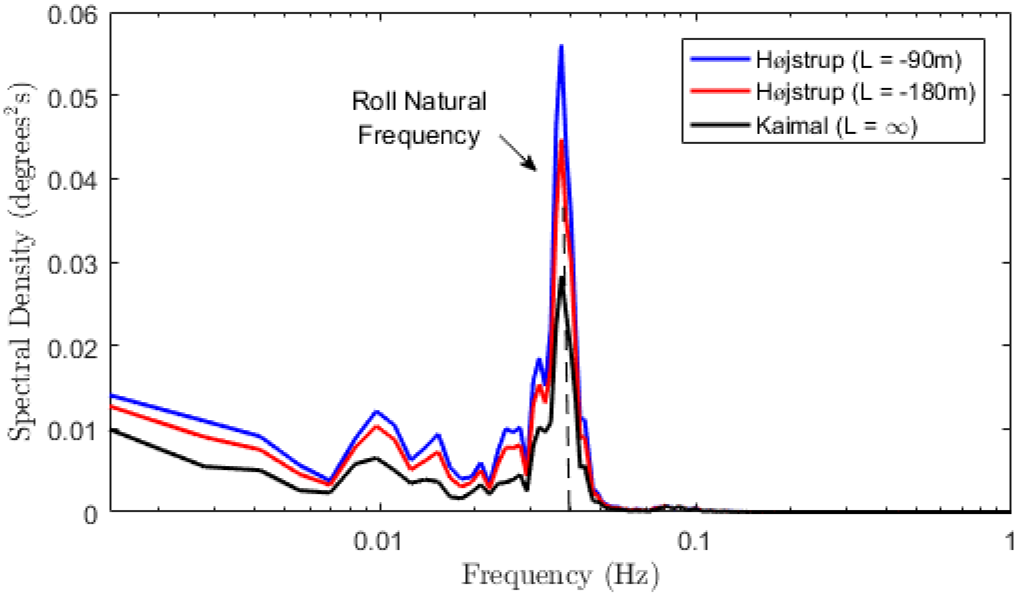

Figure B4: Spectral density of roll rotation for varying stability at rated wind speed (11.4 m/s) with the semisubmersible foundation

Pitch

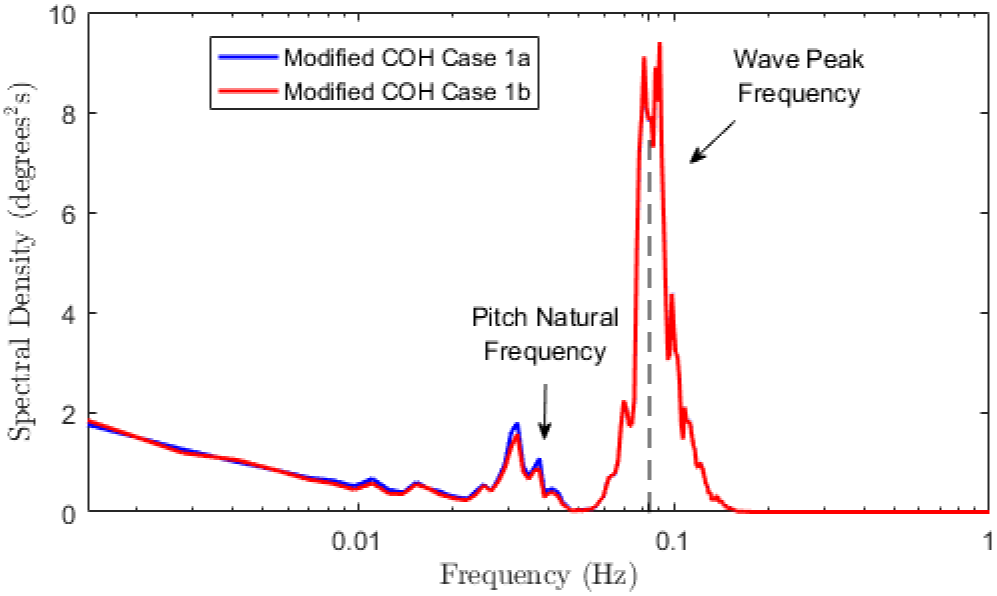

Figure B5: Spectral density of pitch rotation for varying **vertical** coherence at rated wind speed (11.4 m/s) with the semisubmersible foundation

Yaw

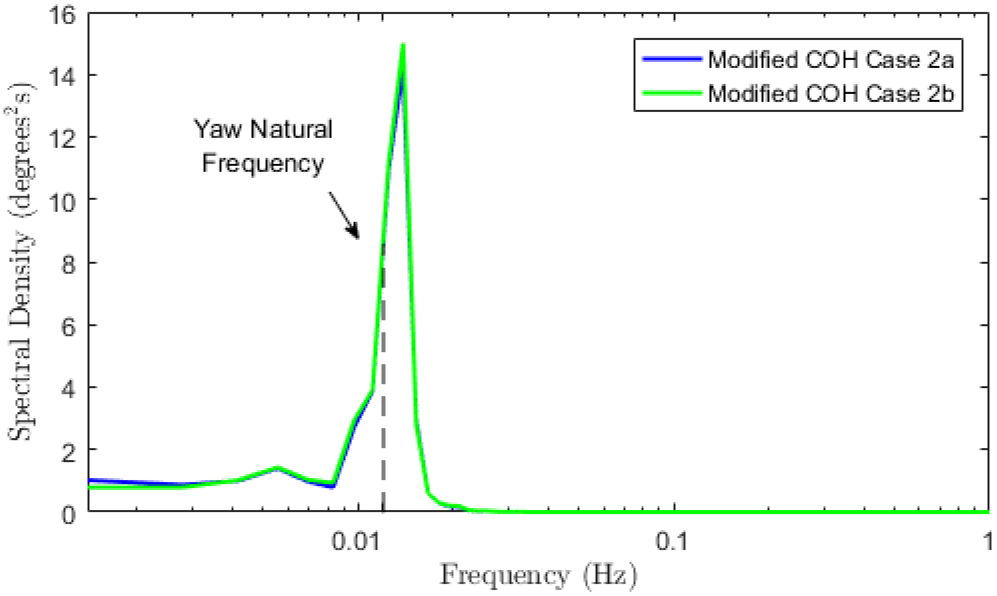

Figure B6: Spectral density of pitch rotation for varying **lateral** coherence at rated wind speed (11.4 m/s) with the semisubmersible foundation

C.1 Algorithms

C.1.1 Simulated Coherence

Since the wind fields generated in this study corresponded to a pre-defined coherence model (e.g. the Davenport Coherence Model or the Modified Coherence Model), the simulated coherence for each wind field could be found by looking at the resulting wind velocities. Using the specified YZ grid created in the MATLAB simulations, various points were chosen from the velocity time series to account for a 30 and 120 m separation distance, both laterally and vertically. The chosen points for the analysis of vertical and lateral coherence sensitivity are marked in red in *Table C1*. Since the y-component varies laterally and the z-component varies vertically, the matrix is defined differently than normal, with the brackets corresponding to: [column, row]. In this study, a 30 m vertical separation was recreated using grid points [16,22] and [16,16], which corresponded to a height above ground of 62.5 and 92.5 m, respectively. A 120 m vertical separation was defined using grid points [1,32] and [1,8], which corresponded to a height above ground of 12.5 and 132.5 m.

Table C1: Relevant points from YZ grid

-77.5,167.5 [1,1]	…	-42.5, 167.5 [8,1]					77.5, 167.5 [32,1]
…							
-77.5, 132.5 [1,8]							
			-2.5, 92.5 [16,16]	…	27.5,92.5 [22,16]	…	
			…				
			-2.5, 62.5 [16,22]				
-77.5, 12.5 [1,32]							77.5, 62.5 [32,32]

Subsequently, using a MATLAB code presented on the following page, the simulated coherence was determined; a coherence function was used to determine the real and imaginary parts of the co-spectrum, which defined the correlation between the two points. This process was carried out for vertical and lateral coherence, which consisted of reading in the appropriate wind velocity .bin file, redefining the chosen grid points, and properly plotting the simulated coherence.

MATLAB code for determining the simulated coherence:

```
%% SIM COH - Case 1
fs = 32768/3600; % sampling frequency (Hz)
M = 15; % M is the power of 2: If M = 10, 2^M = 1024 time step
[t,f] = getSamplingPara(M,fs);

WINDOW = length(t)/64;
NOVERLAP = WINDOW/2;
NFFT = WINDOW;
Fs = fs;

XNEW_vert120 = u1(1,8,:); %120m vertical separation Case 1a
YNEW_vert120 = u1(1,32,:);

XNEW2_vert120 = u1_2(1,8,:); %120m vertical separation Case 1b
YNEW2_vert120 = u1_2(1,32,:);

[cocoh, Quad, freq] =
coherence(squeeze(XNEW_vert120),squeeze(YNEW_vert120),WINDOW,NOVERLAP,NFFT,Fs);

[cocoh2, Quad2, freq2] =
coherence(squeeze(XNEW2_vert120),squeeze(YNEW2_vert120),WINDOW,NOVERLAP,NFFT,Fs);

figure
plot(freq,cocoh,'b','linewidth',1.5) %case 1a
hold on
plot(freq2,cocoh2,'r','linewidth',1.5) %case 1b
xlabel('Frequency (Hz)','interpreter','latex')
ylabel('$\gamma_{uu}$ $(\Delta z,n)$','interpreter','latex')
legend('Modified COH Case 1a','Modified COH Case 1b')
title('120m Vertical Separation in Along Wind')
set(gcf,'color','w')
xlim([0,0.2]);
ylim([-0.5,1]);
grid on
```